UNIVERSITY OF LATVIA

FACULTY OF PHYSICS, MATHEMATICS AND OPTOMETRY

LATVIJAS UNIVERSITĀTE

FIZIKAS, MATEMĀTIKAS UN OPTOMETRIJAS FAKULTĀTE

Ainārs Ozols

Optimization of materials, design and production technology of multifocal liquid crystal diffuser for augmented reality displays.

DOCTORAL THESIS
Submitted for the Degree of Doctor of Physics
Subsector of Material Physics

Scientific Advisor: Dr. Phys. Martins Rutkis

Paplašinātās realitātes displejos izmantojama multifokālā šķidro kristālu difuzora materiālu, dizaina un ražošanas tehnoloģijas optimizācija.

PROMOCIJAS DARBS
Doktora zinātniskā grāda iegūšanai fizikas nozarē
Apakšnozare: materiālu fizika

Zinātniskais vadītājs: Dr. Phys. Mārtiņš Rutkis

Riga, 2022

The doctoral thesis was carried out in EuroLCDs and in the Institute of Solid State Physics, University of Latvia from 2020 to 2022.

The thesis contains the introduction, four chapters with references, conclusions, thesis, 1 appendix.

Form of the thesis: dissertation in Physics, Solid State Physics.

Supervisor: Dr. phys. Martins Rutkis, lead researcher at the Institute of Solid State Physics, University of Latvia.

Reviewers:

Dr. habil. phys. Janis Purans, Institute of Solid State Physics, University of Latvia,

Dr. habil. phys. Maris Knitte, Riga Technical University,

Dr. chem. Romaric Massard, eLstar Dynamics (The Netherlands).

The thesis will be defended at the public session of the Doctoral Committee of Physics, Astronomy and Mechanics, the Institute of Solid State Physics, University of Latvia, at 13:00 on 28th of November, 2022.

The thesis is available at the Library of the University of Latvia, Raina blvd. 19.

This thesis is accepted for the commencement of the degree of Doctor of Physics and Astronomy on 19. September, 2022 by the Promotion Council of Physics and Astronomy, University of Latvia.

Chairman of the Promotion Council _____/ *Anatolijs Šarakovskis/*

Secretary of the Council _____/ *Inese Siliņa/*

Abstract

The development of augmented reality head mounted displays (AR-HMDs) nowadays is becoming very popular and is considered one of emerging technologies for future. One of the current limitations for them to be applied beyond simple 10 minute entertainment is vergence-accommodation conflict. This limitation can be overcome by using volumetric systems for image projection on fast switching liquid crystal diffuser stacks (optical chips). Despite the fact, that polymer free liquid crystal diffusers have proven for large form factor displays, their application for near eye distances provide new requirements in terms of very small dimensions, and high contrast and transparency. This thesis presents the results obtained during design and optimization of liquid crystal diffusers, their production technology and application in AR-HMDs. Using appropriate physical modeling to designing liquid crystal composition and for optimizing employment and technology of known materials, allows us to fulfill above mentioned requirements with reduced volume of experimental work. In cases when traditionally used for LC technology materials could not be applied, other materials were developed, namely silicon oxy nitride thin films with variable index of refraction.

Keywords: augmented reality head mounted displays, liquid crystal diffusers, material characterization, thin film coating, microdisplays.

Contents

List of symbols

D	Diopter
n_o	Ordinary refractive index
n_e	Extraordinary refractive index
k	Imaginary part of refractive index
Δn	Difference between ordinary and extraordinary refractive index
E	Electric field
S	Entropy
V	Voltage
V_c	Critical voltage
P	Liquid crystal pitch
P_0	helical pitch at zero field
K_{11}	Splay elastic constant
K_{22}	Twist elastic constant
K_{33}	Bend elastic constant
$\Delta\varepsilon$	Dielectric anisotropy
U_{drive}	Driving voltage
$U_{threshold}$	Threshold voltage
d	Cell gap
ɣ	Rotational viscosity of LC
ε_0	Vacuum permittivity
ε	Relative electrical permittivity of media
λ	Wavelength
λ_0	Wavelength of light in vacuum
T	Transmittance
R	Reflectance
A	Absorbance
R	Resistivity
I	Current
q	Charge
r	Reflection coefficient
δ	Phase delay
Θ	Incidence angle of light
p	Pressure
X	Spacer sphere deformation
K	Spacer compressibility modulus
r	Radius of spacer
F	Deformation force
H	Gap height
p	Pressure on display
L	Display length
b	Glass thickness
E_s	Spacer elasticity modulus
s	Degree of surface coverage with spacers
d	Spacer diameter

List of abbreviations

AR-HMDs	Augmented reality head-mounted displays	PDLC	Polymer dispersed liquid crystal
VR	Virtual reality	PFLC	Polymer free liquid crystal
AR	Augmented reality	RI	Refraction index
3D	Three-dimensional	ITO	Indium tin oxide
VAC	Vergence-accommodation conflict	PVD	Physical vapor deposition
		CVD	Chemical vapor deposition
MOE	Multi-plane optical element	ODF	One drop fill
SLM	Spatial light modulator	RGB	Red Green Blue color model
DMD	Digital micro mirror device	FC-D	Metastable focal conic state
LED	Light emitting diode	HTP	Helical twisting power
LCD	Liquid crystal device	E7	LC reference composition, Merck trade name
LC	Liquid crystal		
MTF	A measure of the ability of an optical system to transfer various levels of detail from object to image (modulation transfer system)	PET	Polyethylene terephthalate
		XPS	X-ray photoelectron spectroscopy
		DC	Direct current voltage
		sccm	Standard cubic centimeters per minute
ANSI	American National Standards Institute	HEPA	High efficiency particle filter
ISO	International Standard Organization	TFT	Thin film transistor
		VCF	Vacuum capillary fill method
FOV	Field of view	OCA	Optically clear adhesive
FWVGA	854×480 pixel resolution	CTE	Coefficient of thermal expansion
BBAR	Broad band antireflective coating		
		TML	Total mass loss
5-CB	4'-Pentyl-4-biphenylcarbonitrile	CVCM	Collected volatile condensable material
DSM	Dynamic scattering mode	UV	Ultraviolet spectra
P	Planar state	AA	Active area of display
FC	Focal conic state	ns	Nanosecond
TP	Transient planar state for PDLC	nm	Nanometer
		nF	Nano farad
M	Transient state for PFLC	ps	Picosecond
H	Homeotropic state	μs	Microseconds
PSCT	Polymer stabilized cholesteric texture	mg	Milligram
		μg	Microgram
TN	Twisted nematic	nL	Nanoliter
E-O	Electro-optical		
		pcs	pieces

List of Figures

List of Tables

1.Introduction

Demonstrated on the brink of the 20th century by Ferdinand Braun [1] , the cathode ray tube was the first widely used display technology. In the past decades, the liquid crystal displays (LCD) have become the market dominant technology – in 2019, almost half of private households worldwide were estimated to have a personal computer and in developing countries, this number is closer to 80 percent [2]. Even though many people spend their entire working-days looking at some form of digital display, the displays themselves have not undergone a major paradigm shift since their inception – the majority of displays still render a 2D image on a flat surface. Some efforts have been made towards displaying 3D images, but that has predominantly been achieved by use of stereoscopic 2D displays with binocular disparity. The problem with such an approach is the perceived ambiguity in 3D graphics representation due to the lack of true depth cues. This issue can be solved by utilization of a volumetric display.

There are multiple approaches of implementing a volumetric display, but the general concept is image generation from light-emitting, scattering or relaying pixels (called voxels) that occupy a physical volume in space [3]. A volumetric display can be either static (solid-state up-conversion displays, gas medium displays, voxel arrays, layered LCD stacks, and crystal cubes) as well as swept (rotating LED arrays, cathode ray spheres, varifocal mirror displays, rotating helix displays, and rotating flat screens) [4], [5]. The swept volume displays make use of the persistence of human vision to recreate 3D images. While a multitude of elaborate methods (e.g. the photophoretic-trap volumetric display [6]) for creating a volumetric display has been demonstrated in laboratory conditions, many of these display types are far from market-ready due to the complexity of manufacturing, safety concerns, low image resolution, low refresh rate or sub-par color reproduction.

The majority of currently-feasible volumetric displays are based on rear-projection and some sort of screen (either static or swept). The major limitation for these kinds of displays is the frequency of operation of the projection unit – this means finding a compromise between the total volume of a display and its discretization (the number of layers). Even though volumetric displays with moving membranes/screens have reached a stage of development past a laboratory demonstration [7] and can be considered commercial product-ready (e.g. the Voxon VX1), the lifespan of devices with moving parts are usually shorter than that of their solid-state counterparts. Therefore, the preferred implementation of a volumetric display is often entirely solid-state, and swept displays are mostly used for niche products. A proposed solution for an entirely solid-state display is a stack of transparent organic light-emitting diode (OLED) panels [8], however, the transparency and haze values do not currently allow reaching a meaningful stack depth. Alternatively, a rear-projection device coupled with

a stack of fast-switching liquid crystal (LC) diffuser elements can yield in a practical volumetric display with reasonable volume and its discretization. This concept has been researched in-depth[9] at LightSpace Technologies/EuroLCDs and the focus of this work is to provide comprehensive analysis of solid-state volumetric display architecture and the required properties of the corresponding key-enabling element – a liquid crystal diffuser.

3D displays of future with certainty will have to overcome limitations of currently common stereoscopic 3D displays – such as used for virtual and augmented reality. It could be said that the main shortcoming of single-focal plane stereo displays is lack of consistency between vergence and accommodation depth cues – in other words, a viewer has to fixate accommodation at a single distance. This brings about well-known by now vergence-accommodation conflict which can manifest differently for different people but most commonly is associated to eye-strain, blurry vision and generally contributing to what is known as "cyber-sickness" [10], [11].

A very promising solution for enabling consistent accommodation within a 3D scene presented by a stereoscopic display – is solid-state multi-focal displays [12]. While implementations with varifocal lenses have been demonstrated [13], [14], a solid-state solution typically is regarded as more preferable. For a solid-state implementation a stack of transparent displays is needed. Previously it was believed, that such candidate would be a transparent OLED display [15], [16]– nevertheless, endeavors of researchers and manufacturers didn't succeed to an expected extent. One of the main drawbacks was optical haze, which prevented formation of screen stacks and generation of high-quality image.

Thus, a very viable alternative concepts of which have been demonstrated in early 2000s is a solid-state volumetric technology based on switching optical diffuser elements [9]. The early implementation was based on polymer-dispersed liquid crystal (PDLC) of cholesteric type. Under applied voltage cholesteric spirals were broken up and liquid crystal transitioned into a homeotropic state (H) having high transparency and low haze values. Upon removal of voltage – it collapsed back to light scattering focal-conic state (FC) [17]. The addition of polymer network helped with FC domain formation and generally improved light scattering properties in the diffuse state. Nonetheless, presence of polymer network within a diffuser element interfered with incident light in the transparent state – having unwanted haze off the principal view direction. In terms of switching characteristics, polymer networks also tend to slow-down the transition between optical states, which is crucial for multi-focal and volumetric display architectures reliant on a time-sequential switching between multiple stacked diffusers.

To overcome these limitations a diffuser composition without addition of stabilizing polymer networks was developed. A polymer-free liquid crystal (PFLC) of cholesteric type cell works similarly to PDLC cells in a time-sequential display scenario. Instead of polymer networks facilitating scattering of light, the relatively short-lived transient superscattering state is utilized. This state is characterized by fine-domain structure of focal-conic (FC) texture, which isn't stable [18] for long periods but more than sufficient for time-scales required by time-sequential switching in a volumetric display.

The task of this work has been to redesign PFLC cells for new application in head mounted, volumetric augmented reality displays. New requirements demand to investigate liquid crystal switching mechanisms and optimize overall design of the cell for optimized optical performance of small form factor application. Rather than simply downsizing, the strategy towards this task is to design from set requirements, use modelling approach to decrease experimental work volume and modify existing materials and methods or develop new materials.

1.1 Motivation

The journey to this work started in 2011 when founder of EuroLCDs company, Ilmars Osmanis said: "We have 27 trucks of LCD equipment and agreement from Ventspils Free Port Authority for green field project. It is your task to build factory, develop technology, hire and train staff so we can produce liquid crystal devices for 3D volumetric image devices". I had relevant industrial experience but the display technologies were known to me only by general principles and education in organic chemistry.

So it began, from designing cleanroom and factory, to first 80x80 mm LCD trials to 19 inch diffusers, then to 27 inch displays, mostly developing technology by ourselves. We gathered information on LCD technology from books, publications and many people who provided guidance in this journey. It will be a very long list of sources, names, companies and research institutions. As we begin to specialize in large size, high voltage, scattering type of displays, the technology started to differ from traditional LCD technology. Stepwise we adapted it for larger and larger sizes, mostly based on experimental data.

In 2019 the focus changed to small displays with the trend towards head mounted displays. This provided new challenge, as microdisplays demands other materials and technologies. This time we wanted to start with the design, select proper materials for expected outcomes, reduce number of experiments by modeling the solutions, a more proper way to design new product. I was going to review my current knowledge and material physics. As with COVID-19 lockdowns, more time was available for writing, I decided to summarize findings in form of PhD work. With this work, I hope to

fill the gaps in my knowledge and in the same time leave valuable knowledge for my colleagues for years to come.

Moreover, the application of augmented reality head mounted displays for professional medics become important due to higher demands for safety from COVID-19 infections. The benefit of augmenting reality in operation rooms and hospitals for medics without contamination risks was clearly seen by professionals. PFLC diffuser technology proven for large form factor volumetric displays, at this time point, was the one that could be developed this application.

1.2 Aim and objectives of the work

Is to develop key enabling element for multi focal display application by downsizing PFLC diffusers by:

1. investigating literature data applicable to miniature liquid crystal diffusers;

2. characterizing material properties for application if literature or supplier data is not available;

3. find optimum material combination and structural design for diffusers by using numerical modelling methods thus decreasing amount of experimental work;

4. according to modelling results, manufacture experimental diffuser samples and analyze obtained results, as well as evaluate reliability of modelling;

5. if traditionally used materials and methods are not capable to provide expected results, research new methods and materials for improving diffuser electro optical performance, namely transmittance of the open state, scattering properties of closed (diffuse) state and minimize switching time between both states;

6. find the best diffuser design based on literature review and experimental results;

7. perform scale-up of technology and ensure protection of intellectual property rights for innovations of this work.

1.3 Scientific novelty of the work

A novel PFLC diffuser element system (optical chip) was developed in small size factor, enabling its use in AR-HMD systems. For a first time SiO_xN_y coatings were used to improve optical performance of the diffuser element as index matching, dielectric and LC orientational layer. Switching time was improved by means of optimizing high twisting power dopant concentration and surface alignment combination and spectral dispersion of diffuse state. For a first time it was demonstrated that switching occurs via uniform lying helix.

A demonstration unit of diffuser element has been made and is successfully integrated in AR-HMD system.

Completed research and implementation work have been included in the 5 patents and 3 more patent applications are currently submitted.

1.4 Structure of the thesis

The main text of the thesis is divided into four parts –Augmented Reality head mounted displays, Dynamic light scattering of liquid crystals, Solid State material interaction with electromagnetic waves, Single diffuser and multifocal diffuser (optical chip) build up, and Conclusions and defendable thesis. Each part is further divided into Literature review, Aim and objectives for materials, Experimental part and Conclusions for more convenient reading, as each part can be separate theme.

In the Literature review, a brief overview of different materials and methods for specific parts will be given that will serve as starting point for setting aims and objectives of the work. Aims and objectives of the materials will contain considerations how they could be achieved. Calculations and modelling will be done here. The Experimental section will be compiled of sample preparation routines, sample characterization methods, and results. Conclusion section will summarize up observations and conclusions from modelling and experiments. Finally, all results from this work will be summarized in Conclusions and Thesis.

1.5 Author's contribution

The experiments presented in this work were done by the author of this work, except specific experiments and measurements with equipment available in Institute of Solid State Physics that required proper training and qualification (XPS, AFM, sputtering cluster etc). Characterization of diffuser visual properties with combination of headset projection system were done by my colleagues in Lightspace Technologies.

The author prepared Design of experiment plans for the work, supervised operations and prepared reports using liquid crystal display production line. Line functions were ensured by its operators. If multiple sample characterization were required, it was done by operators, using methodology developed by author after first samples have been tested. All COMSOL Multiphysics, CODE V modelling were done by the author. Optilayer and Filmwizard modelling were carried out by colleagues Martins Narels and Sandra Balode.

All of the data processing and result interpretation were done by the author.

2. Augmented reality head-mounted displays (AR-HMDs)

2.1 General technological approaches in AR-HMDs

Augmented reality and virtual reality both have become more than "sci-fi" now. Virtual reality (VR) places user in world wholly generated by computers, partly or completely composed of imaginary things, people or scenes. Augmented reality (AR) use optical combiners, displays and photonic devices to "add" computer generated objects in real world scenery. The most common method is to use transparent optical chips, which allow to see real world and virtual images by human eyes simultaneously. Research nowadays focuses on projection systems and optical chips for AR-HMDs, as there are many challenges so they may become part of everyday life. Ergonomic, field of view, resolution, brightness, optical transmittance, aberrations are just few examples for research and development. This involves use of new materials or recombination of the traditionally used, commanded by requirements stemming from AR-HMDs high expectations.

Augmentation of reality by targeted (contextual) visual information in real time – in a format of critical information, alert or manual can be an effective method to reduce emotional stress levels while executing high-complexity high-risk tasks. Moreover, it is useful also for less complex tasks – such as assembly and repair of mechanisms – where it can improve efficiency of task execution, reduce error rates, by providing a convenient access to the needed information – without consulting printed materials. In case of medical applications – especially if the working environment is contagious – similarly such device makes any printed materials (*unnecessary surfaces for transferring contaminants*) obsolete, by providing a medic with all the relevant information digitally while ensuring free hands for manipulations.

The target format for such AR-HMDs is a glasses or headset type of device. Nevertheless, to fully exploit the possibilities such devices can offer in the professional work environment - they have to be stereoscopic in order to convey perceptually three-dimensional (3D) image. Currently in the market there are two wider-known manufacturers (*Microsoft with its Hololens project and Magic Leap Inc. with ML1*) which offer a well-developed system. Nevertheless, these devices are ill-suited for listed professional use-cases. The majority of professional tasks or actions where the benefits of an AR headset would be most notable involve near-work – a work where the operator/medic performs a manual task. This means that any relevant 3D information should be output perceptually also at close distances (up to an arm's reach). As conventional stereoscopic displays employ binocular disparity [19]–[21] as the source for 3D depth cues while utilizing only a single display (single focal plane), they introduce so-called vergence-accommodation conflict (VAC) [22], [23]. This means that

the eyes at all times have to be focused (accommodated) at the plane of display, which typically is located around 2 – 3 meters from eyes, while binocular disparities drive the vergence mechanism freely. At close vergence distances, the mismatch between vergence distance and accommodation distance can be severely out of tolerable by majority of people limit (~0.5 Diopters) [22], [24]. For example – if a display optically is located at 2 meters (0.5D), while the object is rendered to be at 40 cm (2.5D) – the resultant vergence-accommodation mismatch is 2 Diopters. As a result, a forceful uncoupling of neutrally coupled eye vergence and accommodation mechanisms can manifest as blurred image at close distances, eyestrain, generally unpleasant visual sensations – all contributing to limited viewing time and general inapplicability of conventional stereoscopic display systems for high image quality at close distances. Unfortunately, Microsoft Hololens and Magic Leap ML1 are no exceptions and also are prone to introducing vergence-accommodation conflict. While Magic Leap tries to slightly mitigate VAC by adding a second focal plane which based on the gaze direction is active – it doesn't solve the problem sufficiently and comes at a cost of reduced ambient light throughput and degradation of presented image quality [25].

To overcome the major drawback of VAC, a stereoscopic display system has to convey monocular focus cues – or otherwise be able to drive the accommodation consistently or semi-consistently with the vergence. Ideally there shouldn't be any significant mismatch between the vergence and accommodation distances, but the display system would perform sufficiently well for professional near-work applications, if the VAC wouldn't go outside the threshold limit for visual comfort (~0.4-0.6 D). If we consider a multi-focal display architecture – a typical supported full range of accommodation – 4 Diopters (25 cm to infinity) – effectively can be covered by 4 – 6 focal planes without subjecting a person to any state of visual stress. Though there are alternatives to multi-focal display architecture – such as light field displays and true holographic displays, these technologies currently haven't been shown to deliver minimum viable image quality at a reasonable footprint.

Similarly, with multi-focal displays there is a challenge to ensure sufficiently fast image refresh rates, low image aberrations and high light throughput. On one hand transparent self-emissive displays can be used to form stacks of multiple focal planes – nevertheless, the transparency isn't sufficient and substantial haze values adversely impact image quality on deeper layers [26]. On the other hand – application of varifocal lenses is limiting from the standpoint of inertial effects which limits the image refresh rate. Attempts to mitigate this [27] by additional optical focus tracking system makes the system more complex and comes at a cost of focal break-up of colors degrading the perceived image quality (if a field-sequential image source is used). Thus, it is evident, that there is a lack of compelling practical display technology (acceptably small form factor, good perceived image

quality) to overcome vergence-accommodation conflict inflicted limitations and widespread adaptation of individual augmented reality display devices among professionals and everyone else.

2.2. AR-HMDs based on Dynamic Scattering Volumetric Displays (diffusers)

LightSpace Technologies and EuroLCDs has a history in solid state volumetric displays developing 19-inch sized desktop displays. The general architecture of a volumetric display based on fast-switching optical diffuser elements has been more thoroughly described previously [28]. For a brief overview – the projection volume is composed of a stack of fast-switching optical diffuser elements that are driven time-sequentially. The image source is a fast image projection unit, that is synchronized with the switching of diffuser elements to output the corresponding image depth plane at each respective moment in time (see Figure 1.).
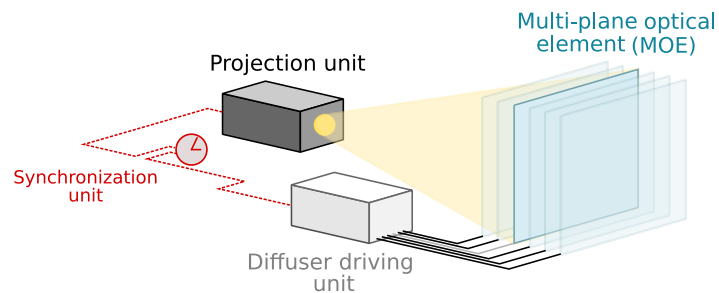
Figure 1.: Schematic of volumetric display comprised of a projection unit, a synchronization unit, the diffuser driving unit and a multi-plane optical element (MOE).

The key enabling component in this architecture is a very low response time (<500 µs) electrically switchable optical diffuser element which is used as a temporary image projection screen. The element itself is a liquid crystal-based device with two optical states – a highly transparent one and highly light scattering state (see Figure 2.).

| a) | b) | c) |
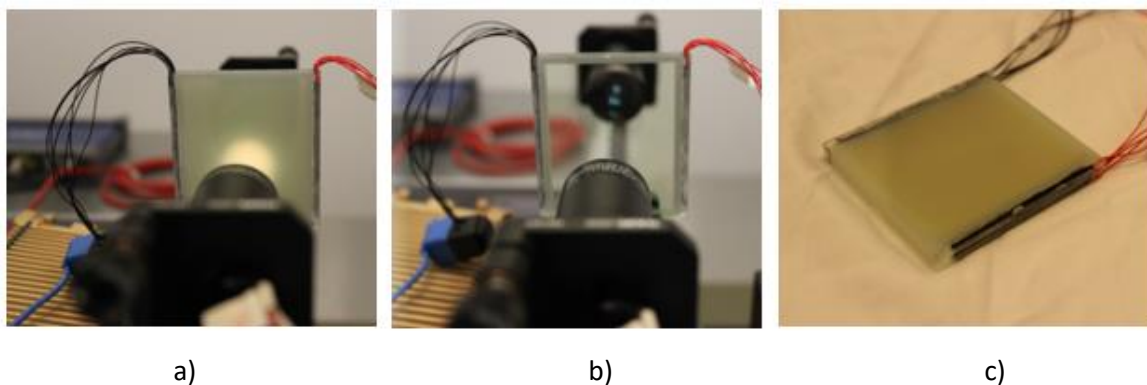
Figure 2.: LCD prototype device: a) scattering state, b) transparent state and c) stack structure from 6 laminated LCD (optical chip).

The high transparency is the main factor allowing stacking of n-elements into solid optical chip. Since 2018/2019 LightSpace Technologies and EuroLCDs have performed an initial miniaturization step from large-format diffuser elements to be used in head-mounted displays [28] and demonstrated feasibility of this approach by a prototype (see Figure 3.). Further miniaturization was planned for diffuser elements as well as miniaturization the image source – a high refresh rate image projector also had to be scaled down. Both system requirements and capabilities are intertwined, as no ready-made solutions exist, especially for projection system based on spatial light modulators (SLM).

Figure 3.: A photograph of a multifocal virtual reality headset being evaluated for the first time.

Nevertheless, SLM in the required form factor generally do not support high refresh rates needed for the multi-focal display architecture. The digital micromirror devices (DMD) by Texas Instruments (DLP 2010 in particular) is a small enough SLM (0.2" diagonal) to allow construction of a pico projector with a feasible footprint and sufficient image refresh rates (60-90 Hz in case of 4 focal planes). Also, it has several major limitations/disadvantages making the multi-focal 3D head mounted display insufficiently compelling. On one hand for AR applications **image brightness** is of very high importance as it directly determines in what environment the projected image is able to compete with the ambient illumination – or be bright enough. Digital micromirror devices are easy to couple with colored LED light sources, thus achieving high brightness. Nonetheless, the DMD is energetically inefficient, which is undesirable for mobile applications. In case only a small portion of pixels is required to depict an image – which is typical for augmented reality – the light from all off-state pixels (black pixels) is diverted into a light trap – facilitating heating. On the other hand – based on experience, users expect high image resolution but the DLP2010 supports a resolution of only 854×480 pixels which by today's standards is insufficient for most cases. Moreover – for true color representation single-DMD systems utilize field sequential color output – meaning that color break-

up is a potential artefact of image – especially so when moderate to fast head/eye movement occurs. Finally, a forced utilization of proprietary controller from Texas Instruments introduces color dithering and doesn't allow for custom control of DMD. In turn, observable color dithering interferes with the text readability on such displays. The deficiencies in projection system can be partly offset by more advanced properties of the optical chip (multifocal liquid crystal diffuser), a central part of spatial volume image forming system in both AR and VR headsets (see Figure 4.).

a)   b)
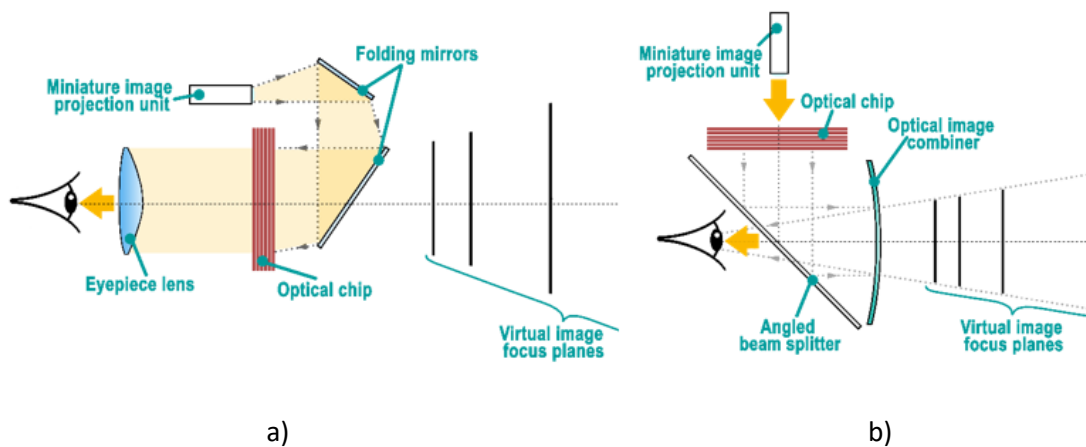
Figure 4.: Optical architectures for a) VR and b) AR.

Consequently, to facilitate further evolution of multifocal head mounted displays and provide a safe AR technology to awaiting professionals from industry to medicine and creative community, the work comprises investigation and development of a novel **miniature, high brightness, fast switching** multi-focal display chip, and validation of its performance.

The key-enabling component of our multi-focal display architecture is a proprietary fast-switching diffuser element. In the previous steps it was miniaturized from large-format to smaller 60×60 mm and now to 25×18 mm. At the latter size, cell-gap forming spacers just started to become visible upon high magnification which is essential to obtain practical field of view for the AR display device. As the task of this work is to improve the multi-focal display module architecture in all aspects – including reducing the footprint – the liquid crystal-based diffuser has to be miniaturized further. The target size is 25×18 mm or less (15x8 mm). This means that at a smaller footprint an image with higher resolution will be projected. Moreover, when mounted in an AR headset, the eyepiece optics will magnify the image to a larger extend making any **internal structural elements** (for example, spacers) even more visible. Thus, this work is oriented towards investigation of methods to achieve high-resolution capable diffuser element with 17-25 mm (0.7-1") diagonal that doesn't show any image artefacts. The work will include investigation of cell architectures with sparsely spaced

conventional spherical spacers. Moreover, methods for spacerless liquid crystal cell design when mounted in laminated stack will also be considered. The research work involves design phase from material physics standpoint, technological validation by sample fabrication and practical evaluation of the achieved image quality.

2.3 Setting up the specification of the optical chip

As could be seen in Figure 4, AR-HMDs must have sufficient optical transmittance and large brightness adjustment range, comfortable for user, to make sufficient contrast between real world and projected virtual image. In order to increase image brightness, one would select as low as possible diffuse state transmittance while keeping other properties, like switching speed and transmittance of open state in the same level. In optical chip, 4 active switchable diffuse layers are required to form volumetric image, composed of liquid crystal displays (LCD). Obviously, thicker cell gap of each LCD would give better light scattering properties. One of the first tasks is to determine optimum cell gap based on optical performance.

LCD elements (67x60 mm) with cell gap of 4, 7, 8 and 12 microns were prepared for the evaluation. The corresponding cell-gap spacer density was 260 pcs/mm^2, 147 pcs/mm^2, 136 pcs/mm^2 and 121 pcs/mm^2 respectively. All diffuser elements shared similar cell structure, homeotropic alignment and filling.

Table 1.: 67x60 mm diffuser electro-optical test results depending on cell gap.

Cell gap	4 micron	7 micron	8 micron	12 micron
Characterization voltage, V	50V	80V	90V	150V
Open transmittance, average	90.7%	90.3%	88.8%	90.9%
Diffuse state transmittance, average	39.1%	14.8%	10.7%	4.5%
Decay (90%-10%) switching time, average µs	878	732	673	665
Rise (10%-90%) switching time, average µs	1291	1408	1415	1088

As we can see from electro-optical results (see Table 1.), one would favor thicker cell gap as it would give best light scattering properties. However, we must evaluate the optical performance in relation to AR headset requirements. The results have been published [29]

For the evaluation of image quality parameters, a setup shown in Figure 5. was used. The image source was a DLP-based projection system – DLP CR4710EVM with an image resolution of 1920x1080 pixels. The test image patterns were projected onto a diffuser element, while the resultant

image as formed on the diffuser was captured by a digital CMOS camera Thorlabs Kiralux CS895CU (image resolution: 8.9 MPix) equipped with a Computar V2528-MPY lens. The CS895CU camera was interfaced to a personal computer and a real-time image stream was analyzed by a custom software responsible for MTF measurements. It must be noted, that in this experiment the performed evaluation is relative and intended for relative comparison between analyzed diffuser elements. For luminance and ANSI contrast measurements via luminance-meter LS-110 (Konica Minolta) was used. For the evaluation of spacer visibility, an additional focusing lens was placed between the projector and diffuser element to reduce the image size on the diffuser element thus matching the image size to actual size (25×14 mm) as foreseen to be implemented in a realistic design of an AR headset.
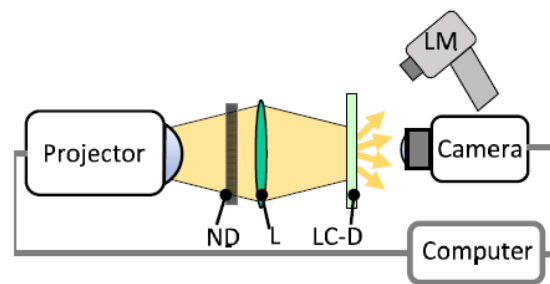
Figure 5.: Schematic of test setup for the image quality evaluation on diffuser element (LCD). In this schematic – L is an optional lens for focusing a smaller image and ND – is a neutral density filter for attenuation of incident image brightness. LM represents luminance meter.

The first experiment involved evaluation of spatial resolution of the tested diffuser elements. To ensure consistency and minimize errors associated to focusing, for every diffuser element and every measurement, the custom software was used to assist with finding the best focus (see Figure 6.). The results showing normalized threshold spatial frequency (at 50% contrast) as a function on the cell-gap (thickness of the active layer) has been provided in Figure 7.
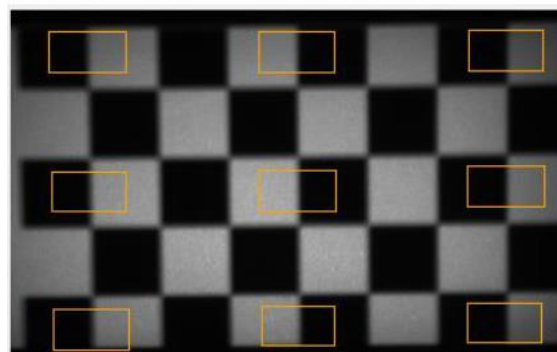
Figure 6.: A screen-shot form the custom software used in this study for determining best focus and evaluation of MTF. Depicted is the checker-board pattern commonly used for MTF measurements and ANSI contrast. Rectangular contours represent regions for automatic content detection and data processing.
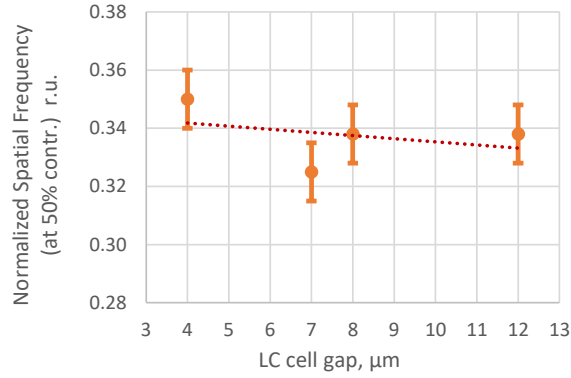
Figure 7.: Normalized spatial frequency at 50% contrast as a function of cell gap for the light diffusing element.

An overall luminance values in correlation to cell-gap of liquid crystal diffuser elements is shown in Figure 8. It must be noted that measured luminance values depend on the brightness of the image projection unit and properties of light scattering diffuser element. As the parameters of the projection unit were constant during all measurements, the variance in luminance values is attributed solely to properties of light diffusing layers.
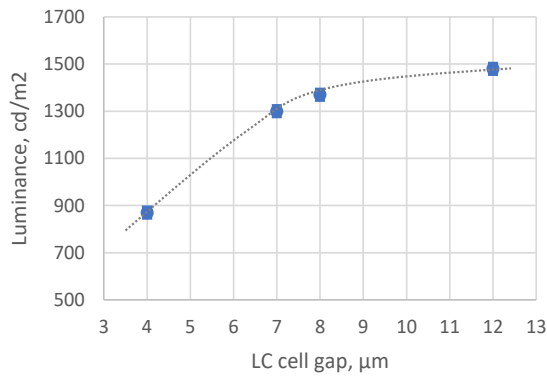
Figure 8.: Recorded luminance values on tested diffuser elements, as a white screen image is projected onto them.
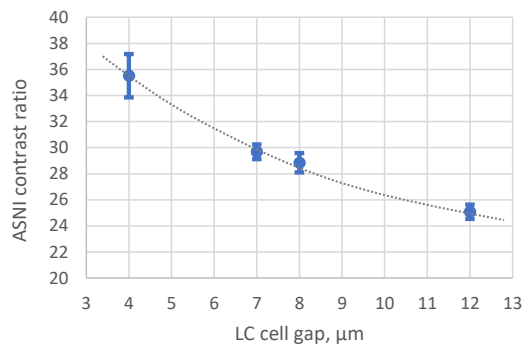
Figure 9.: ANSI contrast ratio as a function of cell gap for liquid crystal diffuser elements.

Another metric, that was registered by luminance meter was ANSI, Figure 9.
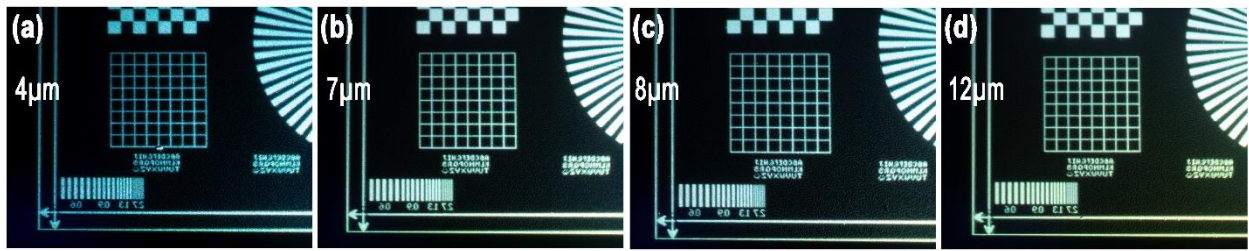
Figure 10.: Photographs showing a cropped view of a test-pattern image on diffuser elements with (a) 4µm, (b) 7µm, (c) 8µm and (d) 12µm cell gap. Pictures taken with an APS-C digital SLR camera (24 MPix effective image resolution) with a 35 mm focal length lens at a magnification close to 1:1. Shutter speed 1/50th of a second.

Besides quantitative measurements of diffuser elements, qualitative evaluation was done by photographing a test pattern projected onto every tested diffuser element. This data has been presented in Figure 10, and demonstrates a part of the projected image as observed by viewer. The photographs have been taken at similar camera parameters (similar exposure time).

The target horizontal field of view (FOV) using a "bird-bath" optical design (curved image combiner and flat beam splitter, see Figure 4b) was 40 degrees. The availability of spatial light modulators restricted the image aspect ratio to 16:9. As a result, the derived image size on optical diffuser elements was 25×14 mm. Considering a typical available resolution of spatial light modulators – 1920×1080 pixels (Full-HD) and 854×480 pixels (FWVGA), the size of a pixel on a diffuser element is around 13 µm and 30 µm respectively.

When an optical design demands a scale-down of diffuser elements, their image resolution starts to become an issue. It is desirable to maintain a surface of a pixel large in comparison to its depth. In this case by pixel size a volume of the active layer that receives a single projected image pixel is considered.

On one hand, an increased thickness of the active layer promotes better light scattering, but as determined by pixel size estimation, it starts to become comparable to the size of a pixel. Thus, this can limit spatial frequency that can be effectively shown by given diffuser due to crosstalk between neighboring pixels. As can be seen from Figure 7., there is a trend for reduced spatial frequency with increasing the cell-gap – nevertheless, it is not as prominent as would be expected. An aberration at 7 µm cell gap possibly could be attributed to quality of used spacers, which might have contributed to increased light scattering within the plane of diffuser, thus lowering the recorded contrast values. Nonetheless, the general trend is highlighted by the endpoints showing that within the verified range of cell-gaps the resolution of the diffuser element doesn't change substantially.

As the cell-thickness directly correlates with light scattering power, the image brightness on tested diffuser elements also varies (see Figure 8.). Moreover, it can be seen that there is a trend towards saturation at larger cell-gaps. Thus, it could be seen, that from the image brightness standpoint, larger cell gaps don't mandatory translate into improved performance.

Similarly, a related metric, dependent on the cell gap and light scattering properties of diffuser elements, is ANSI contrast (Figure 9.). This is an honest and representative metric of image contrast within the scene and as expected with higher light scattering power of diffuser elements, it decreases. Nevertheless, it must be noted, that a higher ANSI contrast for a diffuser element with 4 µm cell gap isn't preferable due to excessive energy expenditure which isn't used directly for recreating an image on a diffuser element. This can be seen from Figure 10., which allows visual comparison of images on all tested diffuser elements. The 4 µm version (Figure 10 a.) produces notably dimmer image, meaning that the rest of the light goes through the diffuser element un-scattered and producing a secondary image of the light source – known as a "hot-spot" in rear-projection systems [30] Thus, from practical standpoint, a diffuser element with larger cell-gap appears to be a better choice.

Figure 11. on the other hand demonstrates an even more magnified view of Figure 10., hinting on visibility of spacers.
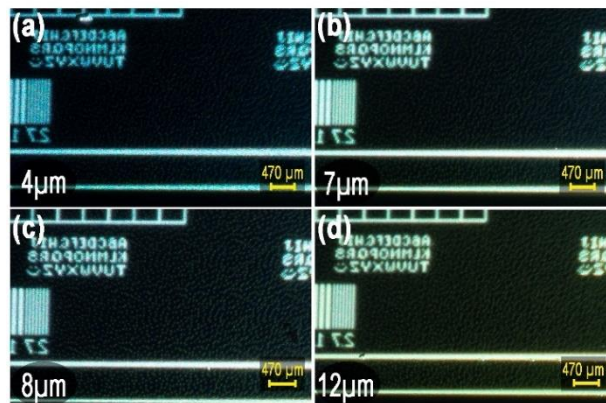
Figure 11.: Magnified view of a test-pattern image on diffuser elements with (a) 4µm, (b) 7µm, (c) 8µm and (d) 12µm cell gap.

Also – it must be noted, that actual size of spacers and their separation isn't well represented by photographs of Figure 11. due to image resolution of the camera system. A more representative image of spacer pattern is provided in Figure 12.
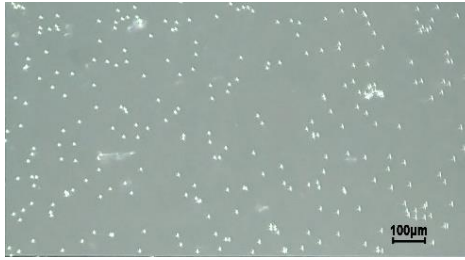
Figure 12. Micrograph of optical diffuser element with 7 μm cell gap in transparent state.

Furthermore, at the desired image size of 25×14 mm and magnification yielding a 40° horizontal FOV, the visibility of spacers could interfere with the perceived image quality. Thus, it would appear to be beneficial to keep the active layer as thin as possible. For a given image size and magnification the spacers would be seen at 23, 49, 46 and 79 seconds of arc for 4, 7, 8 and 12 μm diffuser elements respectively. Considering the maximum angular resolution of a human eye, which is around 1-2 arcminutes, it is evident, that in all cases spacers likely could not be observed. Nevertheless, for the 12 μm diffuser element, the angle at which the spacer could be observed (79 arcseconds) nears the maximum angular resolution of an eye, and thus with high probability could become obtrusive.

Consequently, for the set case, smaller cell gaps with smaller spacers are preferable. Figure 11. demonstrates a high magnification crop of an image as it is formed on a diffuser element. While presence of spacers could be observed in case of all diffuser elements, generally they do not interfere with the presentation of an image. Here an image with FWVGA resolution has been projected, and it is evident, that a single pixel can be discerned for all diffuser elements (all cell gaps). Note, that actual size of spacers and their separation isn't well represented by photographs of Figure 11 due to image resolution of the camera system.

Based on observations, it is evident that for a practical multi-focal head-mounted display with basic characteristics as defined at the beginning of this chapter, optical diffuser elements with 7-8 μm thick active layer is optimum for 4-layer element stack. The other requirements can be formulated now.

First and foremost, the physical dimensions must be smaller. The size of 16x9 mm moves into micro display manufacturing territory, setting higher requirements for technology. In the same time, optical architecture favors smaller distances between active layers. Ideally, distance should be 0.33mm, requiring display to be produced from 0.15mm thin glass substrates, practically a film like material but micro displays, typically, are made on silicon wafer. The current passive matrix LCD manufacturing line have been designed for glass thicker than 0.4mm. In this aspect smaller size and

thinner materials are contradictory to each other, and a balance must be found using other materials and technologies during this work.

Further, decreasing density of spacers in cell from current 136 pcs/mm^2 will serve two purposes: 1) it will increase image quality, 2) will increase total light transmission as they are inactive constructive element. In the same time, thinner materials will require more support elements, so that cell gap is not changed during LCD manufacturing. Again, a balance must be found.

In order to increase image brightness, we can decrease transmission loss in all materials and on their boundaries. In order to have 4 active layers (diffusers), traditionally we would need additionally 8 glass substrates, 3 glue layers, 8 conductive layers, 16 thin film internal dielectric layers, and two stacks of outer broad band antireflective layers (4-layer BBAR). Currently 33x22mm 4-layer diffuser stack with has 78 % transmission (white LED, VST-1 measurement setup, see addendum A.). We will focus on reduction of layer number (47 in total) and on index matching of layers to get higher than 78 % value.

Last but not least, electro-optical performance could be improved: faster switching and higher scattering value of the active LC layer. Faster switching will give more time for image projection, thus increasing image brightness. Higher scattering values not only will aid brighter image but may reduce "hot spot", created by non-scattered light.

The following Table 2. summarizes aims for the work which will be developed in next chapters.

Table 2.: Specified diffuser properties for the work.

Specification	Current	Goal	Chapter
Size, active area	62x49 mm	26x15 mm-16x9 mm	5
Distance between active LC layers	1.1 mm	0.66 mm	5, 6
Number of layers	47	39	4, 6
Inactive elements in size of 8µm	136 pcs/mm^2	0-100 pcs/mm^2	5
Total set transmission in open state	78%	82%	4, 5, 6
Individual unit transmision in diffuse state	20%	19%	3
Individual unit transmision in open state	89.3%	90.5%	4

3. Dynamic light scattering by liquid crystals

3.1 Literature review

Introduction on liquid crystals

The main operational part of the display is the liquid crystal, the material that exists between conventional isotropic state (liquid) and three dimensionally ordered solid crystal with only orientational order but no positional order. It combines properties of both states, such as fluidity, anisotropy in optical, electrical and magnetic properties. In the displays, the most important is that its optical properties can be directed by external electric field [31] and the low viscosity means that optical properties can be changed by relatively small force and fast. Vast range of LC types are known and used.

In this work, the focus is on LC that scatter unpolarized light in one state and be as much as possible transparent in other, and can be switched from one state to other as fast as possible. For example, author have worked with smectic-A LC that have excellent light scattering properties but the transition between switchable states is slow [32], so it is not the focus of the work.

Typical example of most common, cylindrical shaped LC molecule is 4'-Pentyl-4-biphenylcarbonitrile (5-CB), see Figure 13.
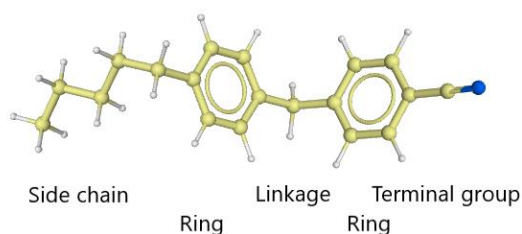
Figure 13.: Chemical structure of 5-CB with identified functional groups.

The terminal group determines dielectric constant and anisotropy, benzene rings provide short range molecular forces which affect electrical and elastic properties. Note that nonaromatic rings can also be used. The linkage group provides stabilization against ultraviolet light, moisture and chemicals and side chain influences the elastic constants and transition temperature of LC. Nematic LC lack positional order but have self-organized directional order with their long axes almost parallel, characterized with director n, which is the average direction of the molecules [31]. Due to their structure, LC have birefringence, namely two direction-dependent refractive indexes, ordinary n_o and extraordinary n_e. The difference between can be positive or negative. Rod like molecules like 5-CB, have positive values, see Figure 14 while chiral molecules have negative values.

The optical anisotropy of LC can be increased [33], by

- replacing saturated aromatic rings with the unsaturated ones;
- with the elongation of the conjugation link parallel to the long molecular axis;
- by increasing the values of the order parameter S or decreasing the value of temperature;
- by shortening the alkyl chain of the end molecular groups in homologous series in the form of even-odd alternation.

In theory one would want optical anisotropy as much high as possible but for practical reasons (stability, switching threshold) the difference between directions Δn is ~ 0.2.
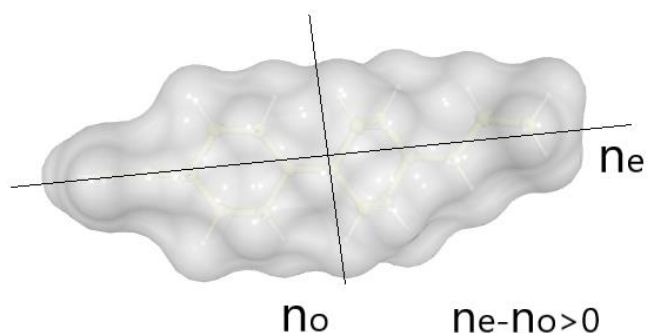
Figure 14.: Illustration of LC refraction indices of 5-CB.

Dielectric properties determine how polarization of the molecules happen upon application of electric field. Two directions are used, parallel to LC director and perpendicular. The difference between dielectric permittivity in those directions can be either positive or negative, meaning that in positive value, molecules align themselves parallel to electric field.

The speed how molecules react to external field is dependent on their viscoelastic properties. The phenomenological rules are [33]:

- Alkyl end groups provide lower values of viscosity than alkoxy and acyloxy end groups.
- The viscosity is lower for shorter molecules.
- Introducing the rings with heteroatoms increases viscosity compared to phenyl analogues.
- The most viscous bridging groups are the ester group ▬COO▬, the simple bond (as in biphenyls) and the ethane group ▬CH=CH▬.
- Replacement of phenyl ring by a trans-cyclohexane ring results in reduced viscosity values.

It should be noted that the final properties on LC composition is composed of multi molecules. Changing content of one or more component will lead to change of overall dielectric property, temperature range or viscosity. The cyclohexane derivatives often serve as components that lower overall viscosity of the LC mixture. Once these options are exhausted, the only way is to work on surrounding solid state and electric field interaction.

Dynamic Scattering Mode

When a voltage is applied to liquid crystal device, two effects can happen – current effect and field effect. Historically first displays were operating in dynamic scattering mode (DSM) where current generated turbulence to scatter light, see Figure 15. Nowadays all displays currently uses field effect so a dielectric layer is needed [17] between LC and electrodes.

1) V=0   2) Voltage V>V_c 3) Build-up of space charge

4) Williams domain V≥V_c 5) Turbulence-Dynamic scattering V>>V_c
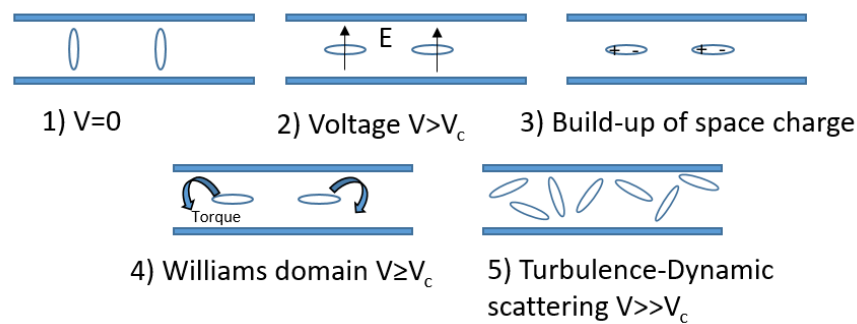
Figure 15.: Dynamic Scattering Mode display operational principle. V_c – critical voltage.

Cholesteric Liquid Crystals

Cholesteric LC are composed by chiral molecules and they were next LC type that was used for light scattering. Initially first discovered were cholesteric molecule derivatives, giving the name of class. Cholesteric LC can be composed by chiral nematic molecules or formed by adding chiral dopant to nematic LC mixture.

Twist in LC structure happens with alignment between molecules with slight angle to one another producing quasi nematic layers. Their individual directors are turned by a fixed angle form one layer to another. The pitch (P) is the distance over which the director of LC molecules undergoes a full twist of 2π angle. As the phase directors at 0° and 180° are equivalent, the arrangement of molecules in the chiral nematic phase repeats at every half pitch (P/2). Due to this strong twisting effect, cholesteric LC shows a selective reflection of the circularly polarized light of wavelength equal to pitch length [34].
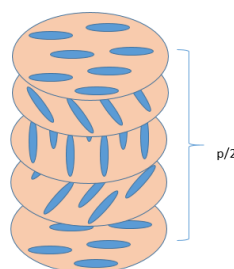
Figure 16.: Cholesteric pitch formation.

The cholesteric mode has two distinct stable states, the planar (**P**) and focal conic (**FC**) states. In planar state, all helical axes align normal to the surfaces. In this state, it is Bragg reflector [17], see Figure 17.

a) FC state   b) planar state   c) homeotropic state
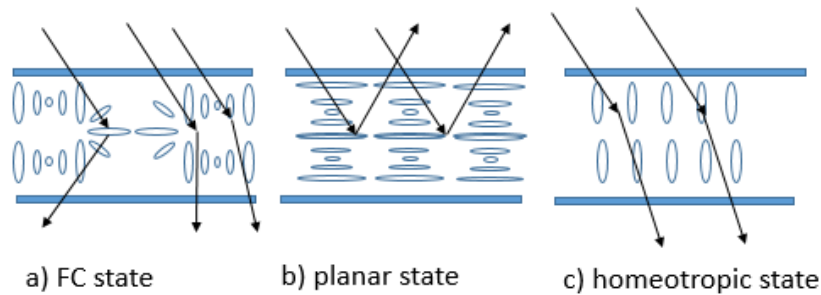
Figure 17.: Illustration of Focal Conic (a), planar state (b) and homeotropic state (c).

Upon application of electrical field, the change from planar to focal conic state happens. The texture is strongly forward scattering and selective reflection property vanishes. Presence of microdomains, formed by suitable prepared polymer network, results that LC tend to keep helical structure and the directions of helical axes are random, in the absence of electric field. Formed microdomains strongly scatter incident light [34], and this is the principle for polymer stabilized cholesteric displays, see Figure 18.

a) Voltage applied   b) Voltage off
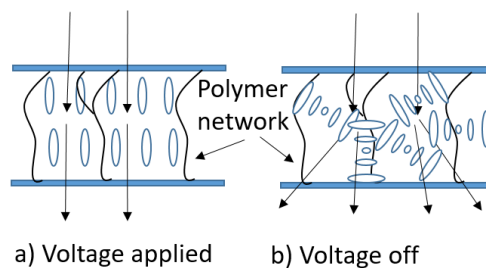
Figure 18.: Operation principle of polymer stabilized cholesteric LCD.

If electric field is slowly decreased, transition back is not homogenous, but instead is nucleation process that starts at defects in the sample such as spacers and the strands of the polymer network. The focal conic texture grows from just a few places so it forms larger domains. If the voltage is removed suddenly, the domains form in many more places at once and therefore the average domain size tends to be smaller, which results in better light scattering [35]. This transition has been studied and transient planar scattering states (**TP**) have been identified [17]. There is also the fourth state, homeotropic (**H**) induced by electric field where no twist happens and all directors are pointing perpendicular to the substrate plane. The transitions between states are shown in Figure 19.
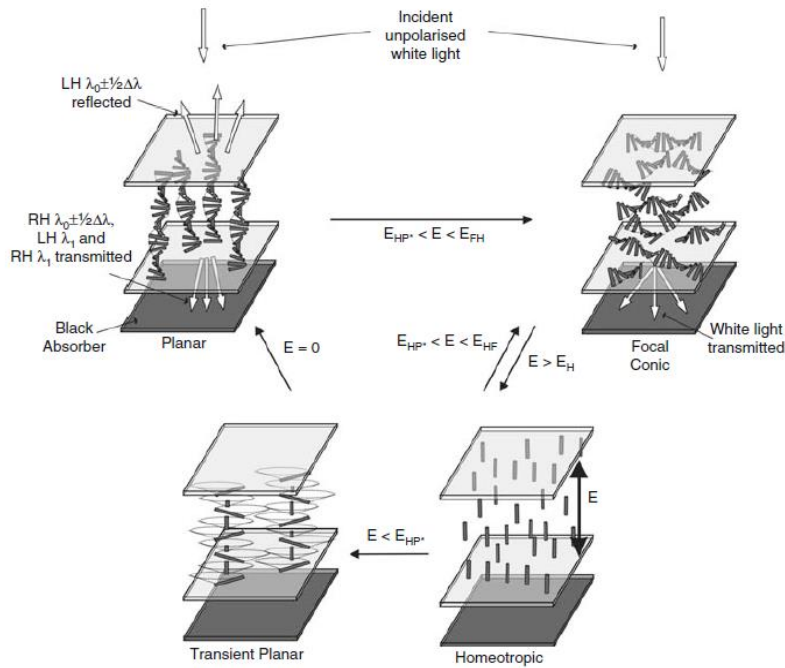
Figure 19.: Transitions between cholesteric LC states [3.8].

In one of the first research [36] on this subject, Watson reports that surfaces (planar or homeotropic) do not influence the time needed to switch from the **TP** state to the **P** state. By measuring reflected light at certain angle the **TP** and the **P** states are identified by their specific reflection at certain wavelength. Thus, the **TP** state has distinct reflection peak at 950 nm and minor peak at 450 nm. After 5ms, disappearance of these peaks is observed as well as rise of another reflection peak at 610 nm, characteristically for planar orientations.

Two-dimensional computer model was used to verify the proposed transformation model [37]. According to this model, once the field is removed, LC drops to a state in the plane of the cell but with non-equilibrium number of twists. In order to relieve this high-energy state, sinusoidal modulation forms, and after sufficient amplitude, leads to buckling and folding of the layers and formation of l-layer defects. This highly disordered state is characterized by equilibrium pitch. Uniform regions grow leading to final transition to the P state. In addition to previous studies using only reflection measurement, Watson uses photography to measure domain sizes and light scattering measurement to establish that the typical domain size is about 5 μm. Most important, the definition of domain is given as "area of uniform colour and brightness under observation by microscope between crossed polarizers". 100-400x magnification is used.

Capacitance measurements were used to further verify the optical results in this work. Shortly after voltage is removed, large capacitance is detected, which is consistent of the LC being in homeotropic state. Then the capacitance drops to a minimum value at about one millisecond,

corresponding to the TP state, where the majority of the material is in the plane of the cell. Over the next 30 milliseconds, capacitance raises again, suggesting that the director is no longer in the plane of the cell. This is in agreement with the optical measurement results [37].

Microphotographs and observing colour change during the transition process from the **H** state is used, starting at 1 millisecond and resulting in stable green colour after 35 milliseconds, when the **TP** state is observed. Further transition process is characterized by initial violet stripes perpendicular to rub direction and final lavender colour for equilibrium **P** state. This confirms that both states have planar orientation. For isolated system, it would apparently seem easier to go directly to **FC** state, where directors exhibit twist about some axis, approximate parallel to the surface. The simulations are backed up by the experiments. To obtain the **FC** state, it is necessary to drop the voltage not to zero but to some intermediate bias voltage. The reflection results in planar cells agreed with simulations. However, a difference can be seen in the homeotropic cells. Watson supposes that the LC elastic constant ratio assumed in simulation is different than in the experiment and un-expectedly observed reflectance peak in blue is due to multiple off-axis reflections, causing blue shifting of reflected light for homeotropic cells.

The research is continued in Anderson work "Transitions from the homeotropic state in cholesteric liquid crystals", 2000. The author [38] uses newer simulations and explains that the system is winding up from the planar surfaces and there is a region of homeotropic orientation in the middle. This homeotropic region allows the twist at the edges to become tighter as it tries to reach initial pitch. This happens evenly throughout the cell, and is opposed to previously held theory that the small regions of correct twist nucleated and then grew based on defects with isotropic cores. Anderson observes significant effect of spacers and surface irregularities on the speed of transition and proposed polymer wall technology to control the interruption of the director field. This led to the development of polymer stabilized cholesteric texture displays (PSCT) at the Kent State University. Both Anderson and Watson work is part of a fundamental knowledge in the display industry, for cholesteric LC application mode. This is also closest fundamental research to LC mode used is this work.

Liquid crystal backflow

When LC orientations are manipulated with the help of electric field, LC backflow effects must be taken into account. Splay and bend deformations of LC are always accompanied by a macroscopic flow of liquid crystal with velocity V=(V(Z), 0, 0), due to a change in position of the centers of gravity of the molecule. If the surface orientation (for example in twisted nematic (TN)) cells are antiparallel, this creates counter directional flow inside the LC layer that slows down switching speed see Figure

20., so in electro-optical (E-O) response this is typically observed as transient peak. This effect can be mitigated by antiparallel orientation of surfaces. Then all flow inside LC layer is unidirectional, facilitating faster switching speeds.
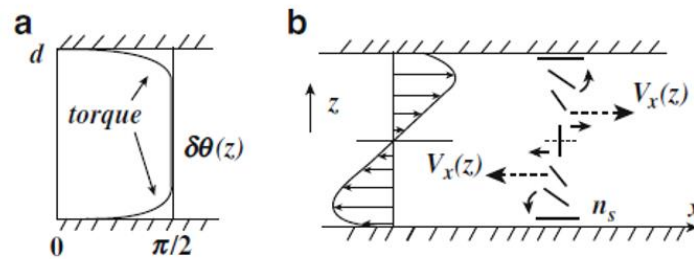
Figure 20.: Backflow effect. The profile of the director in he director in the field-on regime with steep parts close to interfaces at z=0 and z=d (a). The direction of the torques is shown by small arrows in the right part of the sketch (b) and a profile of the velocity is shown by thin arrows in the left part of the sketch. The strongest velocity is in the middle of the cell (dash arrows)[39]

Polymer Dispersed Liquid Crystals

When the polymer is homogenously mixed in LC, it provides mechanical and structural stabilization to LC devices. Depending on concentration, it can be classified as polymer stabilized (~10% concentration of polymer, PSLC) and polymer dispersed (equal concentration of polymer, PDLC) display mode. Only PDLC work with unpolarized light [17] and they were first used for 3D volumetric devices as LC diffusers, see Figure 21.
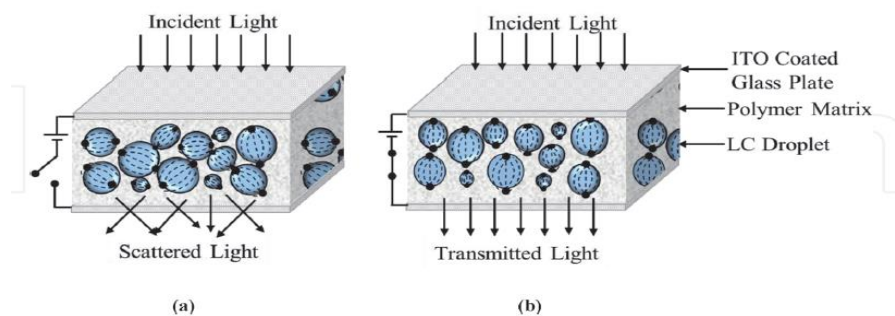
Figure 21.: Operational principle of PDLC diffuser [34]

PDLC have micron sized LC droplets, randomly dispersed and embedded in optically isotropic polymer matrix. For LC with positive birefringence in the absence of electric field, LC inside droplets is randomly oriented and incident light repetitively will refract/scatter at multiple polymer-LC interfaces. Upon application of electric field, LC in droplets align to the direction of field, and if refractive index of polymer matches the ordinary index of LC, all incident light is transmitted through. Similarly, negative birefringence material can be used with corresponding polymer refractive index. Here light

reflection is based on Rayleigh scattering [34]. Despite apparent simplicity (no LC alignment surfaces required) and possibility to be produced in larger sizes, PDLC have disadvantages related to polymer use. Haze is observed as the droplets is not perfectly round.

Polymer-free Liquid Crystal (PFLC) diffusers

Polymer-free Cholesteric Textured mode was first described in patent [40]. The electric field untwists the chiral nematic or cholesteric liquid crystal molecules and homeotropically aligns the liquid crystal directors to transform the liquid crystals into a transparent homeotropic state. When electric field is turned off, the liquid crystalline material forms microdomain textures and scatters light. Authors claimed that, although the directors within each micro domain are ordered (i.e., short range order), they are disordered with respect to other microdomains. This localized chiral domain formation was believed to contribute to the observed transient shuttering effect.

PFLC cells, can be considered as evolution step of PDLC cell [18]. The polymer structure inside cell is absent and faster switching speeds are observed as well as improved scattering properties, see Figure 22. PDLC cells use relative long cholesteric pitch, whereas for PFLC short pitch <500 nm is required. Polymer free and PDLC diffuser E-O responses are similar, see Figure 22. but there are differences.
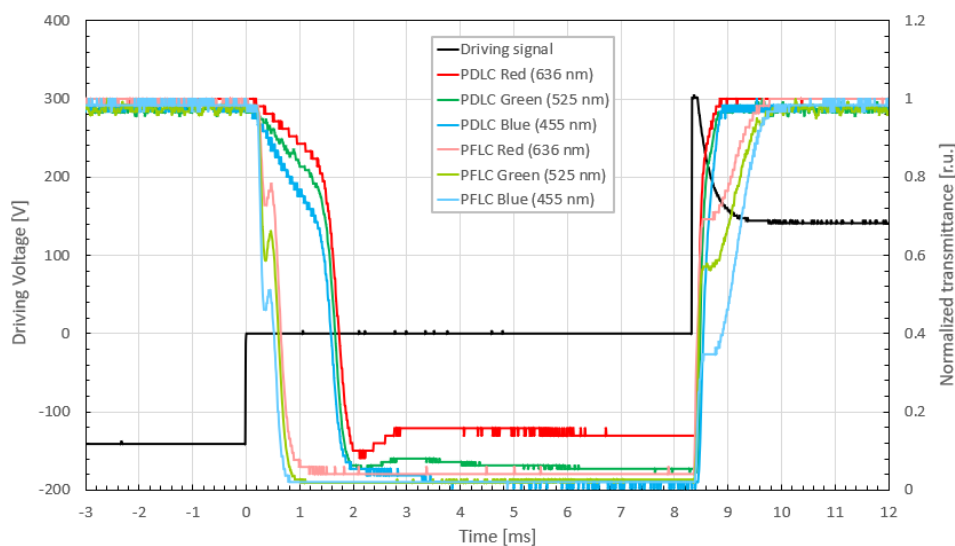
Figure 22.: Dynamics of electrical and optical signals for PDLC versus PFLC diffuser with a 15µm active LC layer measured with 3 wavelength laser system.

The minimal transmissive state (transient focal conic) is not stable and scattering state degrades over time into static focal conic state, see Figure 23. This limits PFLC uses for short light diffusing periods. The later research studies [41] for these diffusers proposed that transition from clear

homeotropic state (**H**) to diffuse focal conic (**FC**) state occurs via metastable planar state, in analogy to PSCT, as transient raise of transmittance is observed, see Figure 22. (**H** -> **FC**).
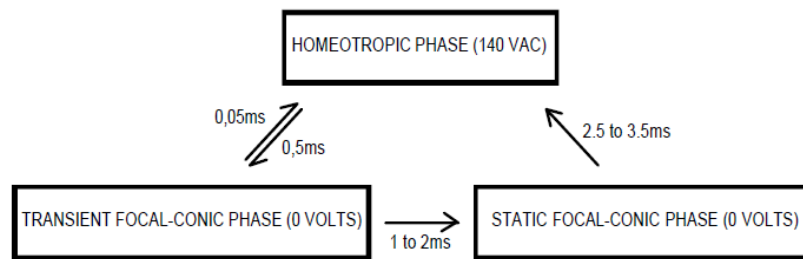
Figure 23.: Schematic diagram showing the switching characteristics between various textures for PFLC [41].

LC refraction indices and layer thickness

LC, like any material in optical device, must be characterized for device design and optical performance optimization. LC refraction index (RI) dispersion over spectra can be measured by multi-wavelength Abbe refractometer [42]] or using the spectral reflectometry method [43]. The spectral reflector meter processes the light spectrum reflected or permeated by the sample. If the sample consists of a multilayer system in which multiple internal reflections occur, the interference bands may be observed in the spectrum, whose position is determined by the optical properties of the investigated layers - thickness and refractive index. In the Institute of Solid State Physics this method is used to determine the refraction indexes of 1 μm thick layers [44].

We have optimized LC mixture for fast switching, and its refractive index dispersion is unknown. In the same time, unlike solid materials used in LCD construction, LC layer thickness can vary. Its exact determination is one of the critical measurements in display development and manufacturing as it determines both transmission and switching speed. In LCD production process liquid crystal layer thickness between both sides of display glass is formed during vacuum assembly. Thickness is controlled by adjusting spacer size and liquid crystal volume inside the cell. There are deviations caused by liquid crystal dispensing process and evaporation rate in vacuum during assembly process which decrease production yield or lead to variations in optical properties. Excess of LC can also cause visually distinct regions in lower part of display during intense use, called "gravity mura" [45].

Methods for determination cell gap using light polarization are well developed and commercially available but does not work for scattering type or other special type LCDs [46]. Spectroscopic method can be used to measure LC layer thickness based on transmission spectra measurements where interference is created by different layers with different thicknesses and

refractive indexes. By using mathematical methods, cell gap and RI can be calculated from transmittance spectrum [42]. Yet this requires the refraction index to be known first. If gap (layer) is filled by air instead of LC material, the interference peak determination is easy but it is commonly known in the industry that cell gap for unfilled displays is larger than for filled displays, up to 20%. After the layer is capillary-vacuum filled, extra pressing step is required to planarize the glass substrates and to bring filled layer to final value, when glass is resting on cell gap spacers. So, the layer thickness measured for unfilled displays is not valid any more. For more modern manufacturing method "one drop fill" display liquid crystal layer thickness is directly formed in vacuum with LC drops present, so the layer thickness is dependent on dispensed LC volume.

To overcome these limitations, scanning white light interferometric method was proposed [47]. While capable of determining liquid crystal layer thickness of different display types, it is not yet tested for scattering type of displays.

Additional challenge is the requirement to measure diffuser LCD in transparent mode after all production steps have been finished, as scattering mode typically hinders spectroscopic determination.

Capacitance measurement in contrary can more easily be integrated in production process as it is more simple technique. Display capacitance is dependent of liquid crystal layer thickness, and from its measurement one can compare one display to another in the same series, on condition that other parameters are constant and controlled. It might provide convenient method for in-line process control, and if exact dependence is known, even absolute liquid crystal layer thickness values can be obtained. Display modeling by finite elements method can provide values of capacitance dependence from liquid crystal layer thickness so precise model of capacitive and resistive structures must be built. COMSOL Multiphysics software frequently is used for modelling complex capacitive systems in displays [48]. Use of software allows to model displays with more complex electrode geometries like interplane switching electrodes or raised (slanted) electrode regions.

3.2 Aim and objectives of the research

Recall the aims for the work, defined in previous chapter - faster switching and higher scattering value of the active LC layer. In previous work LC composition itself has been optimized for speed, scattering and temperature range, leaving few open questions [18]. Can we speed up the switching speed in regions where it is slower, and what is the cause for "hot spot" (red wavelength bleed through) with projection systems? Can we improve E-O performance by changing soft matter physics interaction with solid state components?

Switching time from diffuse state to transparent (raise time) can be improved by driving conditions. The driving waveform effect on diffuser switching was reported by my colleague [49] in his master thesis and will not be repeated here. In short, raise time can be shortened by increased voltage if dielectric breakdown does not occur.

On the contrary, switching from transparent state to diffuse state (decay time) happens after the electric field is switched off and therefore cannot be manipulated by driving conditions. For application both speeds are important, as longer one become limiting factor. Hence, shortening of the fall time is the objective.

If we look at the electro-optical response curve, we see after 300-350 µs a peak, that was previously [41] described as metastable transient planar state, based on similar phenomenon for cholesteric displays. Does it slow down transition? Is it caused by backflow, current reversal, scattering center formation or transient planar state? At the first glance, it is counterintuitive, that the transition from homeotropic to transient focal state goes through planar state. For cholesteric displays it indeed happens this way, and it is confirmed by both simulations, experiments and measurements. The same methods (capacity, reflection measurements) will be used in this case.

Typically for commercially available LC components and mixtures, refractive indices for one wavelength are available. For precise diffuser stack calculations, LC RI dispersion values must be determined. Besides, to increase diffuse properties considerable amount of chiral dopant is added to the LC that might change final values. In order to measure refractive indices, LC must be measured in working device, with precisely known LC thickness (cell gap). Spacers is used to control the thickness but they compress (or decompress) to some value during production. So, initially we need to measure precise cell gap of diffuser. For LCDs working with light polarization, many methods are known [46] and some are commercially available. For dynamic scattering LC devices, a new method must be found.

3.3 Experimental part

Device preparation and characterization techniques

Diffuser cells with corresponding cell-gaps of 4-25 microns were prepared using two 0.55 mm thick plane parallel glass substrates separated by divinyl-benzene spacers. The glass substrates were coated by thin transparent conductive layer of indium tin oxide (ITO) with the corresponding sheet resistance of 80 Ω/□. Surface alignment layers were prepared from commercially available poly-imide materials from Nissan Chemicals by flexo-printing method. Alternative alignment layers were prepared from Si targets in oxygen atmosphere using physical vapor deposition (PVD) equipment or chemical vapor deposition (CVD). Rubbing was used to provide directional alignment with rayon cloth if cell design required preferred LC orientation. Cells were assembled in industrial LCD manufacturing line by using one drop fill (ODF) technology. Nematic liquid crystal mixture was doped with optical dopant having high helical twisting power. Concentrations of the chiral dopant were higher than typically used in PDLC technology, and were initially dissolved in acetone, then mixed with liquid crystal mixture and refluxed for several hours to remove acetone. Electrical connections were attached to ITO layer by means of ultrasonic soldering to keep contact resistance minimal.

Electro-optical response was characterized by VST-1 (white LED light source), VST-2 (3 laser beam system of wavelengths 635 nm, 532 nm, 450nm), VST-3 (spectrometer), see addendum A. Haze measurements were carried out using CHN Spec Haze Meter TH-100 and similar electronics for cell driving.

A programmed voltage waveform from the lock-in in-built function generator was amplified and then applied to the electrodes (ITO glasses), see Figure 24. If not noted specifically, 0.1 ms overdrive length was used to facilitate faster switching. Drive voltage is supplied for 8.33 ms.
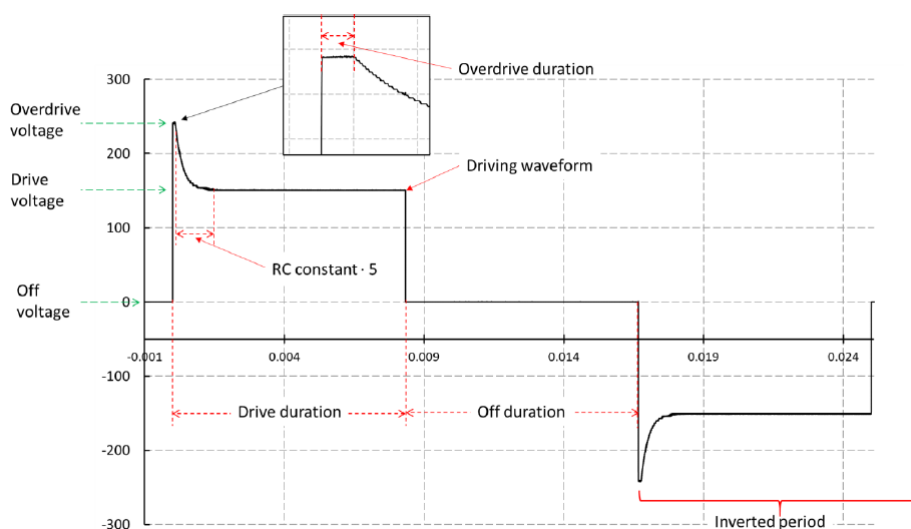
Figure 24.: Typical waveform used for characterization.

Diffuser switching times

To determine the dynamics of how a diffuser-element scatters light, VST-2 setup is used, as it closely resembles RGB projection system in AR-HMDs. The diffuser transition between transparent and opaque states is driven by applying a voltage across the diffuser-element, which is also used for triggering the oscilloscope as the applied voltage is removed. The optical response to the external field and definitions of rise and fall time can be seen in Figure 25.
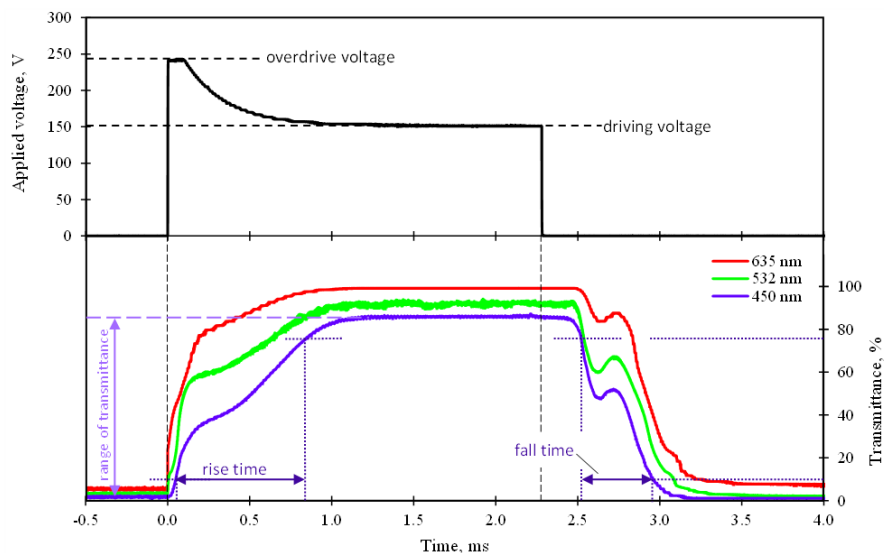
Figure 25.: Dynamics of electrical and optical signals for a large form-factor diffuser-element with a 12 µm active LC layer. Characteristic parameters – rise and fall times – shown for 450 nm optical signal.

After the removal of the external electric field, up to around 250 µs are required for the microdomain nucleation seeds to form at a room temperature. During this delay period the light transmission remains constant and scattering of light begins only after this period. The highly scattering state is reached swiftly – typically the fall time is on the order of 400 – 800 µs. As can be seen in Figure 26., this is a metastable focal conic state which is characterized by a small domain structure and is relatively short-lived. The exact time depends on the particular composition of the active LC layer, but is on the order of tens of milliseconds; after this time the domains grow and the light-scattering power decreases significantly.
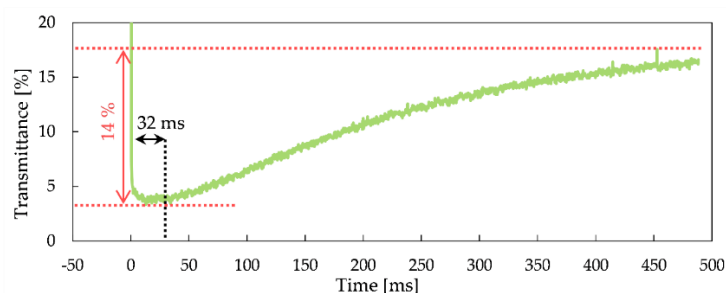
Figure 26.: Change in direct optical light transmission of a polymer-free LC diffuser element over time after the onset of external electric field-off condition. White LED used as light source (VST-1).

For a typical cholesteric (long cholesteric pitch) LC crystal cell, the switching behavior is dependent on the driving voltage (electric field intensity) – with the increase in voltage the rise time shortens but the opposite process or fall time expands. In contrast, for PFLC cells with short cholesteric pitch) a fall time is virtually independent of the driving voltage, see Figure 27.
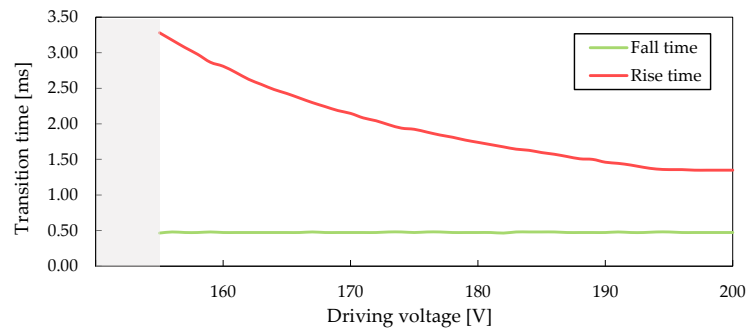
Figure 27.: Dependence of rise and fall time of LC diffusers on applied driving voltage, white LED as light source.

The polymer-free variant of a LC cell typically facilitates faster state-transitions from **FC** to **H** state due to lack of additional polymer-LC interfaces translating into improved overall transparency without sacrificing the scattering properties. However, the switching time of a diffuser-element is also dependent on LC active layer thickness. For twisted nematic LCs, the decay time is proportional to the square of cell gap [50] (meaning slower switching for larger cells) under the condition that $U_{drive} > U_{threshold}$, however, as can be seen in the image below (Figure 29.), for the induced cholesteric LC fall times slightly decrease when cell gap is increased – this is due to diminishing surface interaction effects. This is in accordance with the fact that for $U_{drive} \gg U_{threshold}$ the relaxation speed is independent of cell gap [51]. It should, however, be noted that the fall time in Figure 28. is not the time taken for the **FC** state to completely replace the **H** state, but rather, due to requirements for developing a volumetric display, the time taken to reach 10% transparency after removal of external field.
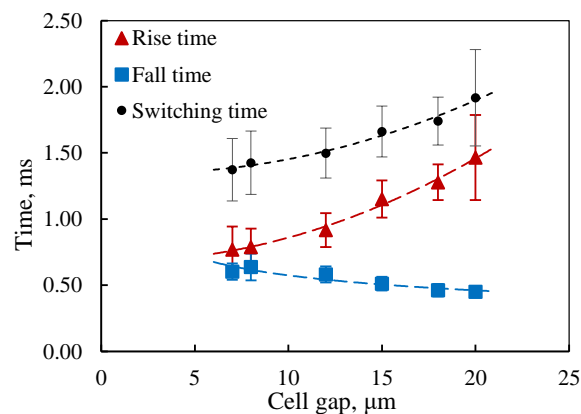
Figure 28.: Rise and fall times for diffuser-elements with different cell-gaps. The total switching time of a diffuser-element increases with the cell-gap.

Ideally, the sum of rise and fall times (switching time) should be as low as possible. Since rise times increase more rapidly with the cell gap size, smaller gaps are favorable. However, the total switching time for cell gaps in the 8 to 12 µm range are very similar, so any of these can be used based on other relevant parameters without sacrificing the refresh rate of the display.

For cholesteric liquid crystals in the transition (rise time) from the focal conic (**FC**) state to the homeotropic state (**H**), the critical field for unwinding of a cholesteric spiral [17] is:

$$E_c = \frac{\pi}{P_0} \cdot \sqrt{\frac{K_{22}}{\varepsilon_0 \Delta \varepsilon}},$$

(1.)

where P_0 is helical pitch at zero field, K_{22} twist elastic constant, $\Delta\varepsilon$ is dielectric anisotropy and ε_0 vacuum permittivity. As we can see from (1.), decrease of the pitch from 10µm (like in PDLC) to 0.4 µm (PFLC case) will raise threshold electric field intensity 25-times requiring higher driving voltages and additional countermeasures against dielectric breakdown of a cell. During the relaxation process from H to FC state the cell, the liquid crystal under-goes bulk structural changes, due to restoring of helical molecular order and formation of transient structures as well as due to the material flow accompanying these changes. This process is considered as nucleation at seeds, present onto the solid surface of the confining substrates [52], [53], or at the cell spacers and generated disinclination lines during the relaxation.

The transition time from H to FC state is approximately given by [17]:

$$T_{HtFC} = \frac{\gamma L}{K_{22}},$$

(2.)

where L is average linear distance between nucleation seeds. As it was shown in [[52], [53]] the relation process depends strongly on the surface anchoring conditions.

Thus, raise time or the transition from the **FC** to **H** state can be controlled to a degree. According to [31], raise time is

$$\tau_{raise} = \frac{\gamma d^2}{K_{22}\pi^2[(V^2|V_{th}^2) - 1]},$$

(3.)

where γ is a rotational viscosity, d is a cell gap, V – driving voltage and V_{th} – threshold voltage. Selecting a liquid crystal with the lowest possible rotational viscosity (at a given normal working temperature) and high K_{22} we have a driving voltage as a lever to control the rise time.

Increasing the driving voltage reduces the time of transition from the **FC** state to the **H** state (see Figure 22.), however it also increases the likelihood that the LC cell will undergo electrical breakdown, especially when threshold voltage is already high. The field value at which the dielectric breakdown occurs is dependent on materials used (especially protective dielectric layer, see chapter 4) as well as the overall quality of a given cell. Typically, dielectric breakdown has been observed to occur at around 10 to 25 V/μm in the LC [54].

All experiments described are performed at a driving voltage U_{drive}=cellgap·10 V/μm and an overdrive voltage of $U_{overdrive}$=cellgap·20 V/μm unless otherwise noted (see top half of Figure 24). With suitable dielectric breakdown prevention measures, driving voltage can be increased few times and rise time can be shortened, even up to 6 μs.

However, this is not possible for a fall time of a transition from the transparent **H** state to the **FC** state, as it depends on the particular LC formulation (will not be addressed here as it was optimized before this work) and chiral agent system as well as the geometric dimensions of a diffuser-element, but for a given element not much can be done to change this time (time taken for the diffuser to undergo a change in transmittance from 90% to 10% of its full range). With the external field removed, the LC relaxes back into the **FC** state. Higher temperatures can facilitate this process but, assuming most applications require the display to work at room-temperature, such an approach is highly limited.

In **H** state an electric field ensures that the elastic energy of induced cholesteric LC, see equation 4. [17], is compensated by an electric field.

$$f_{elastic} = \frac{1}{2}K_{11}(\nabla \cdot \vec{n})^2 + \frac{1}{2}K_{22}(\vec{n} \cdot \nabla \times \vec{n} + p_0)^2 + \frac{1}{2}K_{33}(\vec{n} \times \nabla \times \vec{n})^2, \quad\quad (4.)$$

where K_{11} splay, K_{22} twist, K_{33} bend elastic constants, $\vec{n}$ is liquid crystal director, p_0 the distance over which liquid crystal director twists by 360° (helical pitch). Number of diffuser cells with different dopant concentration in LC were prepared and characterized. As we can see from results see Table 3, after maximum scattering is achieved, there is maximum workable concentration, after which switching time increases again and later scattering start to decrease, due to oversaturation by the dopant. It should be also noted that for such oversaturated systems switching speeds slow down most likely due to increased viscosity of the mixture and recrystallization of a dopant within a cell. Obviously, dopants with high helical twisting power (HTP) are preferred as this allows lower concentrations to be used. S-5011 is one with of the highest available HTP and is used here.

Table 3.: Dopant concentration effect on diffuser E-O properties.

Dopant S-5011 concentration, w%	Clear state transmittance, %	Scatter state transmittance, %	Fall time, us	Raise time, us
0	86.4±0.2	85.5±0.4	527±271	0±56
0.5	87.0±0.2	86.0±0.2	857±407	3±0
1.0	86.3±0.2	67.1±0.1	519±6	116±6
1.5	77.9±1.2	36±2	1219±4	2720±68
2.0	87.2±0.4	3.0±0.1	1118±8	1631±9.2
2.5	85.9±0.2	2.3±0.3	756±5	1727±24
3.0	87.3±0.1	5.7±0.1	543±0	1884±22

For a further fall time reduction, mechanism of **FC** state formation and any transient transformation states have to be understood.

Focal conic state

Although the highest light scattering power of a diffuser element is maintained for a limited time, it is more than plenty for applications in a time-sequential volumetric screens – including multi-focal near-eye display architectures. For example, considering 4 image planes and an image refresh rate of 60 Hz (240 Hz total), the maximum time-slot devoted to a single frame is 4.16 ms. That is – in practice the limiting factor for time-sequential volumetric display architectures is the switching time (rise time plus fall time) not the longevity of superdiffusive state [55]. Even considering the lower threshold for a flicker-free (or flicker-tolerable) representation of a 3D image, a volumetric refresh rate of at least 50 Hz is required. The critical flicker fusion threshold is determined to be around 40 Hz [56], but can vary considerably based on multiple factors [57]. With this condition a volumetric screen with 20 depth planes would cycle through one frame within 20 ms leaving just 1 ms time-slot per each diffuser element. This only highlight, that volumetric screen applications require virtually instantaneous switching to maximally utilize available time slots for the projection of graphical information and minimizing the "dead-time".

The fraction of unscattered light transmitted in the diffuse state depends on the cell gap of a LC cell. From the data (Figure 29.) it can be seen that there is a relation – the larger the cell gap, the smaller transmission in the diffuse state. Small cell gap diffusers have a pronounced high transmission in the diffuse state.
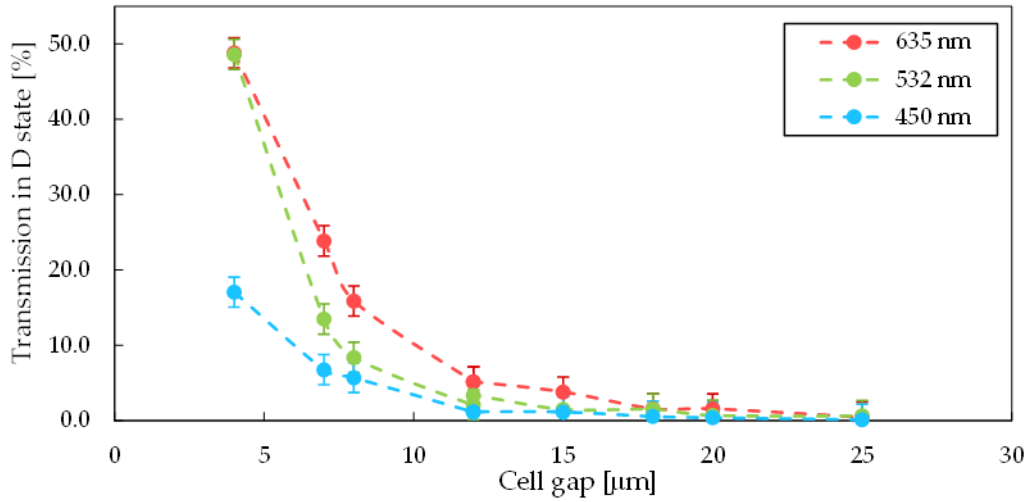
Figure 29.: Transmission in diffuse (FC) state, depending on cell gap and wavelength.

A related trend between a cell gap and haze values within the diffuse state can be seen in Figure 30. With growing cell gap – haze values also increase. The saturation of haze starts at around 12 μm cell-gap and further increase of haze is a slow asymptote towards 95.77 %. It is important to mention, that these results could be impacted by the switching speed kinetics. A cell with larger rise times could spend less time in transmission state and therefore give elevated Haze values.
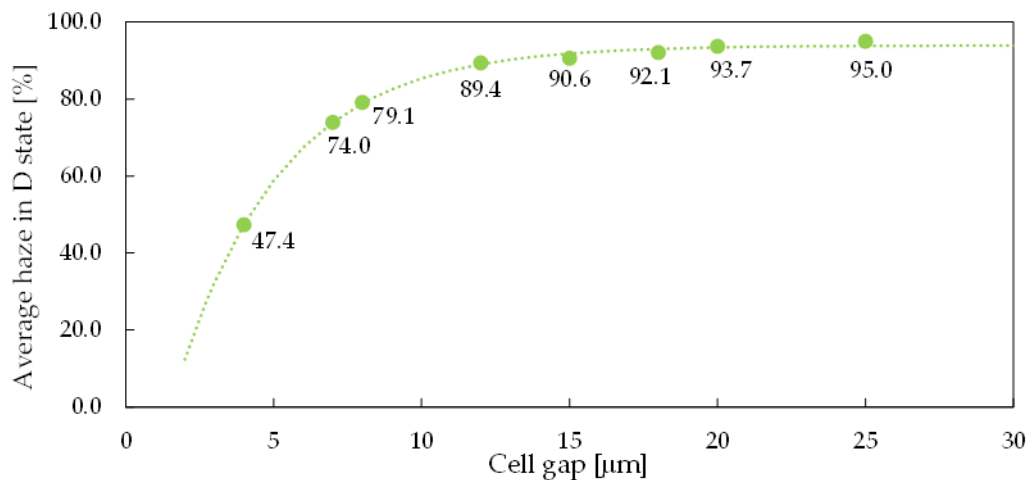
Figure 30.: Diffuse (D) haze measurements for various cell gaps.

Diffuse state transmission and haze properties have strong correlation with viewing angle. Overall, increasing the cell gap also increases the viewing angle for all 3 wavelengths, see Figure 31. From 12 μm to 25 μm cells. The red (635 nm) wavelength has the narrowest viewing angle, while the blue (450nm) has the widest viewing angle. For the 4um cells it is reversed – the 635nm has the largest viewing angle. 7um and 8um cells are in transition region.
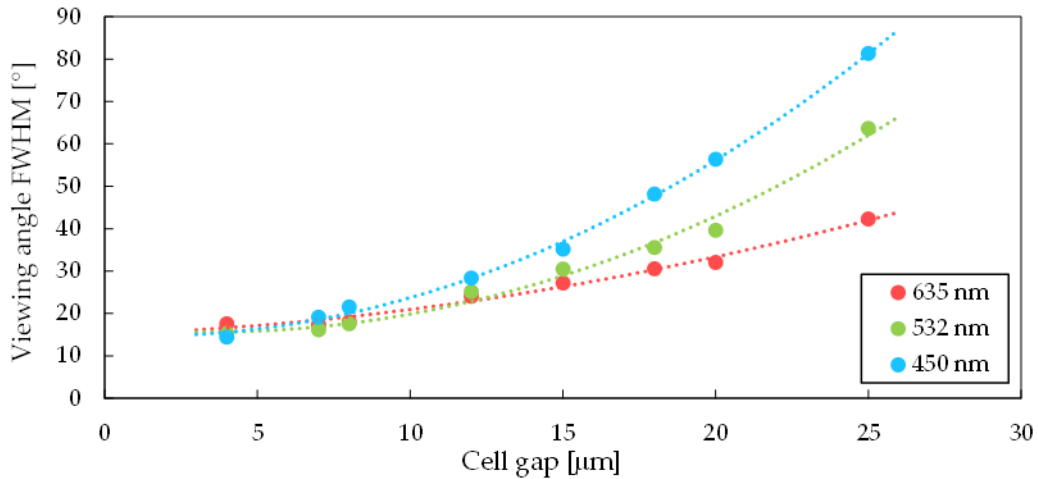
Figure 31.: LC layer thickness impact on viewing angle (FWHM).

Transition from **H** to **FC** in cholesteric LC is not a homogeneous process. It starts with nucleation centres at spacers or polymer material in PDLC [37]. If voltage is removed slowly, the number of formed centres is lower, they grow to larger size and consequently resulting light-scattering power is weaker than in the case when the voltage is removed instantaneously facilitating higher number of nucleation centres and finer domain structure. Similar behavior is also observed for PFLC. The analogy is similar to crystallization of melts and either slow or fast cooling - resulting in either large-grain structure or fine-grain structure.

For PFLCs if the electric field is decreased slowly, for example by discharging conserved electric energy through switched off driver unit or added resistor, the speed is slower and super scattering **FC** state is never observed, transmission is only reduced to 40%, see Figure 32.

(**a**)   (**b**)
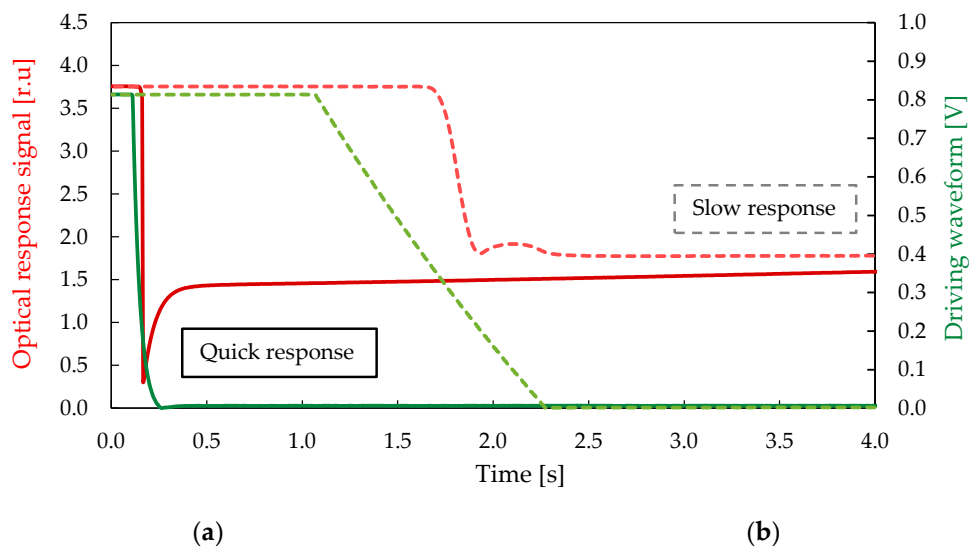
Figure 32.: Electro optical response of diffuser, discharged a) fast and b) slowly through resistor. Note that slow discharge decreases scattering state significantly.

The transient increase in transmittance (**M**) seen as a peak (see Figure 33.) for about 0.2ms after the initial drop in transmittance can be explained by possible formation of energetically favorable transient state similar to intermediate transient planar (**TP**)state observed for PDLCs [37] or a microdomain orientation mechanism (a similar peak characteristic of the transient state can be seen in the **FC**-to-**H** transition but the distinctness of the peak depends on the driving conditions).
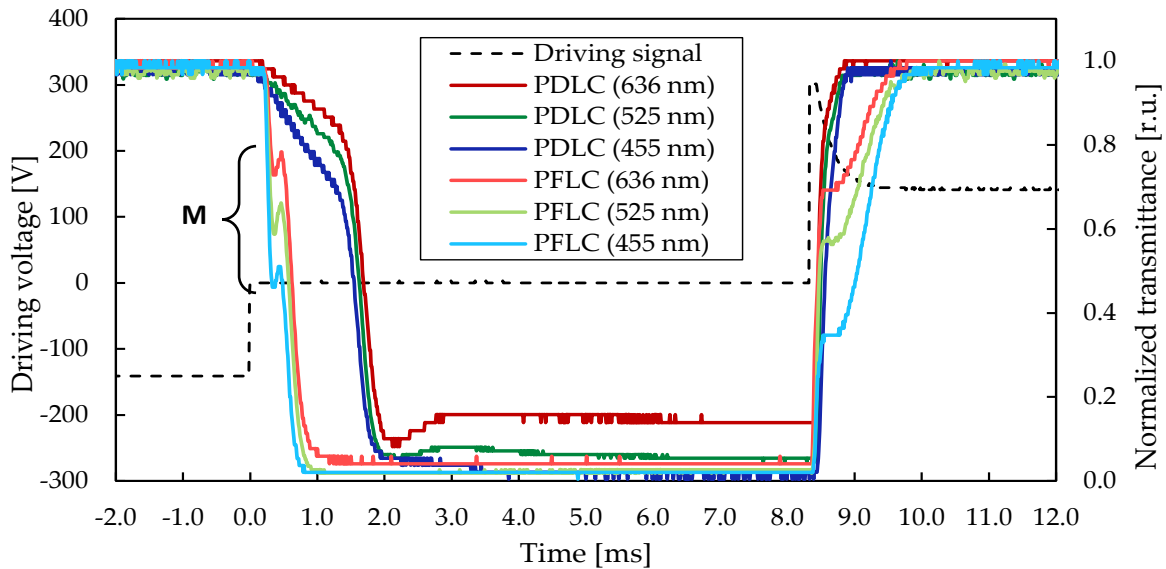
Figure 33.: Transient peak M position in PFLC switching dynamics.

The shortest switching time is observed when PFLC is discharged by short-circuiting but then the transient peak is observed. If the discharge is slower, leading to longer switching times, the transient peak intensity decreases as well, see Figure 34.
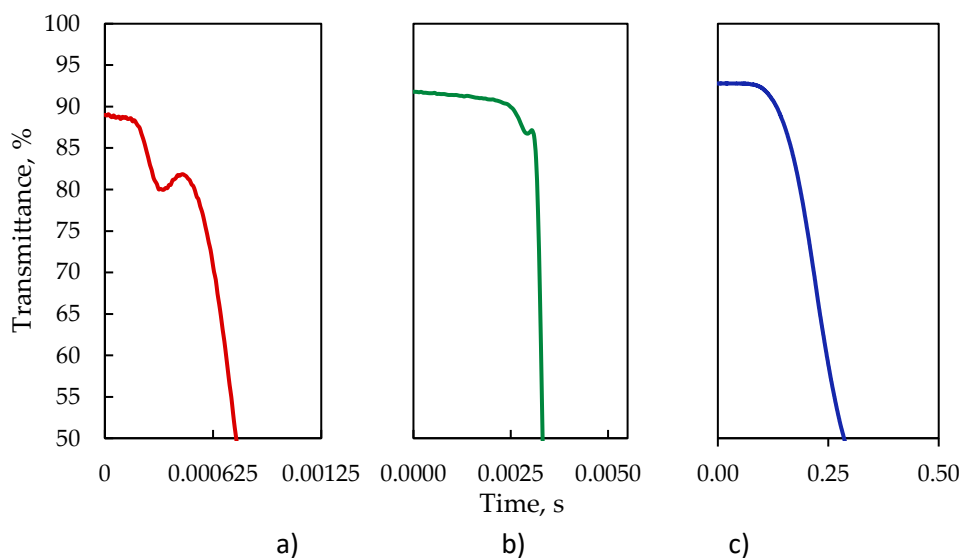
Figure 34.: Transient peak intensity change going from fast (a) to slow discharge (c). Note that fall switching time increases.

Potential cause of transient peak **M** could be reverse current caused by dielectric double boundary layer or motion of electric carriers-ions. LC resistivity measurements were performed using Keythley Model 6517B Electrometer and display cells (empty, filled with undoped LC, doped) in shielded box reveal that the ion contamination is very low, LC having resistivity of 10^{17} ohm*cm and it is not affected by dopant addition. Hence the reverse current mechanism is very unlikely. This can also be confirmed by measuring cell switching current by using 10 ohm shunt, see Figure 35. The only current surge can be detected when driving voltage is switched off.
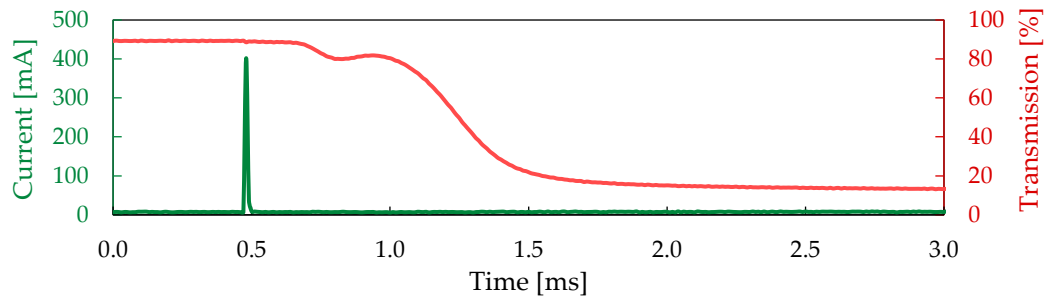
Figure 35.: Current through the cell.

Approximately 0.2 ms are lost during transient transmission peak, **M** state. Contrary to **TP** state for PDLC systems, no selective reflection is observed. Transmission and reflection spectra of 12 μm cell gap diffuser was measured with Ocean Optics Flame-T spectrometer using integrating sphere at several switching time positions A – before **M** state, B- at the maximum of **M** state, C – after the **M** state and D – at diffuse (**FC**) state, see Figure 36.

(**a**)   (**b**)
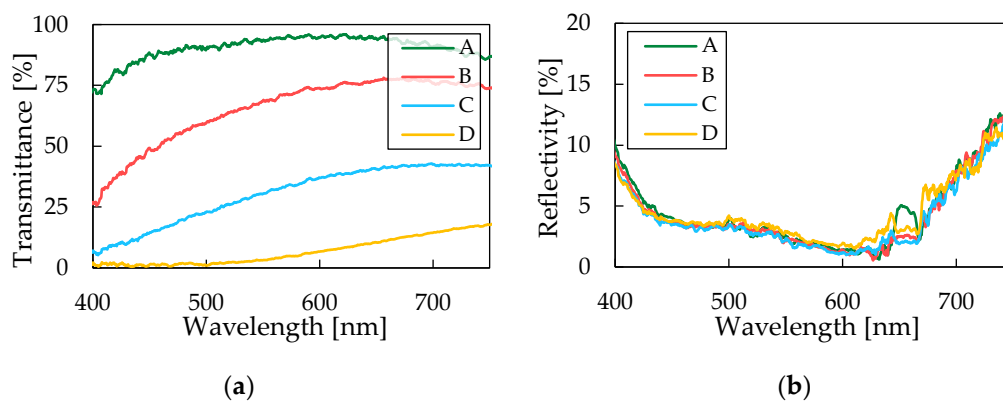
Figure 36.: Transmittance (a) and reflectance (b) changes during various time points for 12-micron diffuser cell during fall. Green – before transient peak, red – at transient peak, blue – after, and yellow – at FC state.

Contrary to **TP** state for PDLC systems, no selective reflection is observed for various time points. No change was detected if polarizing filters are used. Since short pitch systems will have cholesteric reflection band in region of 500-700 nm, we cannot use it to confirm supposed transient planar state. On the other hand, another type of transient state can be assumed. If planar orientation surfaces are used for device, some characteristic cholesteric reflection after some hours after driving

can be observed (slow relaxation), see Figure 37., region B. There are still some regions (region A) of different LC orientation, that reflects light at different wavelength, see Figure 38.
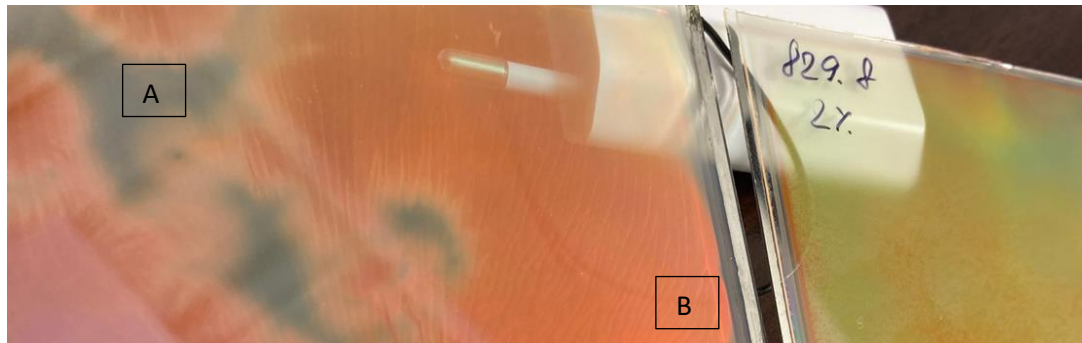
Figure 37.: Planar orientation surface cell color on the left and homeotropic cell color on the right. Region B has distinct cholesteric reflection.
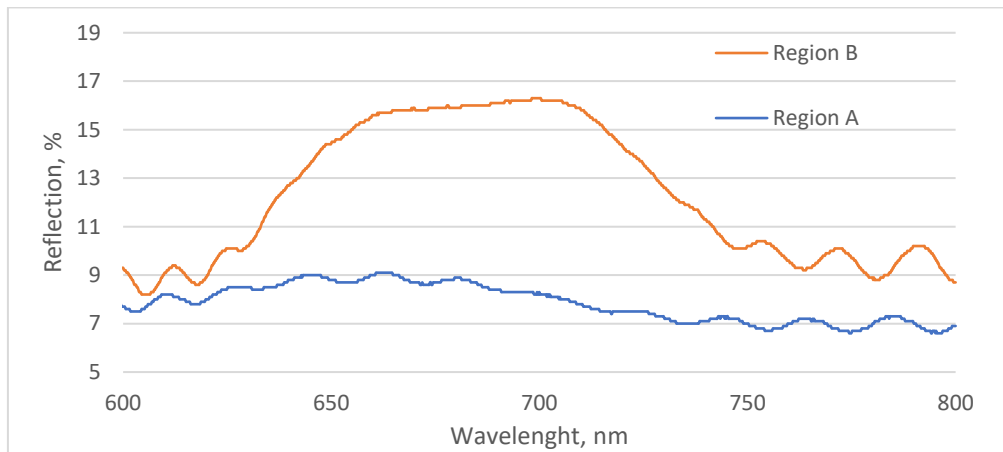
Figure 38.: Reflection spectra for several regions of planar surface alignment cell.

Increase of reflectivity in 640 -730 nm region confirms, that in the region B, planar orientation has formed due to LC slow relaxation. Transmittance spectra is seen in Figure 39.
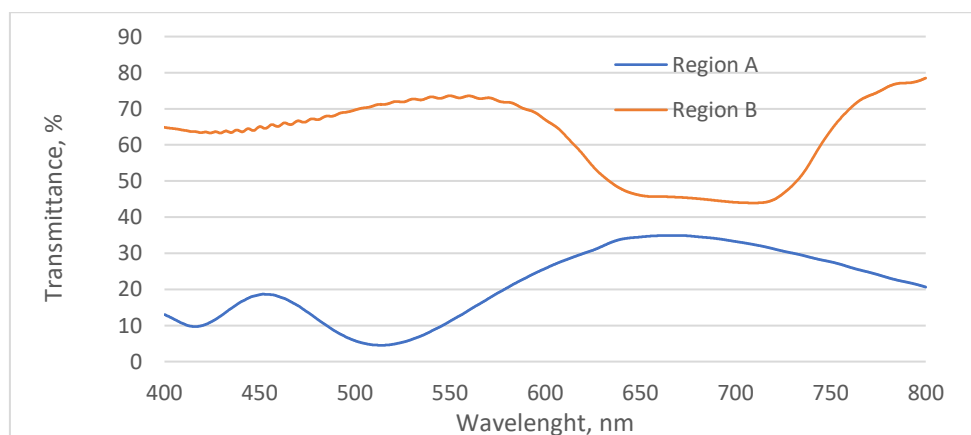
Figure 39.: Transmission spectra for planar surface aligned cell.

There is no evidence, that the transient state **M** is planar.

LC and surface interaction

The influence of the confining substrates surfaces on the relaxation process decreases with increasing the thickness of liquid crystal slab. By comparing different thickness of LC layer, we can see that while fall time remains practically constant, transient peak **M** appears later for thicker cell gap and narrows, see Figure 40.
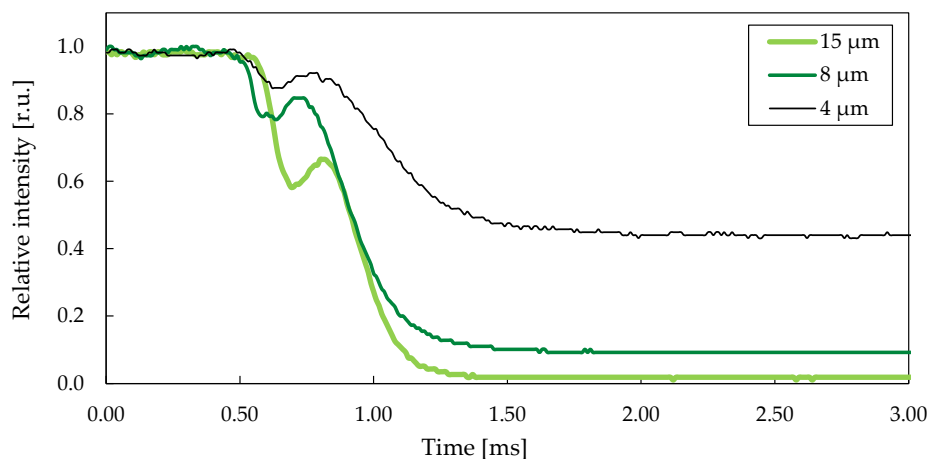
Figure 40.: Electro- optical curve character for various cell gaps. Measurements with 525 nm green laser.

The impact of a varying electric field intensity was evaluated by increasing the driving voltage in steps of 10 V. After the electric field reaches the switching threshold (60 V for the given samples), the nature of transient state **M** does not change, see Figure 41., so no dielectric boundary effect.
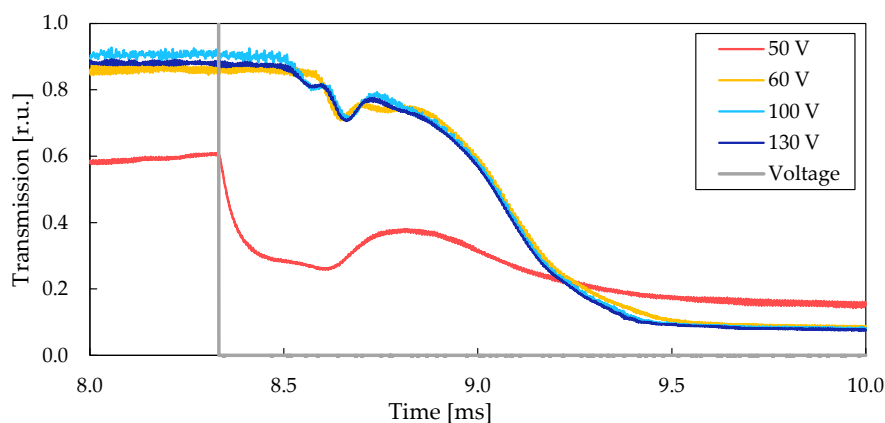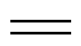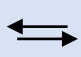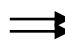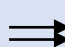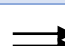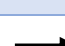
Figure 41.: Electro optical response of diffuser, depending on electric field. Once above switching threshold, nature of the curve does not change depending on voltage. Data for 535nm wavelength.

Another mechanism that can potentially cause transient state **M**, is reverse backflow of LC after electric field is removed. As known from the literature [39], at planar and homeotropic anchoring conditions there is a backflow effect after turning-off the applied electric field. This backflow is increasing the fall (relaxation) time. On the contrary, in cells with reverse pretilt anchoring conditions

(π-configuration) the fall time is shortened. In the same time, if strong surface anchoring of LC is used, like in planar orientation, this interaction will increase elastic energy stored in strained LC system. This might have negative effect on raise time.

Different types of surfaces for LC alignment have been prepared and evaluated, see Table 4. Intensity and timescale of transient peak was observed to be similar for all surface conditions for 7 µm 67x60 mm cells. However, from the surface role studies, we can conclude that if any notable reverse backflow is present, it was countered by reverse pretilt (antiparallel) surface condition, it is not the cause for transient peak **M** as no change of its intensity or position in time was detected.

Table 4.: Surface impact on 7µm diffuser E-O test results (525 nm wavelength).

	Alignment conditions	Pretilt angle	Orientation	Rubbing length, m	Open, %	Close, %	Fall, µs	Rise, µs	Fall speed, %/µs
⊥	homeotropic	-	none	-	83.4	11.9	898	1322	0.080
=	planar	low	none	-	87.6	6.7	1001	1535	0.081
⇆	planar	medium	antiparallel	1	88.5	6.4	1075	1807	0.076
⇒	planar	medium	parallel	1	87.8	6.7	1028	1517	0.079
⇒	planar	medium	parallel	2	87.4	6.7	1016	1549	0.079
⇒	planar	medium	parallel	4	86.1	6.6	1009	1489	0.079
⇒	planar	medium	parallel	10	83.2	6.4	995	1543	0.077
⇒	planar	medium	parallel	16	87.0	6.4	991	1578	0.081
⇒	planar	medium	parallel	28	83.7	6.5	996	1541	0.077
↑	Homeotropic	High	parallel	-	92.5	6.7	1046	1510	0.082

The fastest rise time is seen for homeotropic (PVD sputtered SiO_x) or high (80°) pretilt (SiO_2 by CVD) surfaces as in this configuration LC near the surface is already oriented to the homeotropic direction, which will be enforced after applied electric field. However, planar surface orientation provided better scattering properties than homeotropic orientation which is more important. When antiparallel planar surface alignment is used for PFLC (promoting p-cell configuration), it provides higher scattering property but the rise time is longer, when comparing to parallel condition. Varying

LC anchoring strength to surface by changing surface rubbing length (longer length corresponds to increased surface interaction) did not provide any noticeable effect on the diffuser performance.

As known from the literature, direct transition from **H** to Grandjean texture (the so-called planar state (**P**), with helix axis along the confining substrates normal) is not possible. Usually this transition pass through transient **FC** state. The cholesteric liquid crystal devices may exhibit three stable states with textures being Grandjean (**P**), Focal Conic (**FC**) and Uniform Lying Helix (**ULH**), respectively (see Figure 42.).
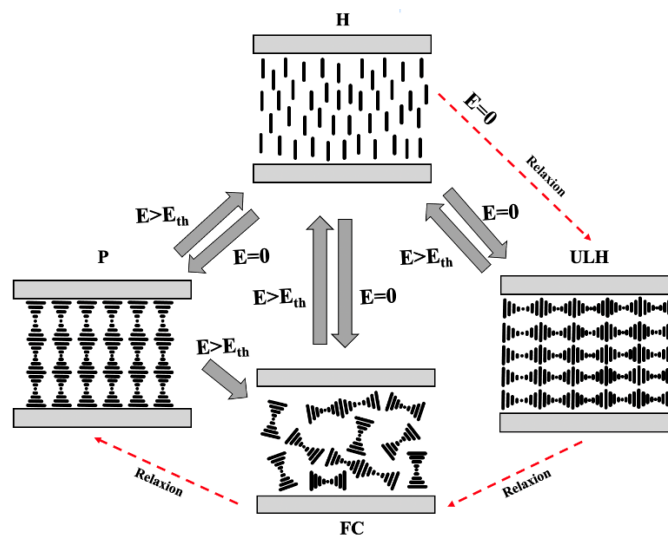
Figure 42.: Schematic presentation of the structural transition in cholesterics. Transition from H to P state may involve transient ULH state in the relaxation process.

The switching between these states is possible by applying an electric field with appropriate form and duration, and/or surface treatment. Moreover, such a switching may be performed by application of mechanical flow with or without application of an electric field, which can be ether unidirectional, inducing transition from **P** or **FC** texture to **ULH** texture, or mechanical pressure inducing transition from **P** or **ULH** texture to **FC** texture.

The optical appearance of **P**, **FC** and **ULH** differs substantially. **P** texture is reflecting selectively the incoming light with wavelength λ_0 which is directly related to the cholesteric pitch p by $\lambda_0 = \Delta np$ where Δn is the average refractive index [$n = (n_o+n_e)/2$], with n_o and n_e being the ordinary and extraordinary indices of refraction. **FC** texture is scattering the incoming light, whereas **ULH** texture is completely transparent.

Transitions between these textures with or without applied field is usually taking place through transient states (structures). In ref. [58], it was found appearance of transition peak M in the electro-optical curve after removal of the applied electric field during **H**-**P** transition, indicating an

increase of the light transmission. The peak was considered to be a result of appearance of transient Grandjean-like cholesteric structure during the relaxation process.

A similar peak in the light transmission curve of the liquid crystal diffuser studied in this work, was obtained after removal the electric field. This peak **M** in the optical response of the liquid crystal diffuser is worsening the light scattering characteristic of the diffuser. The investigations show, however, that the transient peak **M** doesn't exhibit selective reflection and therefore could not be assigned to appearance of a transient (**TP**) state. The increased light transmission, at the time of appearance of the peak **M**, suggests that formation of domains with uniform lying helix texture, which are optically transparent, takes place during the relaxation process. The material flow, which is a result of the structural changes in liquid crystal bulk, is considered as the origin of this transient state manifested by the peak **M** in the optical response of the diffuser. This flow may have parallel component with respect to the confining substrates in certain regions of the liquid crystal bulk. However, such a flow gives a preferred orientation of the growing as well as of the orientation of existing cholesteric domains, thus forming domains with transparent **ULH** structure. This process is transient and overgo with the time to **FC** state and then to **FC** state, respectively (see Figure 42., red arrows). Notice also that **H** texture may relax permanently to Grandjean texture through transient textures being either **FC** or **ULH**.

As already mentioned, the appearance of transient **ULH** state, indicated by the peak **M** in the optical response of the liquid crystal diffuser, is not desirable. One possible way to remove it is to apply electric field with form of continuous decrease of the applied voltage (ramp) to the diffuser rather than a sudden switch-off the voltage but must be precisely in time with **ULH** state.
By applying anchoring conditions in the experimental cells, promoting high reverse pretilt of the liquid crystal molecules at the confining substrates and thus realizing pi-cell configuration, which eliminates the back flow effect in the **H** state and hence is shortening of the fall time, was seen.

Another alternative way of shortening the response fall time is to accelerate the relaxation process by increasing the concentration of the nucleation seeds either in the liquid crystal bulk (*via* addition of nanoparticles or creating shallow appropriate polymer network) or by increasing their concentration on the substrates (creating appropriate surface topography).

Optimization of spectral response

Figure 43. shows the absorbance A of a LCD obtained from transmittance T measurements as $A = \lg(1/T)$. Collecting sphere was used. This value therefore also includes light lost through reflections from interfaces. However, the number of such interfaces is a constant for all samples, thus the change in absorbance for different cell-gaps is due to absorption of light within the LC.
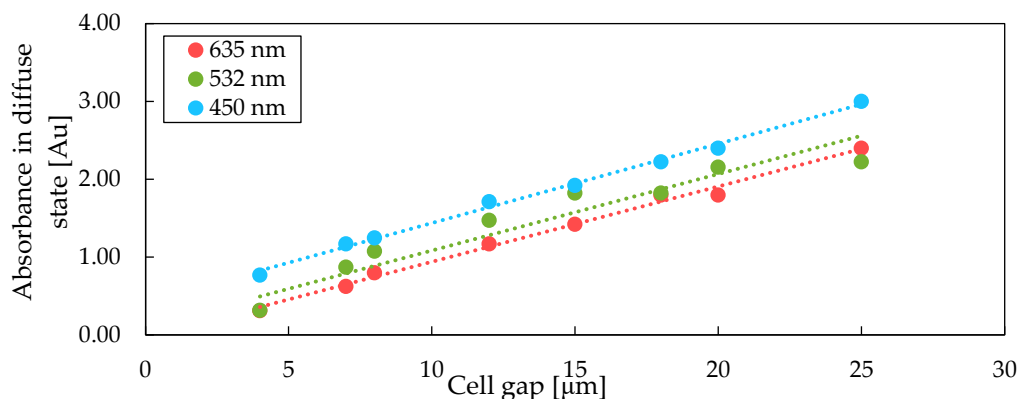
Figure 43.: Change in absorbance with cell gap size of a diffuser in the scattering state for different wavelengths. The scattering for 532 nm signal is due to the quality of laser-source.

It is easy to notice that the absorbance depends on the wavelength of light used. For accurate color representation, a diffuser element, in an ideal case, should absorb (as well as scatter) all wavelengths in the visible spectrum equally well. As can be seen from the transmission spectra in Figure 44., this is not the case – the diffuser-elements are more transparent to longer wavelengths of visible light in both the **H** and the **FC** states. This means that some color adjustments are required when rendering an image if accurate color representation is needed as the images otherwise appear reddish in color.
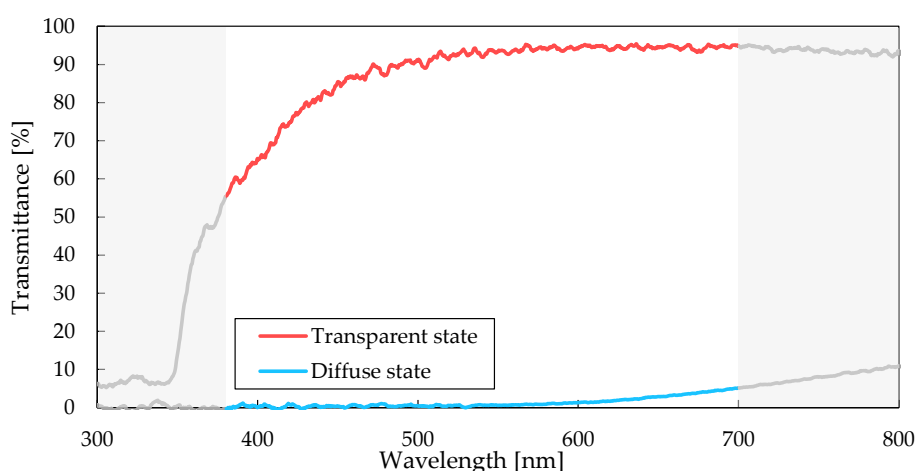
Figure 44.: Spectral transmittance in diffuse and transparent diffuser-element states.

Since in scattering state, when some part of the light is still transmitted, source of light can be seen and due to this effect, the "hotspot" has red color and is characterized as "red bleed-through".

We can try to even out its spectral characteristics with dyes, used in LC industry for specific modes. Dye molecules can be turned with LC molecules, so color intensity is dependent on LC molecule orientation. Blue color might provide good effect but we must keep in mind that dye doped LCD use guest -host mechanism that work with distinct LC orientations. Moreover, blue dyes are anthraquinone based, with very good photostability but lower S parameter (alignment with LC molecules) [59]. In our case switching happens from one determined (homeotropic) orientation to rather to randomly oriented orientation.

Six different dyes supplied by Mitsubishi Chemicals (see Table 5.) were mixed with standard LC, filled in cells and their E-O performance was evaluated with VST-2 testing setup.

Table 5.: Dyes and their concentration used in experiment.

Name	Composition
Yellow	LC3D2 + SI-486 0.001%
Red	LC3D2 + SI-426 0.001%
Blue I	LC3D2 + M-483 0.001%
Blue II	LC3D2 + SI-497 0.001%
Blue III	LC3D2 + M-412 0.001%
Blue IV	LC3D2 + M-137 0.001%
LC3D2	LC3D2 standard, no dyes

Blue dyes were not well aligned with LC molecules in homeotropic state as there is dispersion in open state transmittance results. This could be explained by molecular structure as blue dyes are anthraquinone derivatives. Lower transmittance was achieved for diffuse (close) state for both yellow and red dye doped cells, see Figure 45.

(a)   (b)
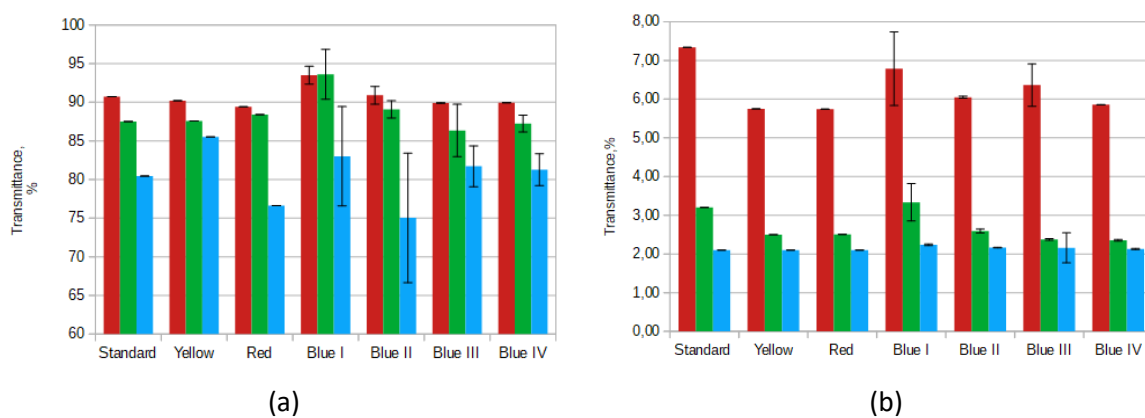
Figure 45.: Open (a) and close (b) state transmittance values for dye doped diffusers, VST-2 (RGB) E-O test system.

By comparing contrast ratio, we can see that yellow due provided better results, Figure 46.
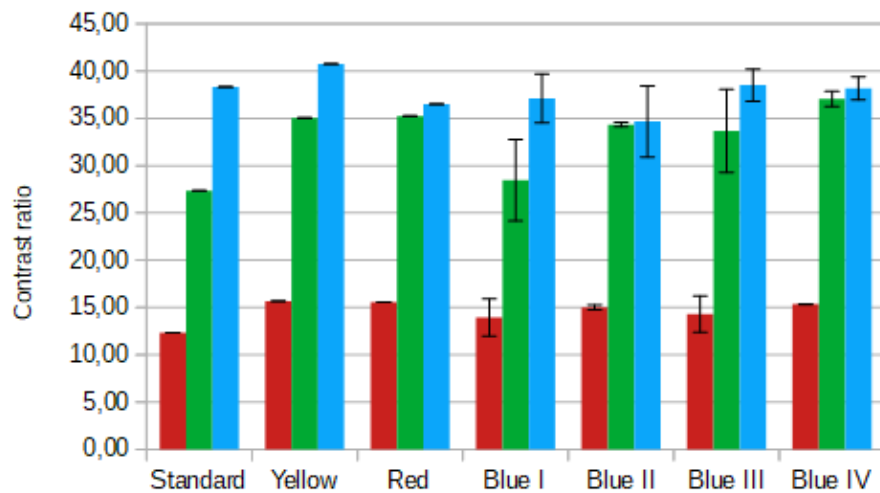
Figure 46.: Contrast for dye doped diffusers, VST-2 (RGB) E-O test system.

From spectral transmittance results, see Figure 47. we can see that none of added dyes have changed values at colour specific wavelengths but have increased scattering properties at larger wavelengths by increasing size of scattering domains. We can conclude that yellow due have improved contrast that can be used for diffusers.
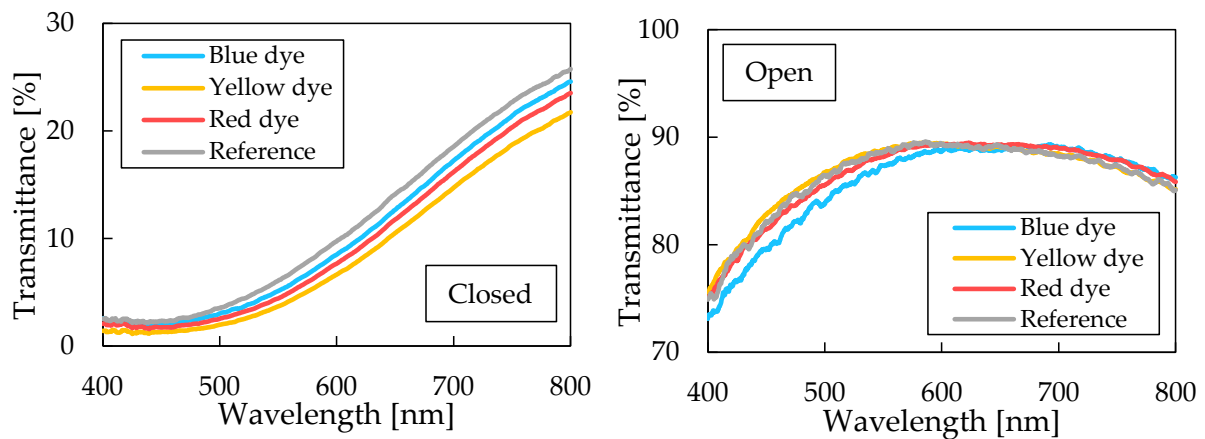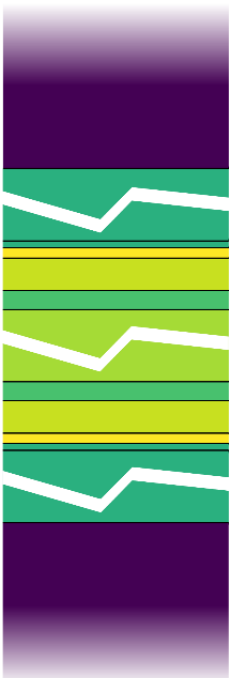
Figure 47.: Spectral transmittance in diffuse and transparent diffuser-element states with doped dyes.

LC thickness and refraction index determination

For further optimization of diffusers through modelling we need to know its refraction index and thickness. Larger form size diffuser was chosen as there is less influence from measurement system and parasitic capacitances of the circuit. Two types of functional LCD displays (61.8x48.8 mm) were prepared for the study by using 2.7 µm spacers and the same layer construction but filled with different LC:

- Most commonly used standard "E7" LC mixture, with well-known properties for reference purposes;
- Diffuser LC for measurement.

According to each LC type, polyimide layer had different LC alignment properties, planar for "E7" cell and homeotropic for diffuser. In order to evaluate liquid crystal layer thickness from measured capacitance data, diffuser and "E7" display capacitive structure simulation model was built using COMSOL Multiphysics software, see Figure 48. Model was used to analyze capacitance dependence from liquid crystal layer thickness, see Table 6.

Material	Thickness d, nm	Refractive Index n	Relative dielectric permittivity
Air	-	1.00	1.0
Glass	550000	1.52	7.75
SiO_2 barrier layer	20	1.52	2.18
ITO conductive layer	30	1.82	-
Silica based hard coat	95	1.75	14
PI alignment layer	55	1.58	3.6
LC layer	8000	1.71	9.6
PI alignment layer	55	1.58	3.6
Silica based hard coat	95	1.75	14
ITO conductive layer	30	1.82	-
SiO_2 barrier layer	20	1.52	2.18
Glass	550000	1.52	7.75
Air	-	1.00	1.0

Figure 48.: Capacitative and resistive structure of diffuser. Refractive index and permittivity data from supplier data sheets. On the left, glass and LC layer thickness is not shown on scale, indicated by zig-zag white lines.

Table 6.: Modelled diffuser capacitance values.

LC thickness, µm	Diffuser display capacitance, nF	"E7" display capacitance, nF
2.8	74.2	148.2
2.9	72.1	144.1
3.0	70.2	140.3
3.1	68.3	136.6
3.2	66.5	133.1

Both display types were measured for capacitance values with Agilent multimeter model 3606A and compared to modelled results, see Table 7. Measured values are lower than modelled results. Multimeter uses lower voltage (20V) well below switching threshold, when we are not completely aligning LC molecules and their orientation is unknown, so average relative permittivity is unknown. Note higher liquid crystal layer thickness value for sample P8-6, as it comes from different (assembled) LCD panel.

Table 7.: Capacitance values of displays filled with " E7" LC.

Sample ID	Calculated gap, µm	Capacitance modelled, nF	Capacitance, Agilent 3606A, nF	Capacitance, method "R", nF	Capacitance, method "C", nF
P8-6	3.3	148.2	85±1	129±1	131±0.6
P6-13-R	2.9	148.2	78±1	144±1	144.1±0.6
P6-24-R	2.8	148.2	74±1	152±1	152.8±0.6
P6-6-R	3.0	148.2	78±1	139±1	140.1±0.6
P6-11	2.8	148.2	72±1	147±1	145.5±0.6

There are two other methods of capacitance measurement that can be used, one with resistor in series (method "R"), see Figure 49., and second (method "C") with capacitor in series instead of resistor.
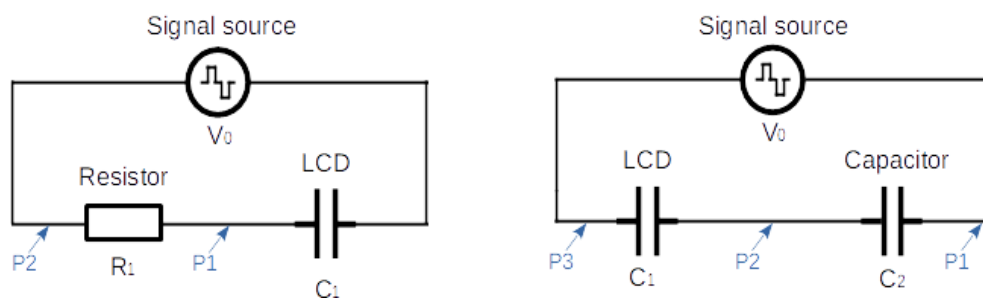
Figure 49.: Capacitance measurement methods. On left with resistor in series "R", on right with capacitor in series "C".

The test setup can be simplified to an RC circuit with a diffuser acting like a capacitor. The probes of an oscilloscope are connected to a resistor with a known and fixed value of approximately 10 000 ohms. Also, the oscilloscope is configured to capture a measured signal when its value crosses some specific voltage level. For this experiment the trigger value can be set up to +10 and -10 volts for detecting the charge and discharge voltage curves respectively.

From a standard RC circuit analysis, it is known that the voltage across the resistor will alter only during some rapid changes of the supply voltage or in our case, when the power supply is connected to and disconnected from the circuit. The voltage change on the resistor can be recorded and then converted to a current:

$$I(t) = \frac{V_m(t)}{R},$$

(5.)

which, by integrating it over the time, is transformed to the total charge that was accumulated on or released from the capacitor.

$$q = \int_{t_{start}}^{t_{finish}} I(t)dt,$$

(6.)

This charge is then transformed to a capacitance:

$$C = \frac{q}{V_s},$$

(7.)

where V_s is the supply voltage. The method with capacitor in series "C" is suggested [60] for faster switching systems, so it is preferred for this case. The method is also more convenient as capacitance value can be calculated directly from voltage measurements:

$$C_1 = C_2 \frac{qV_2}{V_1},$$

(8.)

where

C_1 – capacitance of the diffuser)

C_2 – capacitance of serial capacitor that is known, (300 nF for E7 cells)

V_1 – the voltage on capacitor C_1

V_2 – the voltage on capacitor C_2

Using method "C", measurements with capacitor with known value in series, we get similar capacitance results as with method "R".

"E7" filled displays were also measured by spectroscopic method. The required spectra in the 550-750 nm range were obtained using the Agilent Cary 7000 UMS spectrophotometer in 5 locations

of each cell and liquid crystal layer thickness was calculated using method developed by Institute of Solid State Physics.

Optical anisotropy of E7 LC is n_e=1.7472 and n_o=1.5217 according to supplier data. Extraordinary refractive index was used to calculate liquid crystal layer thickness, see Table 8. There is no difference observed when voltage is applied for most of the samples as expected since LC rotates only in XY plane.

Table 8.: Liquid crystal layer thickness of LCD samples with "E7" LC.

Driving conditions	Voltage on, 5V		Voltage off, 0V		Data from capacitance studies
Sample ID	LC layer thickness, µm	Stdev	LC layer thickness, µm	Stdev	LC layer thickness, µm
P8-6	3.0	0.2	3.0	0.2	3.3
P6-13-R	2.8	0.4	2.8	0.6	2.9
P6-24-R	2.9	0.2	2.9	0.2	2.8
P6-6-R	3.1	0.1	3.1	0.3	3.0
P6-11	3.1	0.2	3.1	0.2	2.8

To use spectroscopic method for further cell gap measurement of diffuser displays, refractive index must be known. To determine it, layer thickness of LC must be known first. If we take precautions that displays produced in the same conditions have the LC layer thickness, and fill some of them with liquid with known refractive index different from adjacent boundaries, so that interference peaks can be detected with ease and precision in transmission spectra. Obvious choice would be to use isotropic materials instead of LC, like ethylene glycol and cinnamaldehyde. However, these materials evaporate during filling process in vacuum chamber, so LC with known refraction index, "E7" typically used for comparable studies, was selected.

Displays were prepared in one batch, so one assumes, that all test displays have equal LC layer thickness but unknown absolute value, somewhat different from spacer size of 2.7 µm. To ensure equal layer thickness, during end sealing process when the excess of LC is squeezed out from cells under press, displays were mixed, see Figure 50.
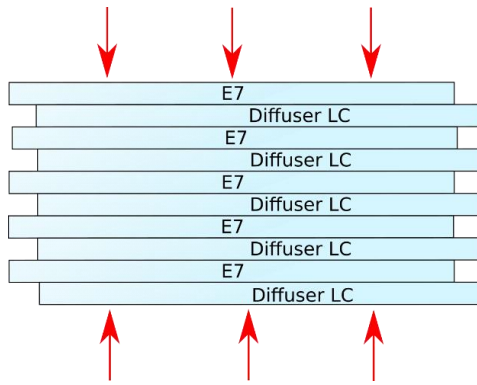
Figure 50.: Cell pressing during end seal press step.

Using LC layer thickness calculated for samples with E7 LC, refractive index of diffuser LC was calculated and average n calculated, see Table 9. See values plotted in Figure 51.

Table 9.: Refractive index of diffuser LC filled cells.

Wavelength, nm	P5-6-R	P5-20-R	P5-15-R	P5-16-R	P5-10	P5-19	Average, n
738	1.52	1.48	1.50	1.50	1.50	1.48	1.50
711	1.52	1.51	1.51	1.50	1.51	1.51	1.51
683	1.53	1.55	1.52	1.57	1.52	1.52	1.53
660	1.57	1.55	1.55	1.57	1.55	1.52	1.55
636	1.57	1.51	1.55	1.58	1.55	1.55	1.55
617	1.60	1.58	1.59	1.61	1.54	1.58	1.58
596	1.68	1.61	1.61	1.64	1.61	1.57	1.62
580	1.70	1.62	1.63	1.71	1.62	1.62	1.65
563	1.78	1.69	1.69	1.72	1.63	1.69	1.70
549	1.69	1.66	1.67	1.70	1.72	1.66	1.68
535	1.81	1.77	1.77	1.81	1.77	1.69	1.77

$$y = 6E\text{-}06x^2 - 0.0088x + 4.76$$
$$R^2 = 0.971$$
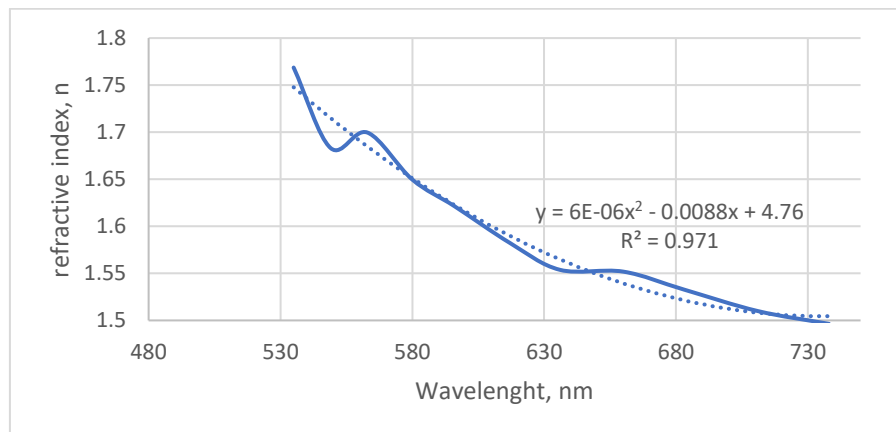
Figure 51.: Plotted n values of diffuser liquid crystal.

Refractive index measurement curve below 530 nm starts to have more interference, so 535 nm limit was used for curve estimation. The parabolic curve shape is in agreement with measurements for other LC mixtures in literature [43].

To explain measured lower capacitance values than expected from calculations, we need to look at general electro-optical response curves of the diffuser display, see Figure 52.
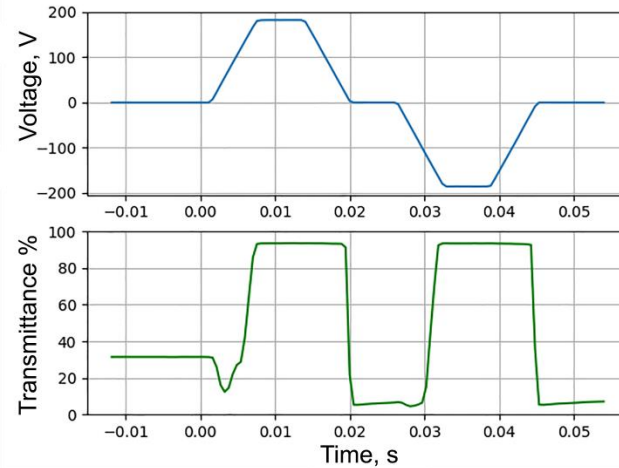
Figure 52.: Diffuser typical electro-optical response.

Before measurement, diffuser display has static transmittance value between 30-40 %, caused by relatively large light scattering domains that are orientated toward each other by weak intermolecular forces. Once low voltage is applied, transmittance drops to expected transient low value, as now previously large domains are broken down into smaller domains due to electric field which overcomes weak positional intermolecular forces. If the voltage is increased, LC molecules are aligning in the direction of applied field.

Capacitance measurements can be only used when LC has reached uniform homeotropic alignment under electric field, and is not changing when field strength is increased. In this case, if 90 V with known capacitor in series is used, see, the measured value corresponds to simulated capacitance values. The LC layer thickness, 3.0 μm is larger than spacers 2.7 μm, used for LC layer thickness control, so we conclude that cells have little excess of LC volume and glass is not completely resting on spacers. Spectrometric results correlate with model calculations, so model can be used for other LC layer thickness and size diffusers.
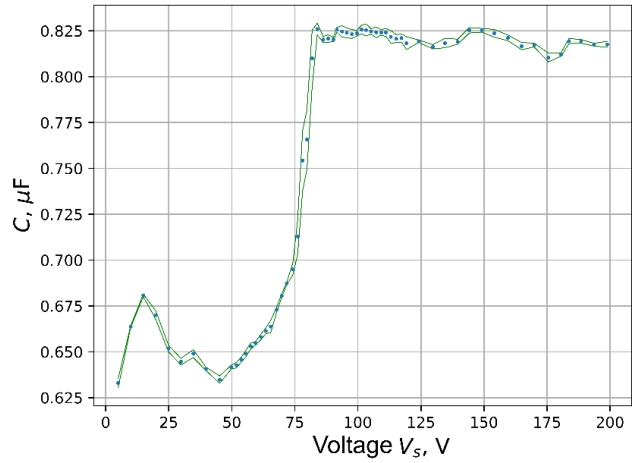
Figure 53.: Capacity measurements depending on measurement voltage with method "R".

Four other diffusers of intended cell gap of 12 μm (size 387.3x294.3 mm) were selected for practical demonstration. All of them have quite identical current profiles during the charging and discharging processes. For example, for method with resistor, a graph of a resistor current starts as an approximately linear function and then transforms to an exponential decay curve for the second half of the charging process, see Figure 54.
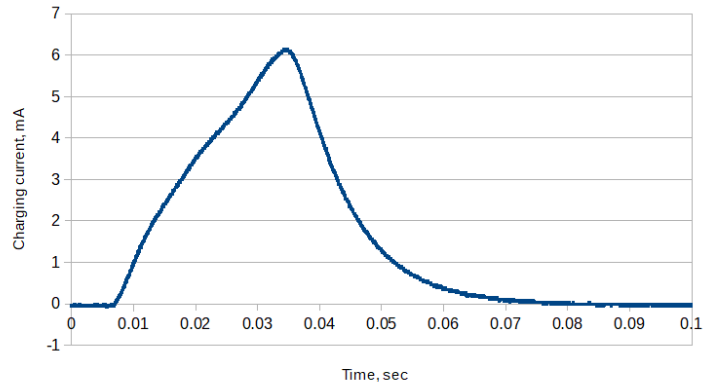
Figure 54.: Charging current of 387.3x294.3mm 12μm diffuser with method "R".

This graph can be transformed to a function of a total charge that accumulates on a diffuser:
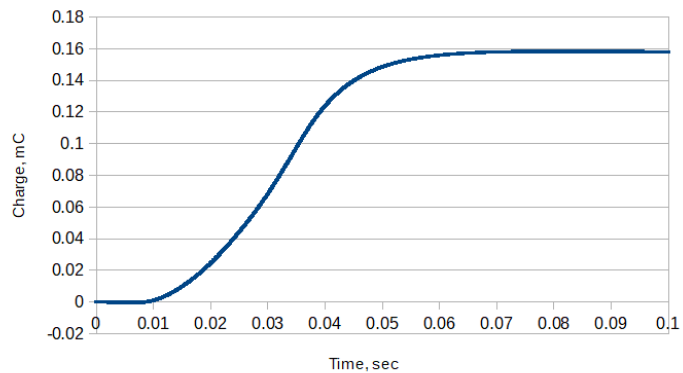
Figure 55.: Total charge stored on 387.3x294.3mm 12μm diffuser during charging with method "R".

From the Figure 54. and Figure 55., it is clear that 387.3x294.3 mm 12 µm diffuser stores around 16 mC of charge, hence by using Equation 7., it is possible to conclude that its capacitance is equal to 0.8 µF. Approximately the same results were calculated for all of the diffusers in the same series, 4 in total. The consistency of the results indicates that that this capacitance value can be considered as correct for this particular diffuser series and specific voltage supply level. With method C, we get the same capacitance values, as with R method. Using COMSOL Multiphysics model, we find that the actual LC layer thickness is 11.6 µm, see Table 10.

Table 10.: Diffuser capacitance measurements with various methods.

Display active area, mm	Calculated LC layer thickness, µm	Capacitance, Agilent 3606A, nF	Capacitance modelled, nF	Capacitance, method C, nF	Capacitance, method R, nF
61.8x48.8	3.0	50.8±2.9	70.2	69.7.±0.6	67±1
387.3x294.3	11.6	400	779.5	780±0.6	779±1

Developed method for cell gap determination can be efficiently used in device manufacturing. During production process, it is important to measure LC layer thickness immediately after glass assembly into panel process, preferably by inline process control system. Coincidentally, standard display glass has notched corner for conductive side and flow direction identification purpose. After assembly both notched corners provide access to opposite display glass conductive layer, so capacitance value can be measured without completing further processing steps, like gasket curing, cutting and soldering of contact pads, see Figure 56.

(a)   (b)
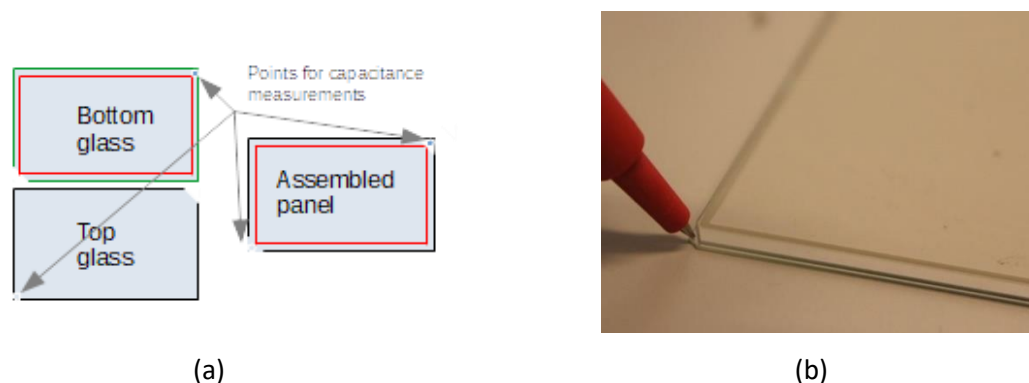
Figure 56.: a) Assembled panel capacitance measurement points b) close up picture of panel corner during measurement.

3.4 Conclusions

Higher concentrations of the dopant shortens cholesteric pitch and also decrease switching time from H to FC state. There is maximum workable concentration after which switching time increases again and later scattering start to decrease, due to oversaturation by the dopant. For one of the highest HTP dopants, this concentration is 2.5%.

Transient increase of transmittance during change from H to FC, is not caused by transient planar state, characteristic to PDLC, but by formation of uniform lying helix state. Its intensity can be changed by electric field removal conditions.

Scattering properties can be increased if planar surfaces are used. Among them, antiparallel surface orientation is preferred as it decrease LC backflow.

Contrast for longer wavelengths can be improved by addition of yellow dye.

Scattering type liquid crystal layer thickness control method based on capacitance measurements was developed and validated. Various capacitance measurement methods have been evaluated and method with capacitor in series have been found most convenient. COMSOL Multiphysics program have been used to compute capacitance models.

Capacitance method has been compared by using spectroscopic measurement method using interference spectrum peak detection for LC with known refractive index and found that both provides similar results.

In the same time, diffuser LC was filled in identical LC layer thickness cells and previously obtained value of layer thickness was used to determine refractive index of novel liquid crystal mixture for diffuser (light scattering) LC. Knowledge of refractive index allows further optimization of LCD cells in future by index matching.

Proposed LC layer thickness control method has been approbed for use in inline LCD production.

4. Diffuser solid state material interaction with electromagnetic waves

4.1 Literature review

Antireflective layer film stack on outer surface of the diffuser

The first boundary light (electromagnetic waves) from image projection system meets is air/glass. Whenever boundary of different refraction index materials is used, reflections according to Snell law appear. Common approach to reduce reflections is by designing antireflective layer stack. There are known methods for calculating antireflective layers, starting from matrix transfer method to Fresnel equation [61]. Several free online calculators and commercial software tools exist, for example Optilayer, CODE V, Film Wizard. They differ in performance and algorithms used and are intended for more complex tasks beyond simple AR layer design, and are expensive. The only way to choose between this variety of tools is to perform validation – simulate stack with software, coat this stack and compare practical results with simulation. Alternatively, for easier cases, like AR layer on diffuser surface, this modelling can be done by calculation of single layer equivalent reflection coefficient r_{eq}:

$$r_{eq} = \frac{r_{12} + r_{23}e^{-2i\delta}}{1 + r_{12}r_{23}e^{-2i\delta}}$$

(9.)

where r_{12} is reflection coefficient between first layer (air) and AR layer, r_{23} is reflection coefficient between AR layer and next layer (for example, glass) and δ is the phase delay that is introduced by crossing the single layer:

$$\delta = \frac{2\pi n_2 d cos\theta_2}{\lambda_0}$$

(10.)

where θ_2 is the acute angle that the ray makes with the surface normal as it propagates through the layer, n_2 – this layer index of refraction, d thickness of the layer and λ_0 – vacuum wavelength. If multiple layers are used in stack, it is possible to use Equation 9. recursively to compute the transmittance and reflectance of the entire structure. Commercially available software COMSOL Multiphysics have Geometric Optics module with built-in Maxwell and Fresnel equations and can be used for this task using finite element method.

Transparent conductive layer

Diffuser manipulates electromagnetic waves in visible range by arranging LC molecules with applied electric field by transparent thin conductive film on both sides of LC layer so that they are passed through or scattered. Contrary to the traditional LCDs where active area is made of many small pixels, diffuser has one large pixel that must be uniformity charged at high electrical field intensity so high conductivity could be preferred. However, higher conductivity typically means thicker layer which is less transparent. In the same time diffuser must be highly transparent for visible range electromagnetic waves, so thin layer could be preferred, so a compromise must be found.

Indium tin oxide (ITO) is most common material for display applications despite some alternatives [62]. One of probable alternative is thin (~10 nm, ~20 atom layer deep) silver layer. However, there are practical limitations. If higher than 5 ohm/sq. resistivity is sought, it becomes very difficult to control such layer deposition as it does not adhere well and thickness control becomes very difficult. By using silver nanowires this resistivity value can be achieved and even exploitable transmission can be extended to far IR region where ITO cannot be used. Silver nanowire network in turn increases haze and if higher current is used, nanowires can weld together [63] making it suitable only for special applications. Contrary to silver, ITO layer adheres quite well to glass by making Si-O-Me bonds, is sufficiently hard for any further processing and have very low extinction coefficient (0.004 at 500 nm) [62]. As it must be deposited in thicker layer, control for optimum properties is much improved. It must be noted that thicker than 250nm layers are not used as transmission decreases even with near zero absorption coefficient in visible range.

ITO properties can be changed to some extent. Typically, ITO is sputtered on glass by physical vapor deposition (PVD) technique at substrate temperatures above 300° C with slight oxygen deficit. Coatings at these temperatures have best conductivity due to crystalline lattice structure and oxygen vacancies in addition to built-in tin ions. It is possible to deposit ITO at lower temperatures and later use thermal treatment at 300° C at reductive atmosphere but conductivity will be lower at least by factor of 2 [64]. This, however, is common solution for sample production or sputtering on temperature sensitive substrates, like polyethylene terephthalate (PET) films. If higher temperatures and oxidative conditions are used, for example for next process steps, conductivity will decrease due to incorporating oxygen into structures [65].

SiO_2 barrier layer is used on soda lime glass as Na^+ ions, due to their small size and increased mobility even at temperatures beginning of 100° C, diffuses into ITO layer and act as acceptors thereby decreasing conductivity. Heavy Na^+ pollution may also lead to NaCl formation on surface and increase of haze. Borosilicate glass usage is thus preferred.

Most of the transmission loss occurs due to reflection at ITO surface, it having refractive index of 1.82. When thick (over 100nm) layer is deposited on glass with refractive index of 1.52, interference gives visible coloration – iridescence. This can be decreased by using Na^+ barrier layer that must satisfy λ/4=n*d condition. For example, carbidic silicon oxide $SiO_x(CH_y)_z$ with 1.74 with 70 nm of thickness is used on SnO_2 coatings [64] to reduce reflections.

Deposition of ITO layer as combination of two ITO layers, each with slightly different refraction index by varying oxygen content decrease reflectivity from 8.8 % to 5.7 % [64].

Use of low resistivity ITO leads to increased likeability of dielectric breakdown. There is patented [66] solution to limit dielectric breakdown frequently used in diffusers. For example, large electrode area (300x400 mm) is structured by dividing lines, so that each electrode is divided into 60 narrow (5 mm) parallel strips. For any arbitrary point, resistance is 6272 ohms but overall resistivity of the system remains low, 6272/60 = 105 ohm. The approach has its drawbacks, as it raises concerns how much high voltage is delayed when narrow strip is charged from busbar side. For very fast LC switching speeds, 4 side or two side driving is used to keep RC constant low [67], [68].

Imagine each mm^2 of diffuser as small capacitor, which is charged and discharged depending on nearby elements. Elmoore delay model, applied in LCD industry for pixel line overdrive calculations [69], can be used to calculate voltage at the end of electrode strip, consisting of M resistors and capacitors. Each capacitor is independent of others and it does not change capacity depending on voltage.

$$RC = \sum_{i=1}^{M}\left(C\sum_{j=1}^{i} Rj\right)$$ (11.)

Where C is capacity and R resistivity of individual element. Alternatively, it should be possible to model by finite element method in Comsol Multiphysics, taking into account LCD capacity change with applied voltage.

It is possible to use conductive layer in direct contact with LC but there are two problems – it is very difficult to control LC alignment on ITO surface and, when high field intensity is used, dielectric breakdown is common. Therefore, dielectric layer is necessary and on top of it, polyimide is traditionally used to control LC alignment in displays.

Dielectric and orientational layer

Dielectric insulator layer on top of transparent conductive must provide following functions [17]:

- Align LC molecules in certain direction;
- Even out electric field across transparent conductive electrode area;
- Be as thin as possible so the main voltage drop happens across LC layer;
- Prevent the capacitor structure from shorting;
- Its refractive index should be matched to adjacent layers to minimize internal reflections.

Traditional LCD organic alignment materials [70] generally provides good correspondence to first three points, while fast switching requires high voltage which is not typically addressed in common LCD modes but increases importance of fourth point. Moreover, for micro displays, inorganic materials are preferred, as there is high-power arc lamp illumination. Short wave blue light lead to differential aging in multiple-micro display projectors, distorting colors [33].

Current approach to readily available range of commercial compounds would be utilization of magnetron-sputtered thin films. In previous work it has been shown, that traditional LCD materials as SiO_2 and polyimides can be replaced by SiO_x thin films deposited by magnetron sputtering [54]. Magnetron-sputtered SiO_x thin films exhibit high transmittance and high resistance to dielectric breakdown.

Moreover, it is possible to adjust the refractive index of magnetron-sputtered films by varying deposition parameters. For example, SiO_xN_y is very suitable dielectric material for optical diffuser applications, since it's refractive index can be varied from 1.5 to 2.0 [71].

4.2 Material specification and initial modelling

Table 2. specified diffuser properties in chapter 2. We will focus at specific some of these properties in this chapter, see Table 11.

Table 11.: Specified diffuser properties for the work, extract for chapter 4.

Specification	Current	Goal	Chapter
Number of layers	47	39	4, 6
Total set transmission in open state	78 %	82 %	4, 5, 6
Individual unit transmision in open state	89.3 %	90.5 %	4

The primarily aim of the work is to increase transmittance of the diffuser stack. To achieve this, we need to take care of air-glass reflections for outer diffusers. From the experience with larger size diffusers, commercial broad band antireflective (BBAR) coating can decrease ~7 % of reflections from the air-glass boundaries for single diffuser, so we can expect similar gain. In addition, we can try to optimize BBAR coating even further by using own PVD coater.

Commercially available BBAR layer stack for air/glass interface is 10 nm Nb_2O_5, 40 nm SiOx, 110 nm Nb_2O_5, 80 nm SiOx, which is coated on ITO glass on nonconductive side. It is rather expensive and with long lead time. Besides it is optimized for general use at broad wavelength range but in our system reflection at projector RGB wavelengths are important. So, with in-house PVD, it should be possible to make AR coating even with better properties tailored to projection systems. COMSOL Multiphysics software was used to model reflection from glass surface by using Thin dielectric layer feature and auxiliary parametric sweep for optimization mode was used, and alternatively Optilayer. This yielded two possible stacks for experimental trials - CS_2_550 (COMSOL: 10nm Nb_2O_5, 40nm SiOx, 120nm Nb_2O_5, 90 nm SiO_x) with less reflection in lower wavelength region and CS_3_550 (Optilayer: with flatter curve and lower normalized reflection (0.7% vs 1.2%), see Figure 57 (next page) and Table 14 (in experimental section).

Commercial stack was also modelled under CS_1_550. For COMSOL model, glass n-k data dispersion was used and for coatings - n values at 550 nm wavelength.
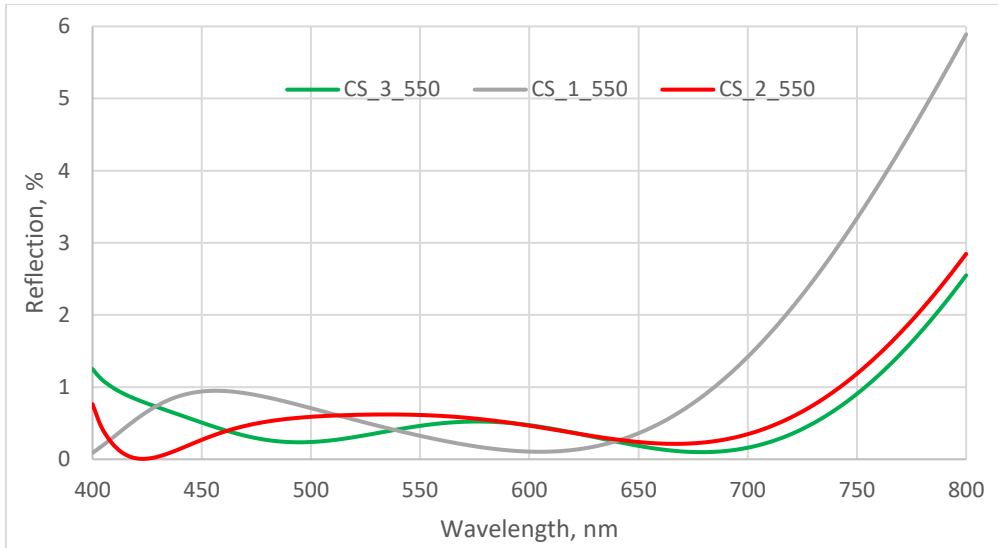
Figure 57.: COMSOL modelled reflection curves CS_1_550 (commercial), CS_2_550 and CS_3_550.

Next, we will need to increase transmittance of each individual diffuser. As a rule of thumb, each 0.1 % improvement for single diffuser transmittance will lead to 0.3 % transmittance gain for the laminated stack, so to get 1 % improvement we need to increase transmittance of single diffuser by 0.4 %.

This can be done by matching refractive index of internal layers (stack). Reduction of layer number is secondary aim, as fewer number will lead to more efficient production. One of the layers with nonzero extinction coefficient is ITO (0.008 at 430 nm, 0.004 at 500 nm), where the primary thickness requirement is based on conductivity requirements. If conductive properties can be improved, thinner coating can be used and this will improve transmittance in turn.

Current layer stack of diffuser, is shown in Figure 58. We can see that there are quite big differences between glass, ITO and LC refractive indexes. Normalized transmittance simulation by freely available filmmetrics.com tool gives 89.4 % value, which is in agreement of experimental measurement results.

Component	n	d, nm	n*d, nm
Air	1		
Glass	1.52	550000	836000
SiO₂ barrier layer	1.52	20	30
ITO conductive layer	1.82	30	55
Silica based hard coat	1.75	95	166
PI alignment layer	1.58	55	87
LC layer	1.71	8000	13600
PI alignment layer	1.58	55	87
Silica based hard coat	1.75	95	166
ITO conductive layer	1.82	30	55
SiO₂ barrier layer	1.52	20	30
Glass	1.52	550000	836000
Air	1		

Figure 58.: Initial single diffuser layer stack composition, showing refractive index, physical and optical thickness.

Conductive layer

For conductive layer we have two options – A) to use commercially available ITO coating with defined conductivity (ITO high temperature process, thin SiO_2 Na^+ barrier layer) and B) to deposit ITO with own equipment in low temperature process where we have more freedom to optimize coating properties for product application. SiO_2 layer under ITO in commercially available glass work only as seed layer and Na^+ barrier layer and does not serve as index matching layer between glass and ITO. In order to evaluate necessity for index matching layer between ITO and glass to improve transmittance, first quick analysis using freeware online thin film metrics calculator, filmmetrics.com, was done. While it is precise for few thin film layer stacks, it does not have capability to use custom materials with refractive index dispersion data. Using quartz/AR layer/ITO/air model, we find that index matching layer will improve transmission, see Table 12. This will be one of goals for experimental work as potential gain here is significant.

Table 12.: Glass substrate transmittance simulation results when BBAR layer is deposited under ITO layer.

Layer under ITO	Normalized transmittance	Note
none	79.63 %	Baseline
75 nm n=1.75 under ITO	80.64 %	Suggested by literature
30 nm n=1.51 under ITO	80.36 %	Available

Since ITO thickness is directly linked to overall display transmittance, use of thinner coating with the same conductivity will lead to improved diffuser transmittance. This is second goal for experiments. ITO coatings with conductivity of 80-100 ohm per square (~30nm thick) are typically used as they have at least 86% of transmittance. Further decrease of thickness does not result in improvement of transmittance but increase of resistivity and hence thicker coatings reduce transmittance significantly according to all supplier data. Moreover, the deposition will be done in lower temperature so its conductivity will be lower.

Contact placement to ITO must be considered as fast switching speed is also desirable. Electrode area is not square and one can suppose that electrode charged from contact edges along the long side will charge faster than one with contact edges on short. Moreover, large size diffuser electrode is separated in small strips to prevent dielectric breakdown. Before modelling small size diffuser, appropriate model could be designed based on existing results of experimental investigations of large size diffusers, especially due to fact that contact placement impact on switching speed should be more pronounced.

Behavior of large diffuser electrode strip can be modelled by COMSOL Multiphysics software, using finite elements method. Fringe fields are ignored as they are small, all layers were modelled with known material properties. In the model one (bottom) electrode have equal 0 potential over the surface but upper electrode is connected to driving signal at the end of strip. As electrode are is 400mmx300mm, the 100 mm difference in strip length will result depending of connection configuration. After initial signal application, voltage over top electrode strip is not uniform, near the electrode connection potential is higher, see *Figure 59*. This is enough to create voltage difference over LC layer immediately after high voltage is applied, so that LC at the area near to electrode connection reaches switching threshold faster than at far end of the strip.
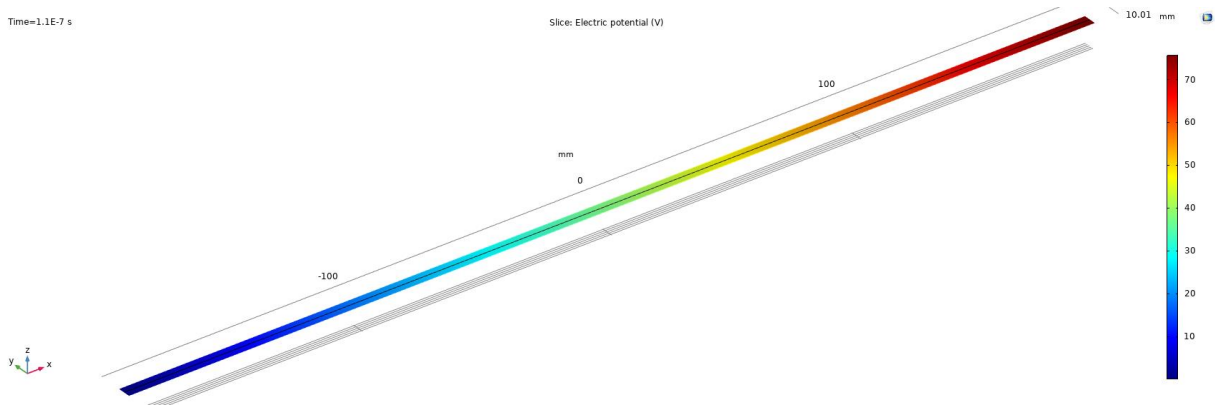
Figure 59.: Electric potential on top ITO layer 0.11µs after 150 V is applied. Left side is connected to busbar and almost zero is observed at the end of 400mm strip.

If we compare both versions for 150 V driving condition, we can see that version with contacts on 400mm long edge is faster, see *Figure 60*.
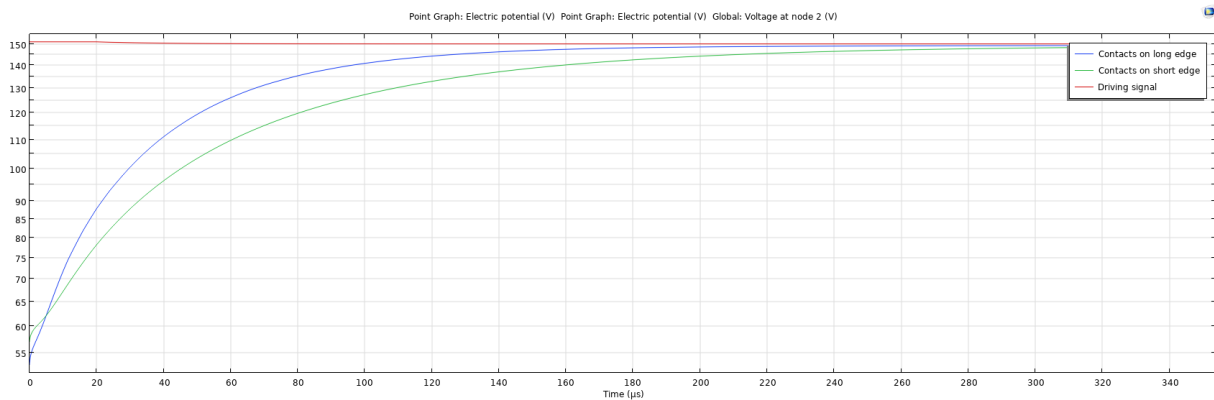
Figure 60.: Potential difference over LC layer for different contact versions, blue – contacts on 400mm edge, green – contacts on 300mm.

However, this value is small, 30…40 µs, depending on threshold voltage. Theoretically, raising the overdrive voltage should eliminate the differences. However, this will require to raise overdrive voltage from 90 V to 310 V on top of driving voltage of 150 V.

Alternatively, we can use Elmoore model [69]. For 300x400mm diffuser with contacts on long side (electrode is divided in 58 shorter strips), RC constant is 2.04553E-05, and 20µs after 150 V is applied, then at the end of strip we get 93.57 V. For diffuser version with contacts on short side (electrode is divided in 78 longer strips) RC constant is 3.6834E-05, and we will get the same voltage value after 36µs. The difference calculated is small, only 16 µs.

To test modelled results for contact placement (400 mm vs 300mm electrode strip length) on electrode two series of 400x300mm diffusers were tested with VST-1 at 150 V. The observed 64 µs difference between versions is slightly larger than modelled 30-40 µs, see Table 13. This probably can

be explained by deviations of cell gap (as precise values are not measured) or repeatability of measurements (~20 μs).

Unit	Electrode length	Transmittance, open state	Transmittance, close state	Fall, μs	Raise, μs
USAM1	300mm	96.9 %	3.4 %	647	1230
USAL1	400mm	96.9 %	3.3 %	687	1293

For smaller form factor diffusers, like 170x95 mm, the whole electrode area is one pixel without division into strips. Several contact configurations exist, see *Figure 61*. At first glance, L-type driving should be more advantageous as allows to charge electrode from two sides at once.

(1) short   (2) long   (3) L-type
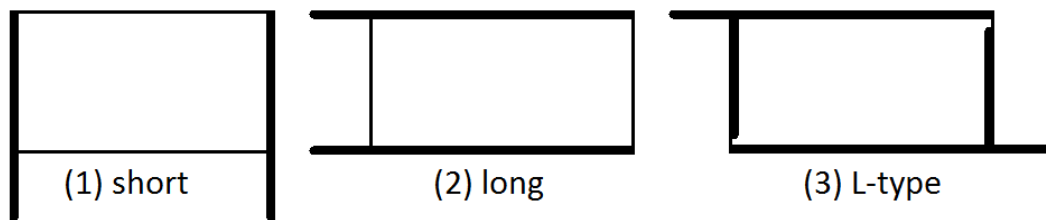
Figure 61.: Contact configurations for single pixel diffuser.

COMSOL model show that there is very small advantage for L-type contacts over short side, as the area is in fact double square, not like long strip in 300x400 diffusers. Visualization in *Figure 62*., show that in the middle of display, electric potential in the beginning of driving is not equal.

a)   b)
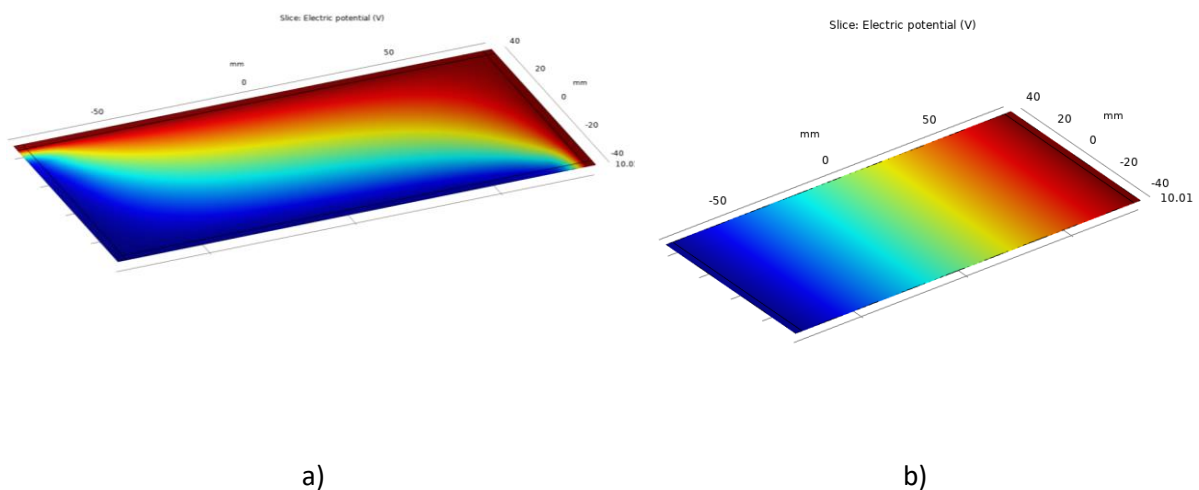
Figure 62.: Visualization of electric potential in V, 0.01μs after signal, a) L-type, b) side.

Modelling of electric potential in upper ITO layer at the middle of the diffuser shows that all contact versions reach 100V almost in the same time and L-type, is marginally faster, see *Figure 63*.
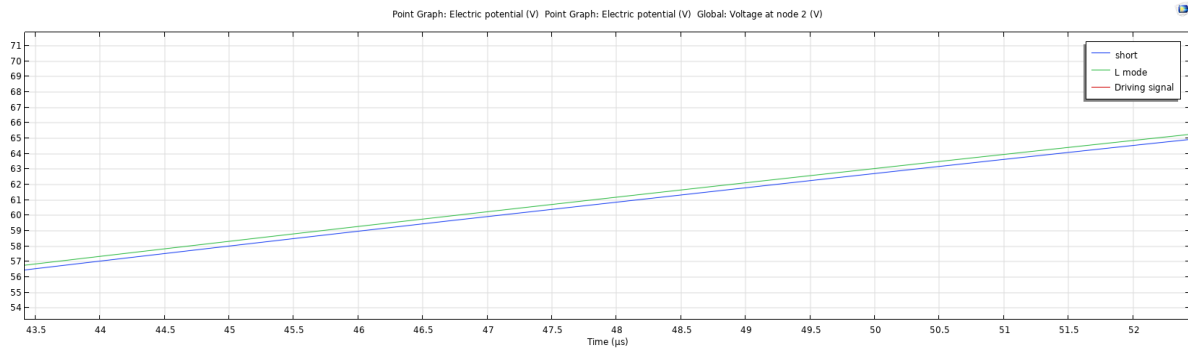
Figure 63.: Comparison between short and L-type, zoom in.

Far larger difference can be observed for different cell gaps, see *Figure 64*. Thinner cell gaps switch faster.
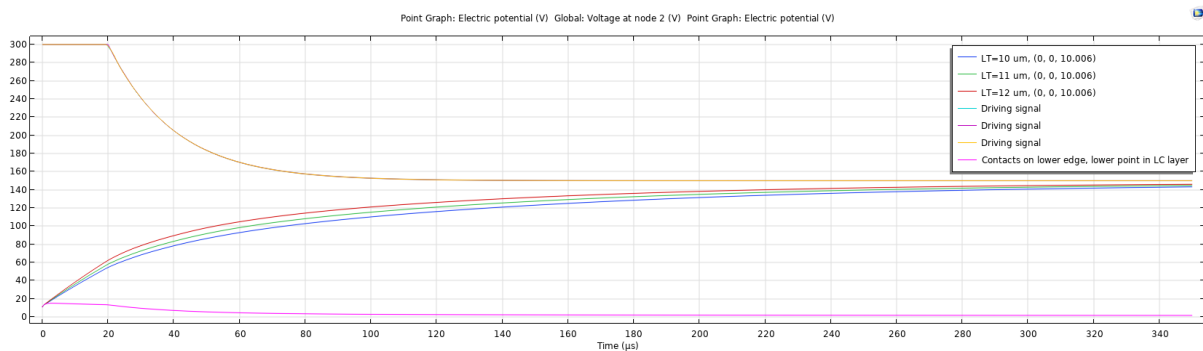
Figure 64.: Comparison of 10, 11, 12 um cell gap diffusers, contacts on short side.

Variations in thickness of dielectric coating or ITO resistance do not significantly influence diffuser switching speed, see *Figure 65* and *Figure 66*.
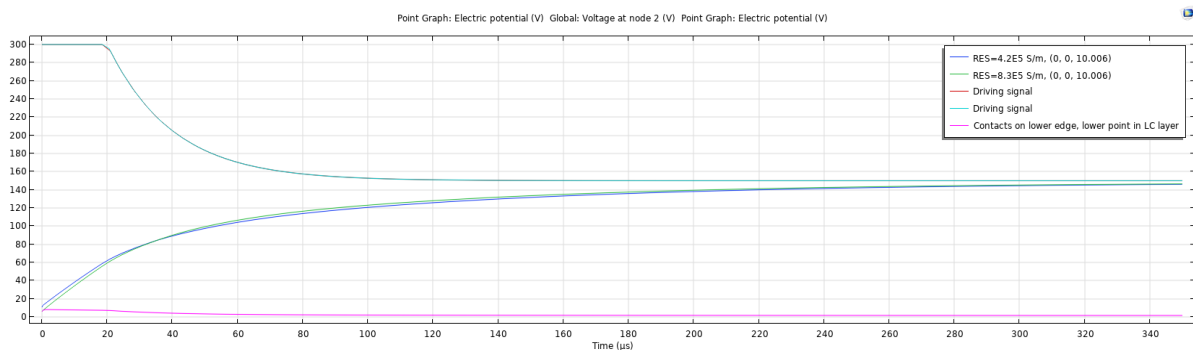
Figure 65.: Influence of ITO conductivity 80 ohm (4.2e5 S/m) versus 150 om (8.3e5 S/m).

Point Graph: Electric potential (V) Global: Voltage at node 2 (V) Point Graph: Electric potential (V)

Legend:
- DT=100 nm, (0, 0, 10.006)
- DT=12 nm, (0, 0, 10.006)
- DT=140 nm, (0, 0, 10.006)
- Driving signal
- Driving signal
- Driving signal
- Contacts on lower edge, lower point in LC layer
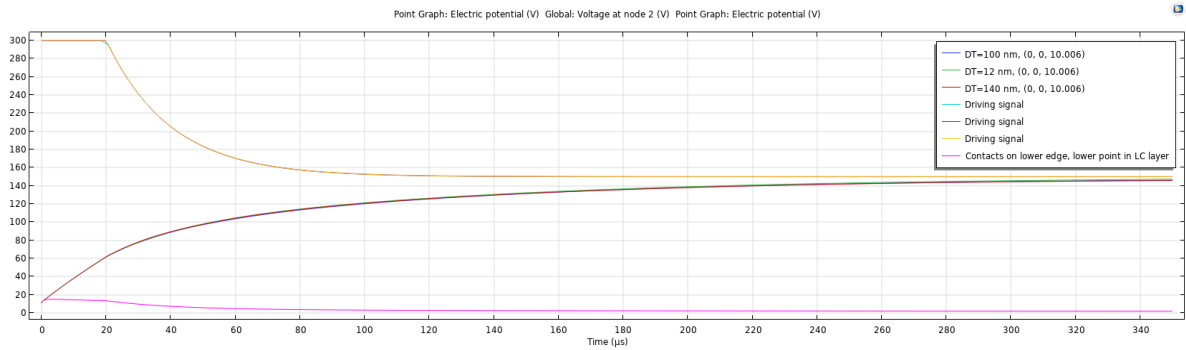
Figure 66.: Influence of dielectric coating thickness.

Modelling shows difference in how fast strip can be charged to LC switching threshold voltage depending on contact placement. The difference is rather small, for larger size diffusers 30-40 µs and for smaller diffusers without strips in active area, versions with L-type contacts also are marginally faster (less than 1 µs) than short side contact versions. We can conclude that for micro-diffusers with 10x smaller electrode area, contact placement is not important.

Dielectric coating

To maximize the portion of the applied voltage dropped across the LC layer, the capacitance of the insulators should be maximized while that of the LC layer should be minimized. To optimize the insulator capacitance, either the dielectric constant should be maximized or the layer thickness should be minimized. Since the layer thickness can't be set too low due to processing and breakdown issues, a high dielectric constant is desirable. Traditional approach is to use combined coating: 50-60 nm organic polyimide coating with dielectric constant 3.6 (n=1.58) on top of 80-100nm SiO_2 hard coating with dielectric constant of 14 (n=1.75).

So, the main requirements to the coating are:

· High dielectric constant, preferably above 3.6;

· n preferably between 1.82 (ITO) and 1.71 (LC).

We have possibility to use sputtered SiO_x coating with refractive index of 1.51. In order to improve diffuser transmittance, refractive index should be matched to adjacent layers: ITO (1.82) and LC (1.71). The standard thickness for SiO_x coatings is 260 nm, the value experimentally found for larger size diffusers that has optimum compromise between transmittance and dielectric breakdown for 300x400mm displays. For micro-difusers, dielectric breakdown is less common due to smaller active area so thickness can be adjusted.

Diffuser transmittance dependance on dielectric layer thickness quick analysis was carried out using Filmetrics.com online tool. It does have capability to use n-k data and perform optimization but could give insights for further studies. Results indicated that overall diffuser transmittance is dependent on dielectric layer thickness and previously used 260nm SiO_x thickness should be decreased to 200 nm, see Figure 67.
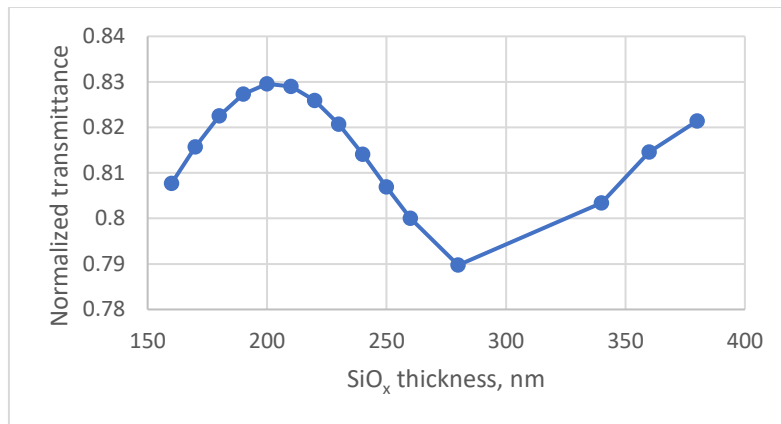
Figure 67.: LCD cell transmittance calculation depending on SiO_x thickness using Filmetrics.com.

The thickness optimization and tuning of refractive index will be performed in this work so that overall stack transmittance is improved.

4.3 Experimental part

Optimization of antireflective layer on multifocal diffuser outer boundary

In order to choose one of modelled BBAR layer design over other (CS_2 vs CS_3) for the final design, both BBAR stacks were coated on glass. Industrial coater FHR Line2500.H was used for layer deposition on 400x300x0.55mm soda-lime glass by physical vapour deposition method. Silica and nyobium oxide rotable targets were used in reactive oxygen/argon atmosphere. Prior deposition, to ensure cleanliness of the surface, ion etching was used with following parameters: 50 mm/s, 4 passes under target and Argon flow at each of 3 sections – 250, 40, 150 sccm. After each layer was deposited (see process settings in Figure 68), sample was collected and its thickness was measured by Dektak XT profilometer using Vision 64 software. Approximately 2-3 experimental runs per layer were necessary to reach specified thickness by changing glass conveyor speed under target (process speed, mm/s) and number of passes under target (number of cycles), see Figure 68.
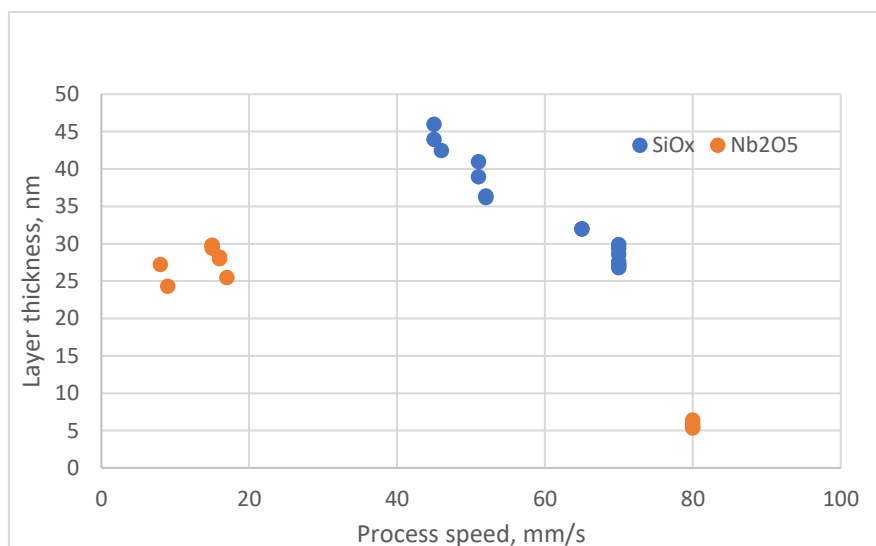
Figure 68.: Nb_2O_5 and SiO_x layer sputtering conditions.

Parameters that were kept constant – 4.85×10^{-6} bar, process temperature 58 °C, rotation speed of target 15 mm/s, DC power 15 kW, 675 V and Ar flow at 3 sections – 900, 150 and 450 sccm. Oxygen flow for Nb_2O_5 process was set to 95 sccm and for SiO_x it was increased to 102.1 sccm for stable process.

Coating stacks were measured with Ocean Optics Flame T spectrometer, see Table 14 and Figure 69.

Table 14.: Modelled BBAR stacks (one surface) and experimental results (two surfaces, one coated).

	Model			Experimental results		
Stack	Commercial	CS_2	CS_3	Commercial	BBAR_2	BBAR_3
Nb_2O_5, nm	10	10	12	-	11	12
SiO_x, nm	40	40	32	-	39	32
Nb_2O_5, nm	110	120	115	-	119	115
SiO_x, nm	80	90	88	-	85	88
Average reflection, visible range	1.3 %	0.6 %	0.6 %	5.1 %	4.8 %	4.8 %
Reflection at 450 nm (B)	0.9 %	0.3 %	0.5 %	5.2 %	5.0 %	6.9 %
Reflection at 532 nm (G)	0.4 %	0.6 %	0.4 %	4.3 %	4.9 %	4.6 %
Reflection at 635 nm (R)	0.2 %	0.3 %	0.3 %	3.5 %	4.2 %	4.5 %
Reflection sum at RGB	1.57 %	1.18 %	1.19 %	13.0 %	14.1 %	16.0 %

While average reflection BBAR_2 (respective model is CS_2 from COMSOL) stack is equal to BBAR_3 (Optilayer), it has higher reflectivity for green wavelength.
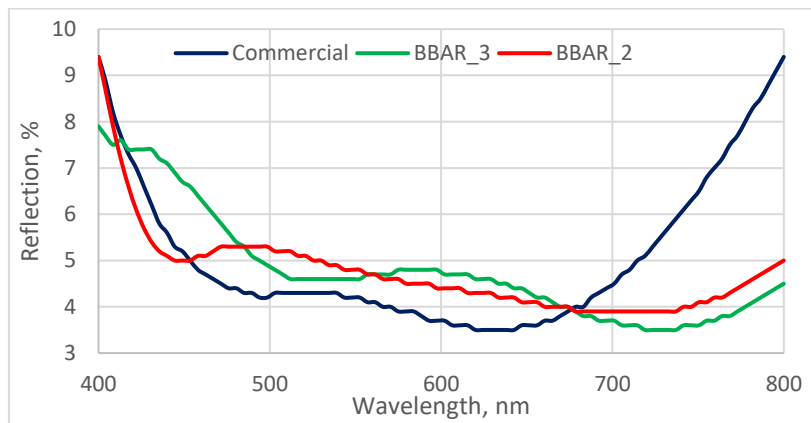
Figure 69.: BBAR_2 and BBAR_3 coating reflectance spectra, taken with Ocean Optics Flame T spectrometer compared to commercial AR

Selected BBAR_3 stack was then coated on ITO glass (BBAR_3_ITO) and compared to commercially available BBAR_1 coated ITO glass, see Figure 70.
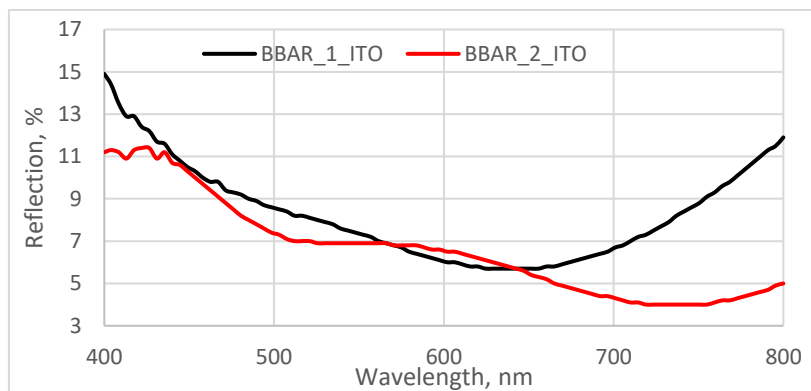
Figure 70.: BBAR_3 coating reflectance compared with BBAR_1 on ITO coated glass.

The results also show that BBAR_3 stack normalized reflection 6.9 % is better than previously used BBAR_1 stack (7.2 %) and can provide small improvement of the overall stack. However, the most of the gain comes from decreased reflectivity at RGB wavelengths – 23.1 % vs 24 %.

When we compare model reflectivity to practical results, we see that the nature of reflection-wavelength curve is close but not exactly, especially at the low and long wavelengths, see Figure 71.
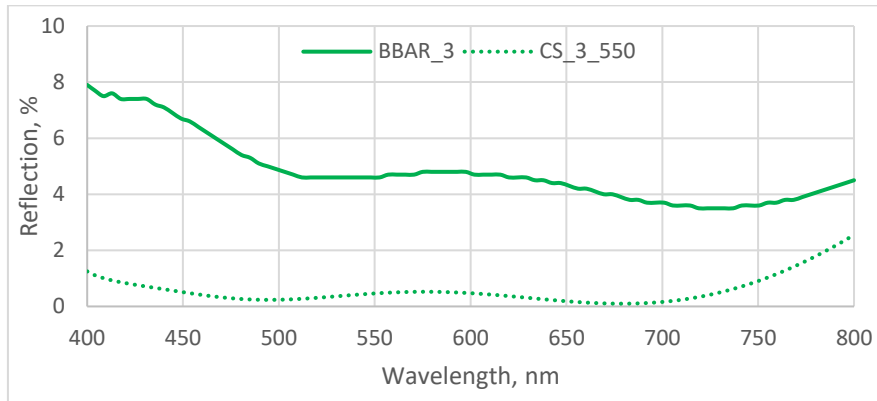
Figure 71.: Comparison between modelled (CS_3_550, one surface) and experimental (BBAR_3, two surfaces – one coated) stack reflectivity.

This difference can be explained by modelling constraints. The disadvantage of COMSOL software is that it cannot use very thin (nm) layers with combination of thick (mm) layers and solve problem by effective meshing, so predefined surfaces are used, like **Thin dielectric film** in Geometric Optics. This way for multiple dielectric layer stack is easily defined but complex refraction index of very thin layer can't be used. Instead, n-k value of specific wavelength, values at 550 nm are used. However, we can improve simulation by changing wavelength specific n-k values.

Material n-k values were measured with spectral ellipsometer. SiO$_x$ sputtered coating is coated in two passes under target, so bottom layer closer to glass surface have lower n value than top layer, see Figure 72.
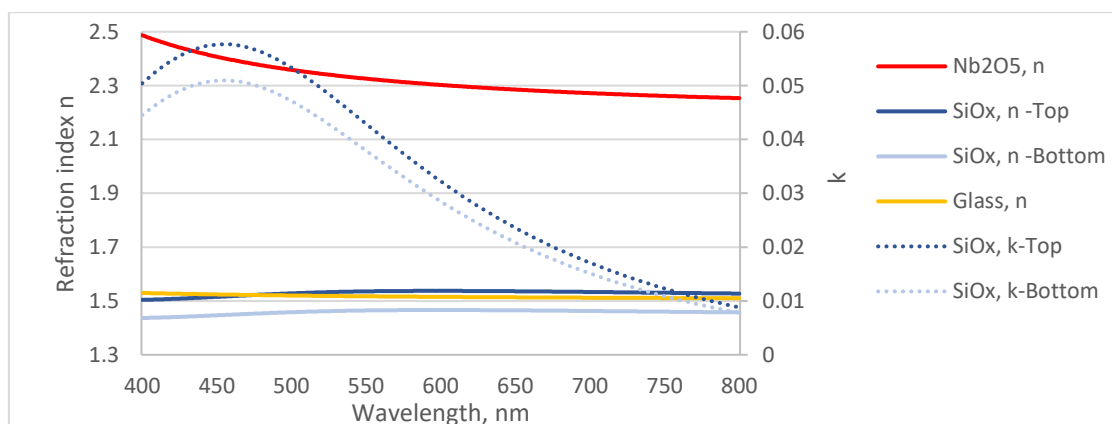
Figure 72.: Refractive indexes n, k for stack materials.

According to XPS data, Si:O atomic ratio is 35:65. It should be noted, that after SiO$_x$ surface is heated in atmosphere for 1h at (if done in production processes), the ratio of the top layer changes to 30:70. This may explain, that temperature treatment of SiO$_x$ coated ITO glass, reduced defects due to less active surface, if SiO$_x$ is used for direct contact with LC. Niobium oxide also is deposited in two passes under target but is homogeneous, see Figure 72. Atomic ratio by XPS data is 42:58, Nb:O. Glass and Nb$_2$O$_5$ have k value of zero, but the highest k – value for SiO$_x$ is at 450 nm, so to maximize its impact, COMSOL model n-k and vacuum wavelenght, were changed to 450 nm wavelength.

Model in Optilayer software with n-k dispersion data was also used for comparison purposes. When comparing the results, we find that even Optilayer software gives cannot predict precise curve but improved COMSOL model provide more closer results, see Figure 73.
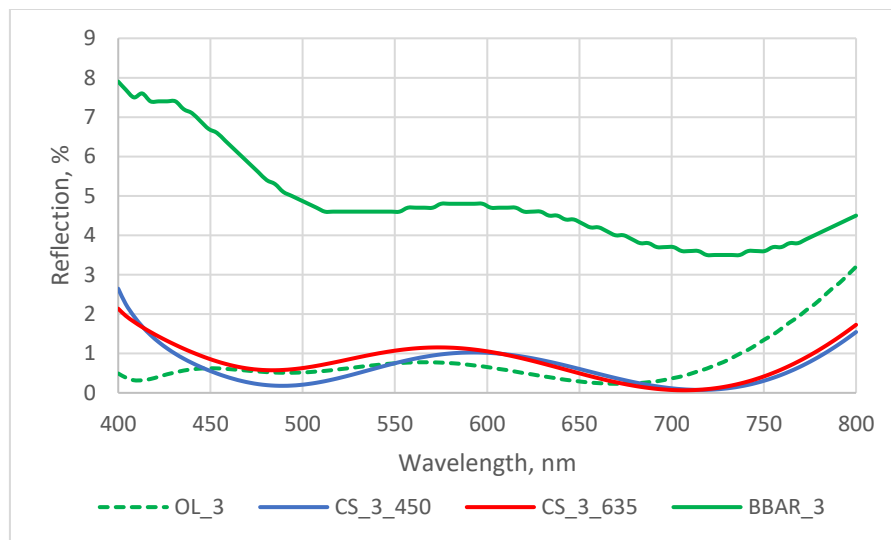
Figure 73.: BBAR_3 coating comparison with various models. Blue- COMSOL with n at 450nm, red – COMSOL with n at 635 nm, green- Optilayer.

For wavelength specific applications, like optic chip in the RGB laser projection system, COMSOL model can provide effective input for AR layer coating optimization experiments. As the result, thickness of individual layers was adjusted, resulting in improved AR properties.

Optimization of transparent conductive layer

Number of experiments to improve ITO layer conductivity was carried out. ITO layer is sputtered on soda lime glass using FHR Line 2500H PVD machine by low temperature process, so post process temperature treatment is used. Transmittance was measured by Ocean Optics Flame T spectrometer. It was found that 30 min are sufficient for 1.6 % transmittance improvement and nearly doubling the conductivity of 107 nm layer, see Table 15.

Table 15.: Temperature treatment impact on ITO layer transmittance.

Treatment	Transmittance at 550nm	Resistance, ohm/sq
none	84.4 %	79
30 min inline kiln 300 °C	86.0 %	45
60 min inline kiln 300 °C	85.7 %	45
90 min inline kiln 300 °C	85.7 %	41

According to the literature, reductive atmosphere can improve the result. High temperature tube furnace Carbolite Gero was used for 300 ℃ thermal treatment, 120 min, 5 % H_2/Ar atmosphere. Results were characterized using Jenway 6310 spectrophotometer. As in previous case, properties have improved but in the same relative degree, so we can conclude that no additional effect of reductive atmosphere is detected, see Table 16.

Table 16.: Temperature and reductive condition impact on ITO layer transmittance.

Treatment	Transmittance at 550nm	Resistance, ohm/sq
none	91.6%	76
120 min furnace 300 °C, 5% H_2/Ar atmosphere	93.0%	49

It would be more effective if high temperature treatment was done during process thus saving time and energy. In the next step, sputtering process temperature was increased and process conditions optimized further. Sample, ITO150, was prepared by increasing sputter chamber heater temperature to 150° C. No improvement was obtained over postprocess temperature treatment method. ITO deposition parameters for 107 nm thick layer were varied with different partial oxygen content in reactive atmosphere. It was found, that the optimum oxygen content is achieved at oxygen flow of 18 sccm (standard cubic centimeters per minute), see Table 17., as it offers best transmittance

and conductivity. Increasing oxygen flow rate (hence more oxygen content in reactive atmosphere) improves transmittance but significantly lowers conductivity.

Table 17.: Oxygen content in sputtering process impact on ITO properties.

Sample Nr.	Oxygen flow	Transmittance at 550 nm (normalized), %		n at 550 nm		Resistance, Ω/sq	
	rate, sccm	before treatment	after treatment	before treatment	after treatment	before treatment	after treatment
ITO150	18	91.4	92.9	2.02	1.97	73	46
6	8	84.4 (66.9)	88.7	2.05	—	207	31
7	14	(80.7)	(84.8)			80	26
1	18	91.6 (83.5)	93.0	2.02	1.97	76	49
5	22	(84.4)	(84.5)	-	-	97	65
2	28	92.1 (84.4)	92.1	2.07	1.98	174	97
3	38	(84.0)	-	-	-	-	-
4	48	(84.1)	-	-	-	-	-

Two thicker ITO versions were prepared, 167 nm and 288 nm, with 18 sscm oxygen flow settings. After the initial normalized transmittance measurement by Ocean Optics spectrometer, no significant differences were observed, see Table 18. and no further experiments were carried out. Two more versions of 110-120 nm ITO were prepared, by changing conveyor speed and number of cycles (pass under target) so that sputtering speed is varied. It was found that 8 mm/s is the optimum process (conveyor) speed.

Table 18.: ITO thickness and deposition speed effect on transmittance and resistance.

ITO thickness	Substrate conveyor	Transmittance at 550 nm (normalized) %		n at 550 nm		Resistance, Ω/sq	
	speed and cycles	before treatment	after treatment	before treatment	after treatment	before treatment	after treatment
167 nm	20 mm/s, 6x	92.1 (83.5)	94.0	2.05	1.97	64	38
288 nm	10 mm/s, 4x	93.1(84.1)	95.6	2.03	1.97	65	32
107 nm	8 mm/s, 2x	91.6 (83.5)	93.0	2.02	1.97	76	49
114 nm	20mm/s, 4x	82.4 (83.8)	82.9 (85.1)	-	-	68	33
~110 nm	5mm/s, 1x	83.0 (83.5)	82.1 (83.8)			74	32

Ellipsometry measurements were taken with spectral ellipsometer Woollam RC2 – XI at incident light angles of 40, 45, 50, 55, 60, 65 and 70 degrees, and sheet resistance with Hall measurement system parameters:

- o Current: 10 mA;
- o Magnetic field: B=0.55 T;
- o Measurement temperature: 300 K.

We can see that for low temperature deposition process, 120 nm ITO coating is needed to reach 80 ohm/sq. conductivity compared to high temperature deposition process, (30 nm, 80 ohm/sq., n=1.82, supplier Token) and its refractive index is also higher, see Figure 74.
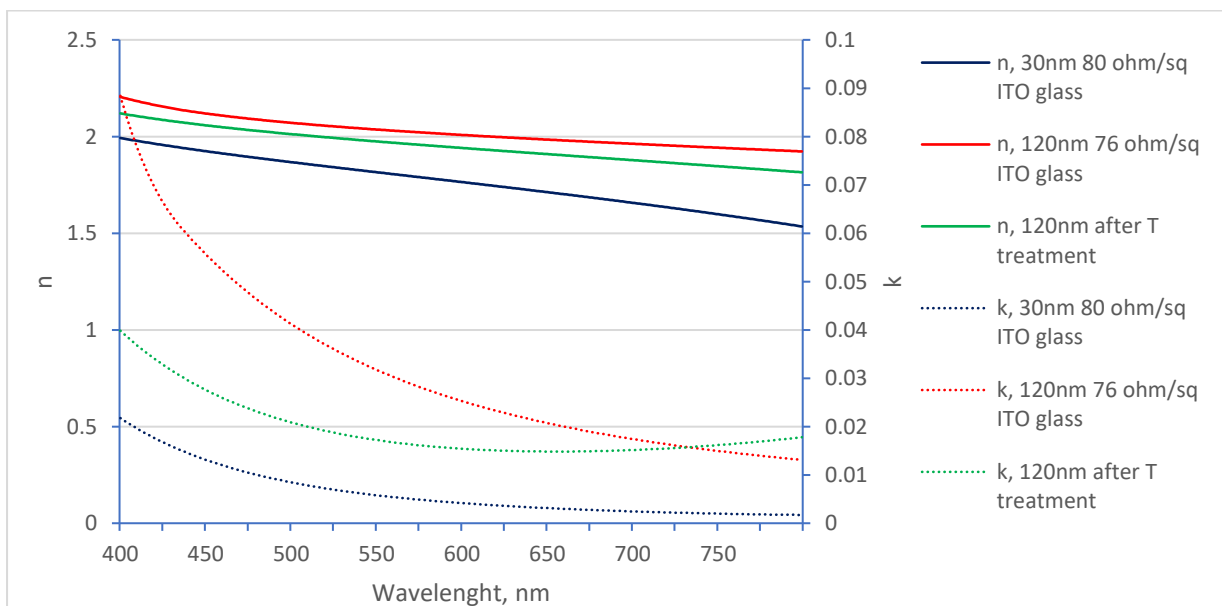
Figure 74.: Refractive indexes n, k of ITO glass samples.

Observed improvement of conductivity and transmittance after temperature treatment can be used to improve layer properties, by its effect on n and k values, reducing layer absorbance, see Figure 75. This must be taken into account when designing all layer stack.
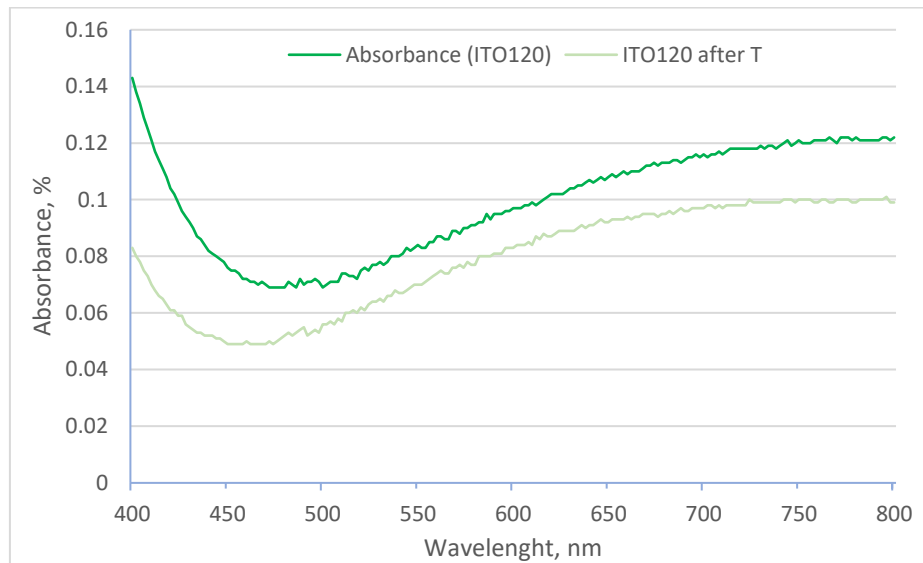
Figure 75.: Temperature treatment effect on ITO layer absorbance.

As the last step for conductive layer optimization, effect of barrier and index matching layer (SiO_x) thickness used as under ITO on transmittance was evaluated. After the ITO layer was kept for 90 min at 300 $°C$, it was found that the best results have 30nm SiO_x coating under ITO layer, see Table 19. Ocean Optics Flame T- UV-Vis, slit size 25um with DH-2000-S-DUV-TTL light source was used for coated substrate measurements.

Table 19.: SiO_x layer thickness impact on ITO coated glass transmittance.

Layer under ITO	Transmittance, at 550nm	Note
none	84.9%	Baseline
20 nm n=1.514	84.3%	
30nm n=1.514	85.7%	Best improvement by 0.8%
40nm n=1.514	83.8%	

Dielectric layer.

The first experiment was to see whether cell transmittance can be improved by changing SiO_x coating thickness to thinner 200nm as modelling suggested.

22x15 mm diffuser cells were prepared and their open state transmittance spectra was measured using Ocean Optics T-Flame UV-VIS spectrometer. The measured results confirm model

results. Use of thinner 200 nm coating have improved normalized transmittance from 88.1±0.1 % to 89.2±0.2 %. The difference increases nearer to 400 nm wavelength, see Figure 76.
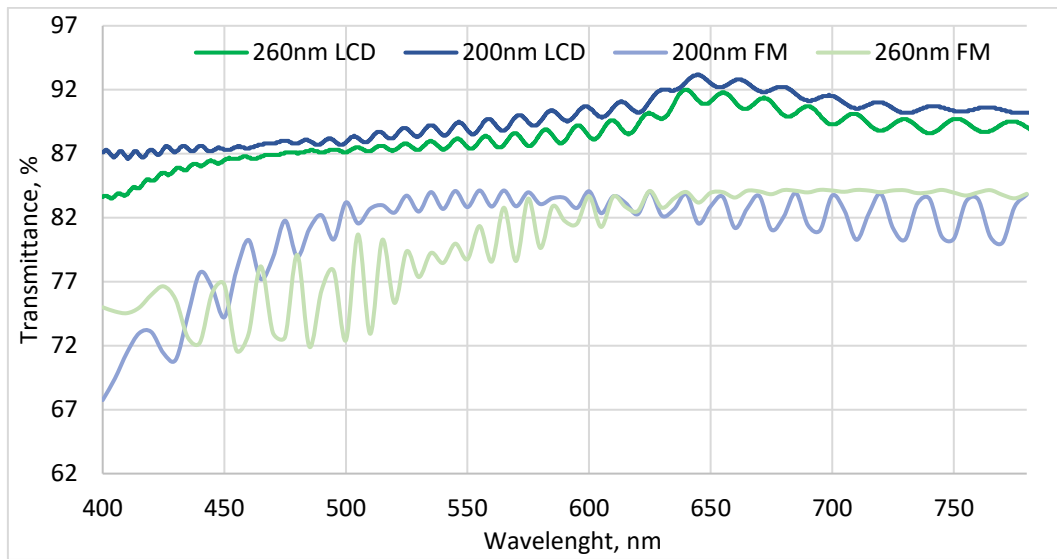
Figure 76.: Microdiffuser (LCD) actual transmittance depending on SiO$_x$ coating thickness and its model using Filmmetrics.com (FM).

To explain differences at 450 nm, more precise model was made. Full display stack was modelled with Optilayer and CODE V software, see Figure 77., using layer materials precise data. Coating n-k data was obtained with spectral ellipsometer Woollam RC2 – XI at incident light angles of 60, 65 and 70 degrees and used for models. Thick layers (glass, LC) were defined as non-coherent to avoid interference.
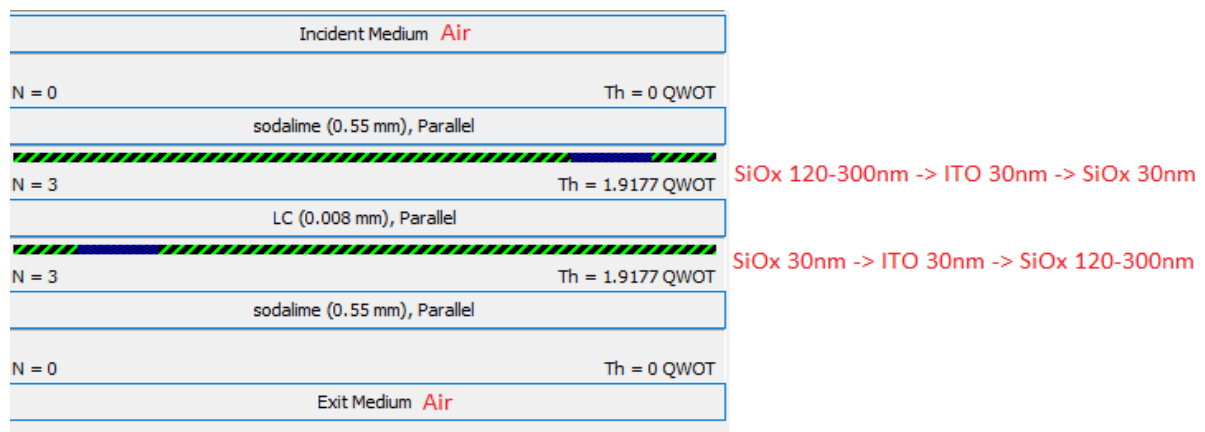
Figure 77.: Diffuser model in Optilayer software.

Both software models predict that 200 nm would give better transmittance but fail to explain behavior near 450 nm, see Figure 78.
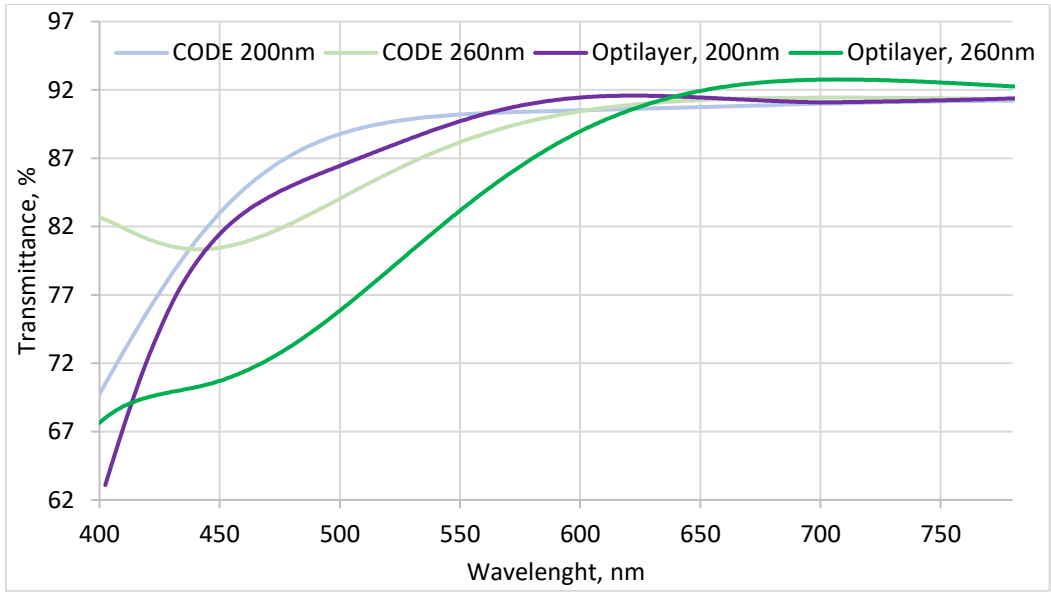
Figure 78.: Transmittance dependence on SiOₓ coating thickness, calculated by CODE and Optilayer models.

Increased transmission difference below 450 nm can be explained by increasing thin film absorptance at these wavelengths. Half stack (glass-LC) simulation shows that it is not only noticeable higher at shorter wavelengths but also changes depending on SiO_x thickness, see Figure 79. Two materials with extinction coefficient larger than 0 in this region are ITO and SiO_x, so they can create interference changing overall transmission.
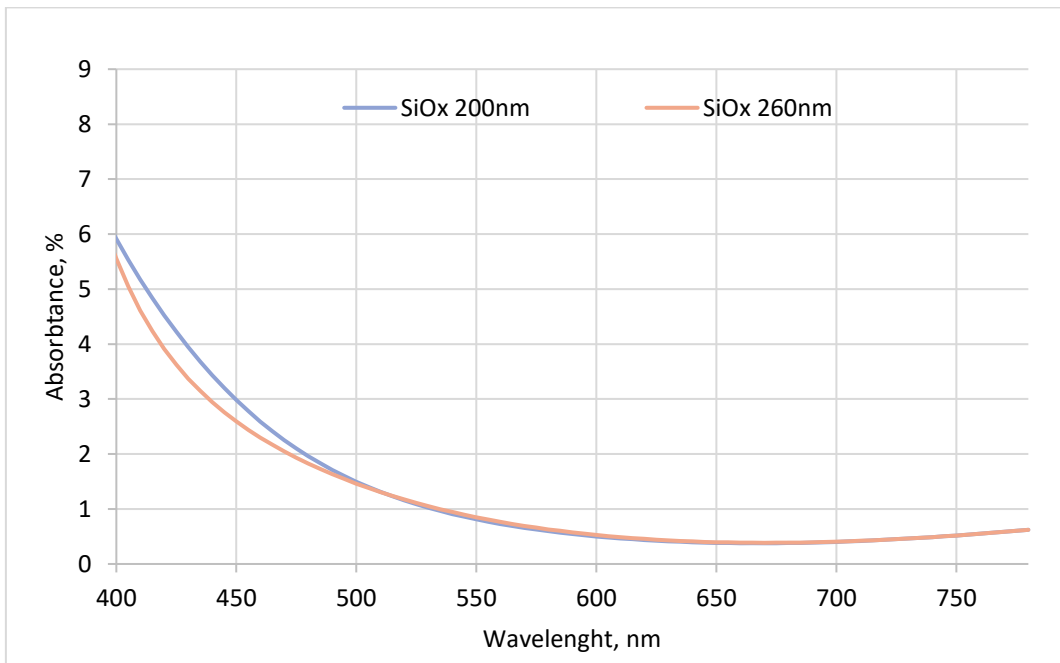
Figure 79.: SiOₓ layer variation influence on diffuser absorptance.

The next experiment was to find out how much SiO_x refractive index can be changed to improve transmittance even further by closer index matching between stack layers. Industrial coater FHR Line2500.H has limited options for changing sputter process conditions. Among them, most likely oxygen flow and surface temperature could provide larger impact on coating properties. Experiment was carried out using on glass and ITO/glass substrates in industrial process with following settings, see Table 20., in order to change refraction index.

Table 20.: SiO_x sputtering experiment parameters.

Sample Nr.	ITO thickness, nm	SiO_x thickness, nm	O_2 flow, sccm	Substrate temperature, ℃	Treatment temperature, ℃
SiO120C	-	240	96	150	-
SiOx-O+	-	248	102	58	-
SiOx-O-	-	226	88	58	-
T-130	106	241	96	58	130
T-300	106	241	96	58	300

Optical microscope measurements were carried out with Nikon 150. A visually similar structure was observed in all sputtered films. Optical image of the SiO_x-O- sample (Figure 80.) clearly shows that silicon particles less than 2 µm in diameter agglomerate in the sputtered films.
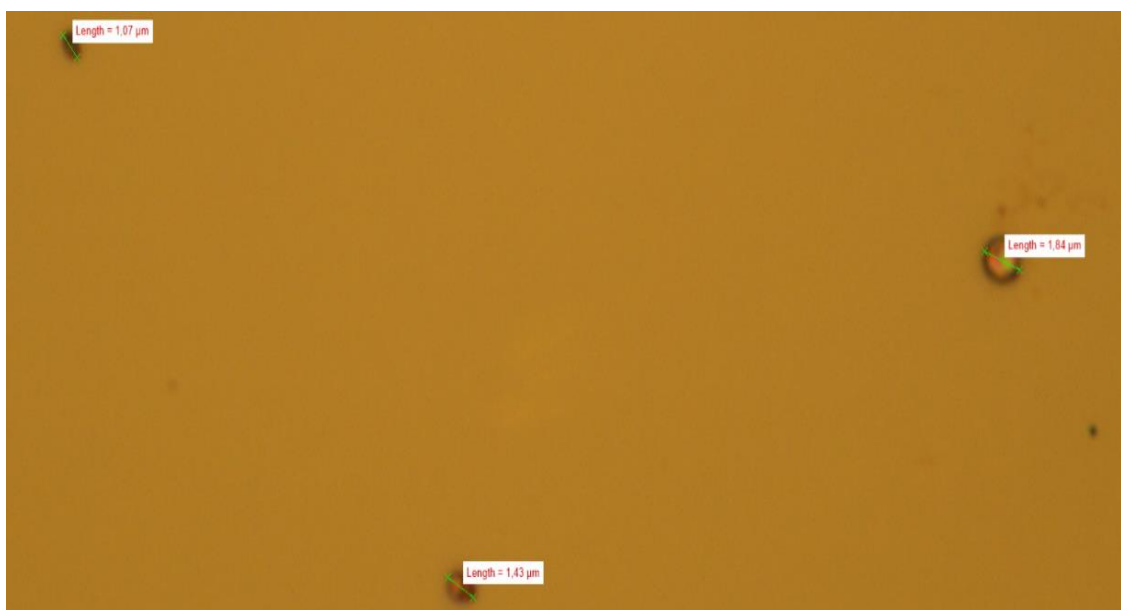
Figure 80.: SiO_x-O- sample image in optical microscope.

Transmittance and reflection spectra using Agilent Cary 7000 of samples are given in Figure 81. and Figure 82. respectively. From these spectra it is clearly seen that SiOx-O- samples are characterized by lower transmittance and higher reflection at λ < 650 nm. Maxima is seen in reflection spectra due to constructive interference of thin films when ITO is added to the stack.
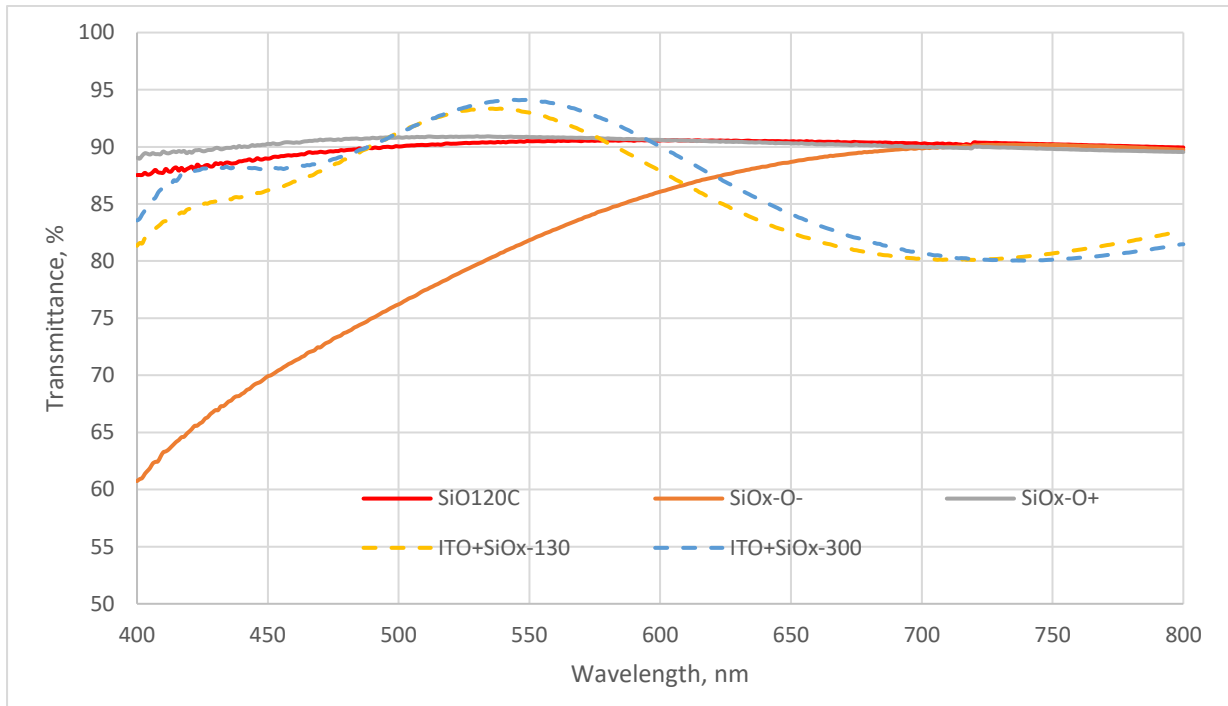
Figure 81.: Transmittance spectra of SiO$_x$ samples.
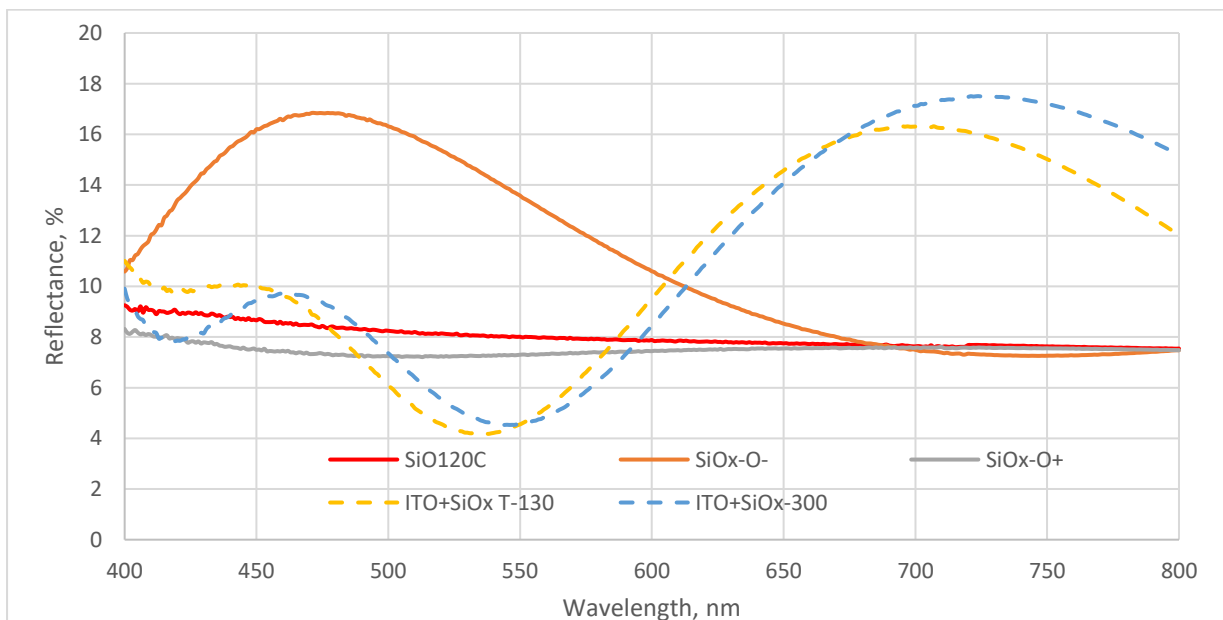
Figure 82.: Reflection spectra of SiO$_x$ samples.

XPS measurements were carried out with ESCALAB Xi. XPS depth profiling measurements for all samples are given in Figure 83. From these measurements it is well seen that oxygen content in

sputtered films varies between 64.5 % and 65.5 %. This means that x value in SiO_x is changing from 1.82 to 1.86.
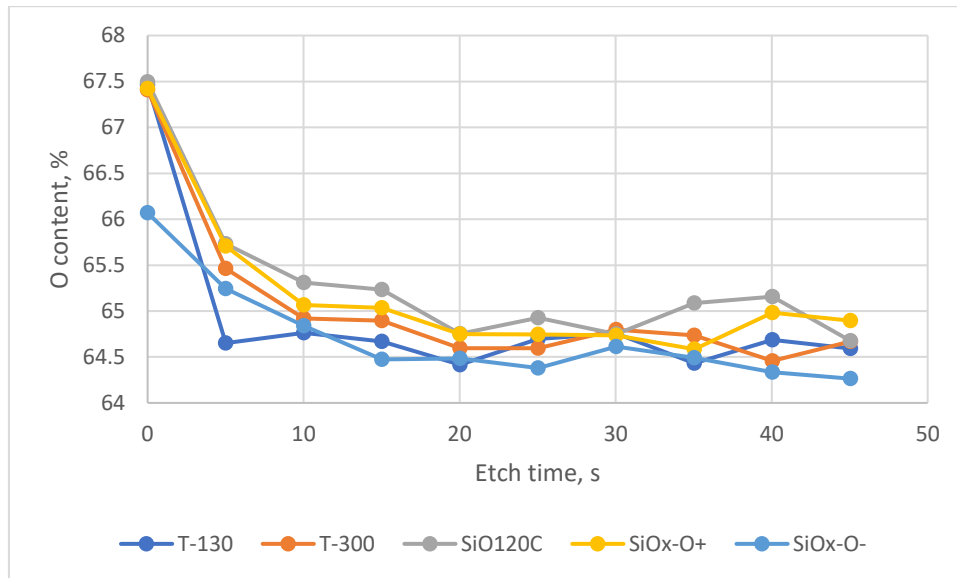
Figure 83.: PZ43 samples XPS depth profiling measurements.

Ellipsometry measurements with spectral ellipsometer Woollam RC2 – XI at are given in Figure 84.
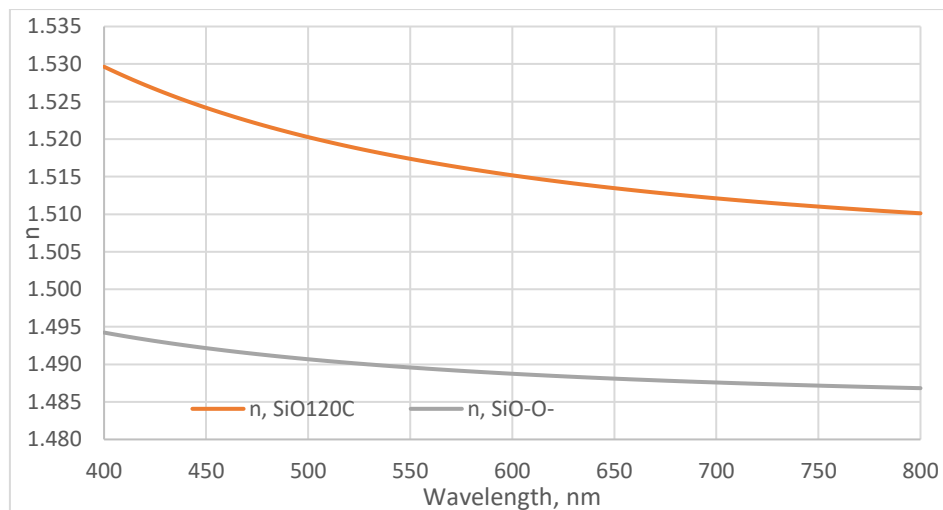
Figure 84.: SiO_x samples ellipsometry measurements.

It was impossible to get refractive index curves for some samples. SiOx-O- sample was not fully transparent, most likely this sample consisted of silicon phase mostly (due to insufficient O_2 during process). T-130-A, T-130-B, T-300-A, T-300-B samples consisted also of ITO between glass and SiO_x sputtered film. This made it much more difficult to choose the appropriate model. The

combination of these reasons led to the fact that it was possible to obtain a refractive index curve only for SiO120C and SiOx-O+ samples.

X-Ray Diffraction spectra for all samples are given in Figure 85 using XRD Rigaku. Peak identification was carried out with "Match!" software. From these spectra it can be concluded that crystal structure is not forming in SiO_x film even after thermal treatment. All crystal structure peaks are related to ITO coating under SiO_x film.
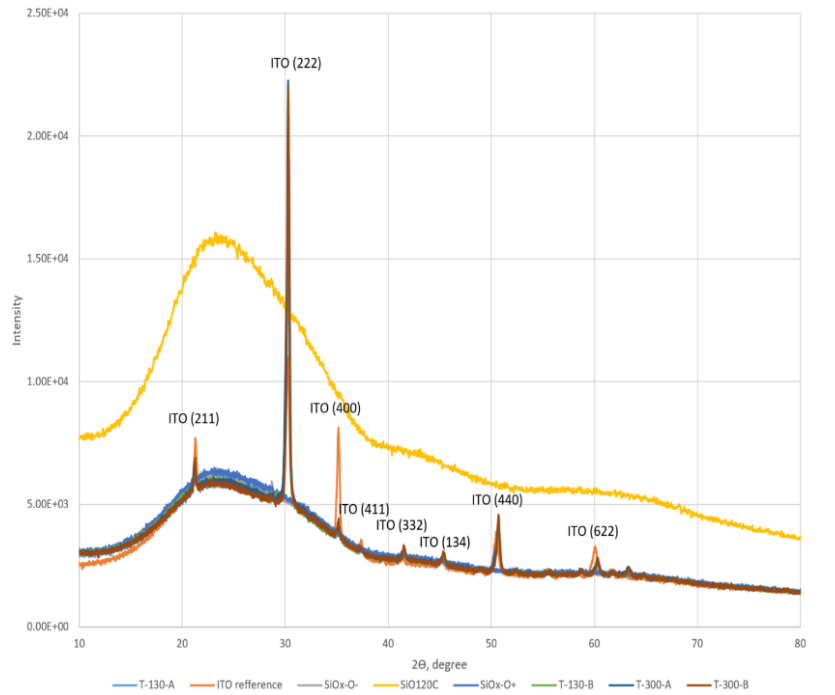
Figure 85.: XRD measurements for SiOx samples with different substrate or treatment temperature.

The experiment results are summarized in Table 21.

Table 21.: Summarized measurement data for SiO_x sputtering experiment.

Sample Nr.	Transmittance at 550 nm, %	Reflection at 550 nm, %	n at 550 nm	Surface roughness, nm
SiO120C	90.5	8.0	1.52	1.5
SiOx-O-	81.8	13.6	–	1.3
SiOx-O+	90.8	7.3	1.49	1.5
T-130-A	93.0	4.6	–	3.5
T-300-A	94.1	4.6	–	3.4

Comparing to typical process n=1.51, increase of refraction index is not significant. Sputtering results often are dependent on machine design (chamber, target dimensions), so next number of

further experiments using small scale vacuum coater SAF 25/50, TruPlasma DC Series 4000, TRUMPF Hüttinger was carried out to see whether the refraction index can be increased more.

SiO$_x$ films were prepared on soda-lime glass using pulsed DC magnetron sputtering with target Si 99.999 % purity, 3 inches in diameter and 6 mm in thickness. For all samples following parameters of magnetron sputtering were constant: Ar flow (50 sccm), power (100 W), substrate average temperature (34 ℃), distance between target surface and substrate (13 cm), pulsed DC frequency (100 kHz), pause duration time (3 μs). Other parameters are shown in Table 22.: SiOx sputtering parameters with DC mode.Table 22.

Table 22.: SiOx sputtering parameters with DC mode.

Sample Nr.	O2 flow, sccm	Working pressure, mTorr	Voltage, V	Current, mA	Thickness, nm
S263	3,2	3.1	405	246	212
S264	3.8	2.2	418	238	180
S265	2.8	4.1	441	226	196
S266	2.4	6.0	435	230	285

The choice of oxygen flow was based on characteristic curves of voltage versus oxygen flow Figure 86.
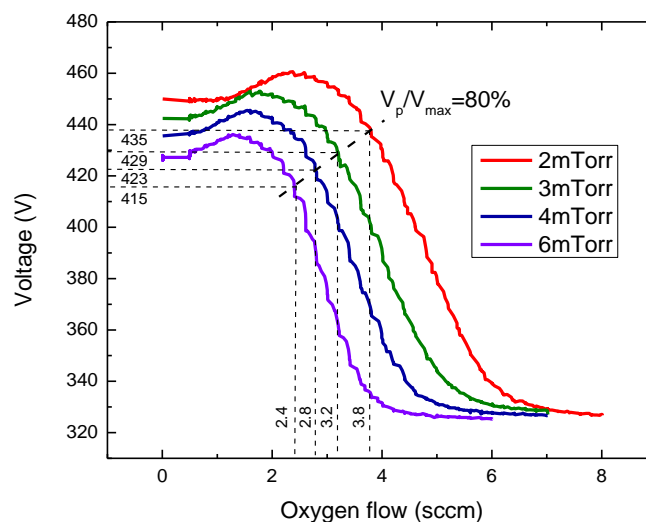
Figure 86.: Dependence of the DC magnetron sputtering voltage on the oxygen flow.

Ellipsometry measurements were taken with spectral ellipsometer Woollam RC2 – XI see Figure 87. Working pressure change did not significantly affect the refractive index of SiO$_x$ sputtered film.
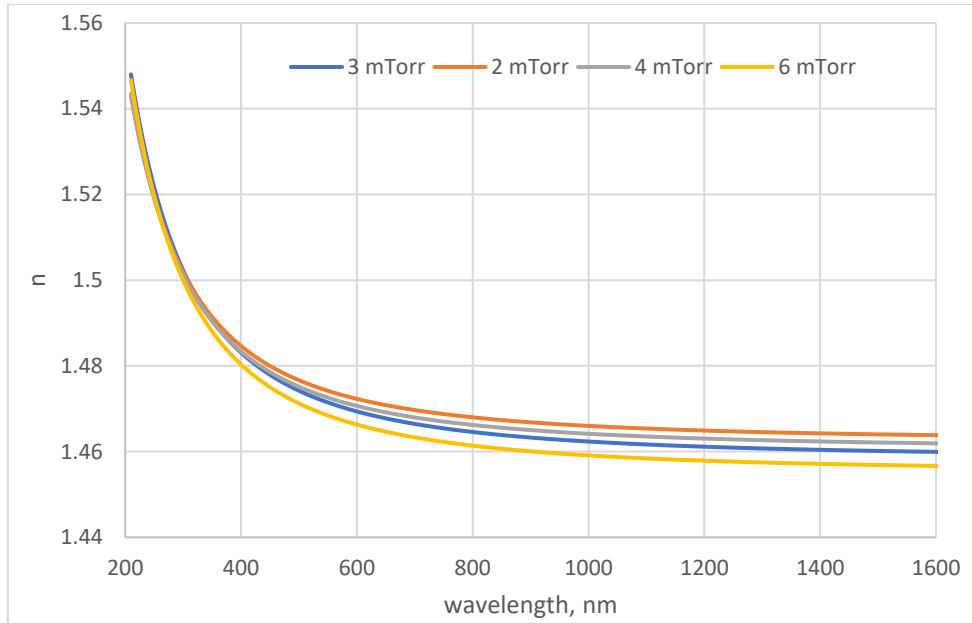
Figure 87.: SiOₓ/glass ellipsometry measurements.

SiO$_x$ on glass samples data are summarized in Table 23.

Table 23.: Summarized data for SiO$_x$ on glass samples with DC mode.

Sample Nr.	Working pressure, mTorr	Surface roughness, nm	n (550 nm)
S263	3	1.0	1.471
S264	2	1.0	1.474
S265	4	2.0	1.473
S266	6	1.5	1.468

Obtained refractive index results of SiO$_x$ coating doesn't show the desired improvements above 1.51, therefore other material must be considered. Material wise, SiO$_x$N$_y$ could be potential candidate. Its dielectric constant is also higher than SiO$_x$, one more reason to select this material.

Next experiments were done to produce SiO$_x$N$_y$ with different x and y values as it is the way to obtain different coatings with different n, first on smaller size glass samples.

SiO$_x$N$_y$ coatings were prepared on soda-lime glass using BDS-HF200/300 BDISCOM Srl RF magnetron sputtering system. Target material for SiO$_x$N$_y$ sputtering was Si$_3$N$_4$ with 99.999 % purity, 3 inches in diameter and 6 mm in thickness. For all samples following parameters of magnetron sputtering were constant: Ar flow (50 sccm), substrate average temperature (32 ℃). Parameters that changed for each sample are shown inTable 24.

Table 24.: SiO$_x$N$_y$ RF sputtering parameters.

Sample Nr.	O$_2$ flow, sccm	Working pressure, mTorr	DC bias voltage, V	Power, W	Thickness, nm	Distance between target and substrate, cm
S268	0	3.6	213	75	70	13
S269	10	4.2	243	100	30	13
S270	2.5	3.6	242	100	45	13
S271	5	3.6	239	100	35	13
S272	1	3.6	239	100	45	13
S273	0	2.2	273	100	-	8

XPS depth profiling measurements for S268 (0 sccm O$_2$ flow) and S271 (5 sccm O$_2$ flow) samples are given in Figure 88. Nitrogen content did not exceed 5 % even when no oxygen was used for reactive sputtering. It means that it is not possible to effectively vary nitrogen in obtained SiO$_x$N$_y$ coatings with chosen RF sputtering technology. Alternative is DC magnetron sputtering that was tested further.
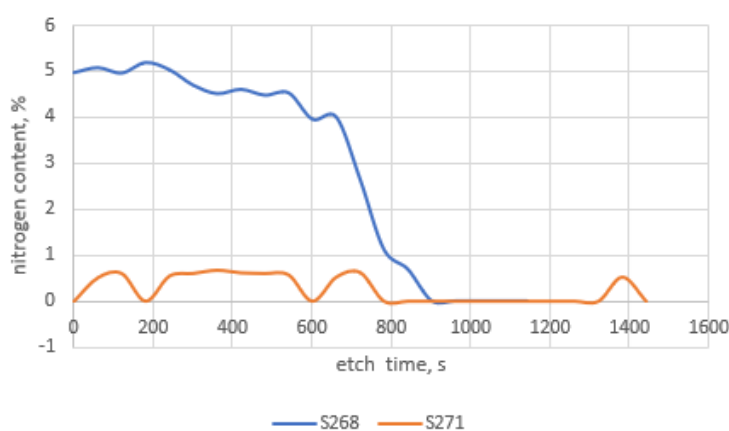
Figure 88.: XPS depth profiling measurements for S268 and S271 samples.

SiO$_x$N$_y$ coatings were prepared on soda-lime glass lime using pulsed DC magnetron sputtering system in Ar/O$_2$/N$_2$ atmosphere that consists of vacuum coater SAF 25/50, TruPlasma DC Series 4000, TRUMPF Hüttinger. Target material for SiO$_x$ sputtering was Si with 99.999 % purity which was 3 inches in diameter and 6 mm in thickness. For all samples following parameters of magnetron sputtering were constant: power (100 W), distance between target surface and substrate ($11.5\ cm$), pulsed DC frequency ($100\ kHz$), pause duration time ($3\ \mu s$). Most important process parameters that changed for each sample are given in Table 25.

Sample Nr.	Voltage, V	Current, mA	p_{N_2}, Torr	p_{O_2}, Torr	p_{Ar}, Torr	Pressure before process, Torr
S276	447	223	4.25E-05	5.90E-06	5.30E-04	6.00E-06
S278	459	218	6.80E-05	4.50E-06	5.40E-04	5.00E-06
S279	461	216	1.20E-04	6.00E-06	5.00E-04	4.40E-06
S280	548	183	1.30E-04	5.30E-08	6.30E-04	6.00E-06
S281	605	164	8.30E-05	8.20E-06	5.40E-04	7.50E-06
S283	529	188	1.30E-04	9.80E-07	6.10E-04	4.00E-06

Transmittance spectra of SiO_xN_y/glass samples measured by Agilent Cary 7000 spectrophotometer are given in Figure 89. Transmittance decreases with refractive index increasing. Lowest total transmittance is observed in sample with highest refractive index (S280), but at 550 nm transmittance for this sample is similar to other SiO_xN_y/glass samples.
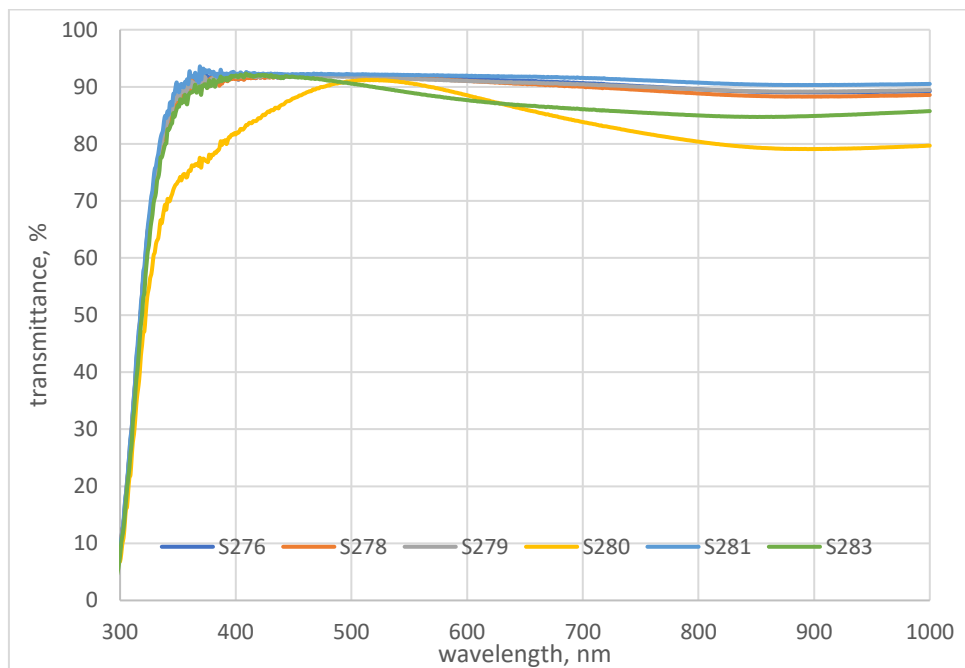
Figure 89.: SiOₓNᵧ/glass samples transmittance spectra.

Ellipsometry measurements were taken with spectral ellipsometer Woollam RC2 – XI at incident light angles of 45, 50, 55, 60, 65 and 70 degrees. Spectral ellipsometer measurements for all samples are given in Figure 90. It is clearly seen that using this technology it is possible to adjust SiO_xN_y coating refractive index.
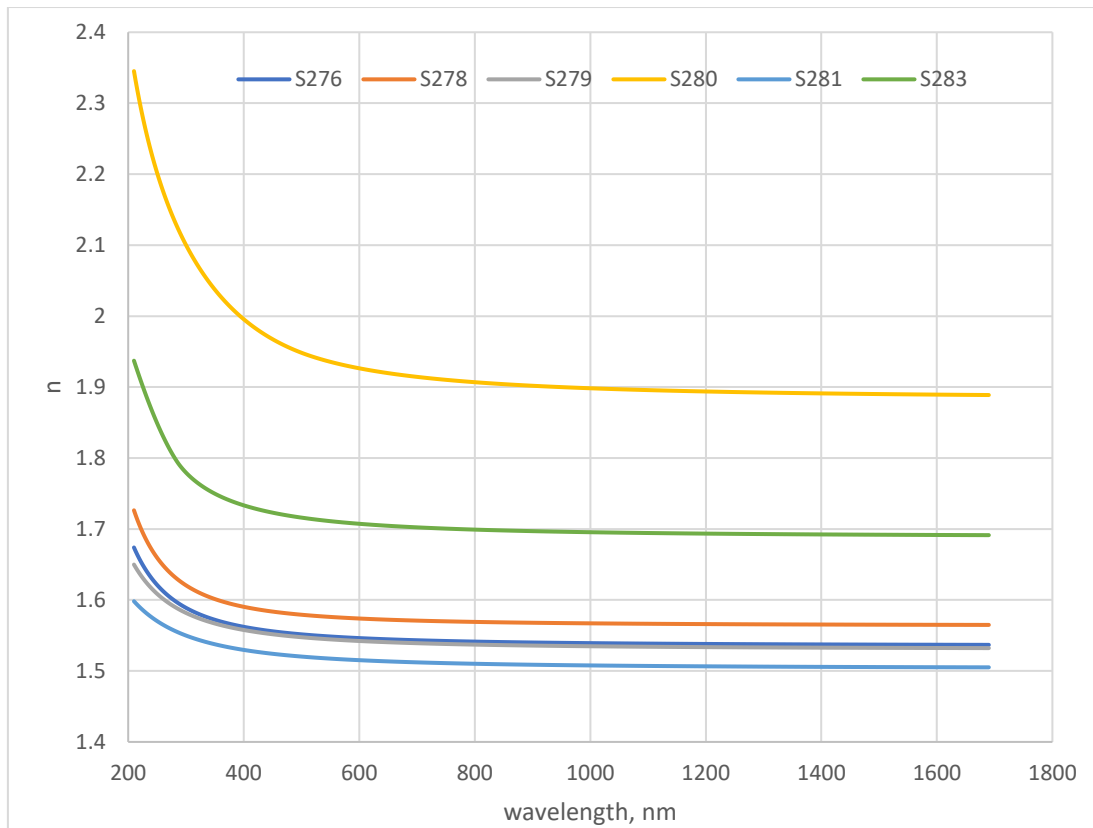
Figure 90.: SiOₓNy/glass ellipsometry measurements.

The refractive index curve (at 550 nm) as a function of the ratio of the partial pressures of oxygen and nitrogen is shown in Figure 91.
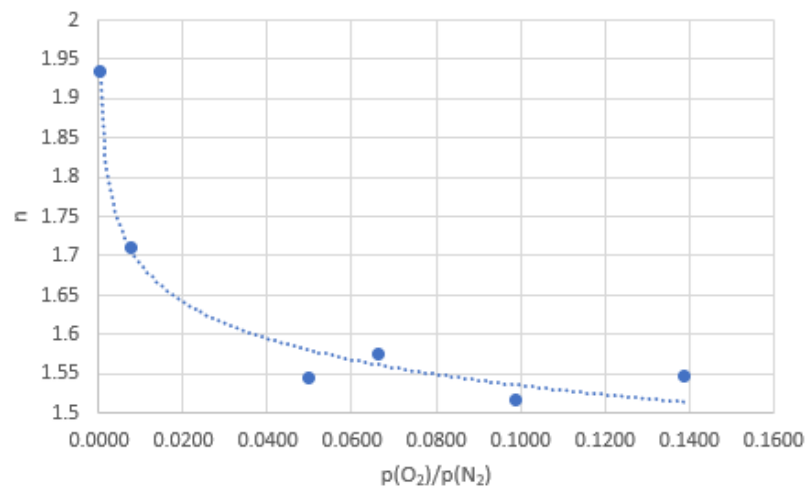
Figure 91.: SiOₓNy film refractive index in dependence from p_{O_2}/p_{N_2}.

SiO$_x$N$_y$/glass samples data are summarized in Table 26.

Table 26.: Summarized data for SiO$_x$N$_y$ on glass samples.

Sample Nr.	p_{N_2}, Torr	p_{O_2}, Torr	Transmittance at 550 nm, %	n at 550 nm
S276	$4.25E-05$	$5.90E-06$	91.7	1.55
S278	$6.80E-05$	$4.50E-06$	91.6	1.58
S279	$1.20E-04$	$6.00E-06$	91.4	1.54
S280	$1.30E-04$	$5.30E-08$	90.6	1.94
S281	$8.30E-05$	$8.20E-06$	92.1	1.52
S283	$1.30E-04$	$9.80E-07$	89.0	1.71

Before proceeding to large scale coating procees, small size diffusers were made in order to prove that these coatings will indeed improve diffuser transmittance and will not create any side effects. 50mmx50mm ITO glass were sputtered with various SiO$_x$N$_y$ and also used for characterization of the coating. Due to the very complicated simulation of glass/ITO/SiO$_x$N$_y$ stack, a piece of soda-lime glass was attached to glass/ITO substrate. Subsequently ellipsometry measurements were carried out on this soda-lime glass piece. In sufficient approximation, it can be assumed that the film obtained on a piece of soda-lime glass has the same composition and optical properties as the film on a glass/ITO substrate. Ellipsometry measurements were taken with spectral ellipsometer Woollam RC2 − XI at incident light angles of 45, 50, 55, 60, 65, 70, 75 and 80 degrees. Calculated functions of the refractive index as a function of the wavelength for all samples are given in Figure 92. It was not possible to obtain SiO$_x$N$_y$ film with n ≈ 1.60 at 550 nm due to technical limitations of SAF 25/50 system.
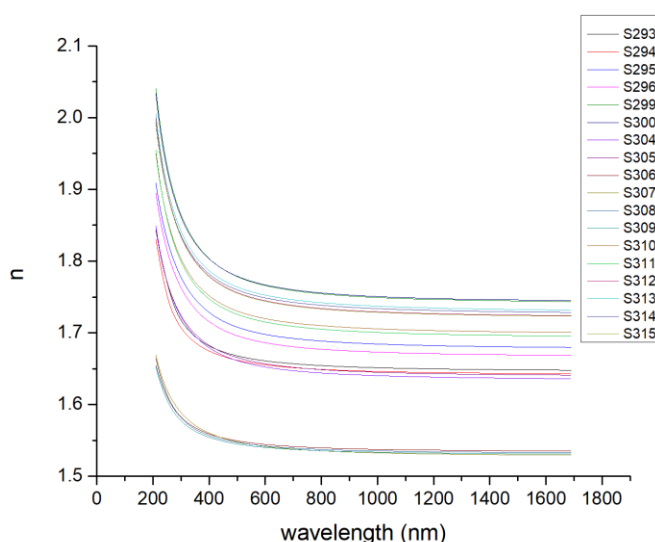
Figure 92.: SiO$_x$N$_y$ films ellipsometry measurements.

Almost linear dependence of the refractive index on the ratio of the partial pressures of oxygen and nitrogen is achieved. This dependence is given in Figure 93.
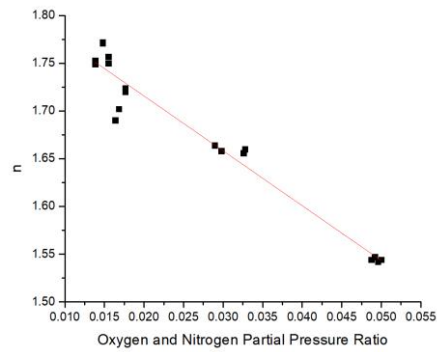
Figure 93.: Refractive index of the SiO_xN_y film depending on p_{O_2}/p_{N_2}.

SiO$_x$N$_y$ films data are summarized in Table 27.

Table 27.: Summarized data for SiO$_x$N$_y$ coating on ITO glass samples.

Sample Nr.	Approximate thickness, nm	p_{O_2}, Torr	p_{N_2}, Torr	n at 550 nm	Average n at 550 nm	XPS data
S293	287	2.75E-06	9.50E-05	1.66	1.66	$SiO_{1.40}N_{0.42}$
S294	273	2.80E-06	9.40E-05	1.66		
S295	246	1.85E-06	1.10E-04	1.70	1.70	$SiO_{1.28}N_{0.51}$
S296	224	1.80E-06	1.10E-04	1.69		
S299	306	1.55E-06	1.05E-04	1.77	1.77	$SiO_{1.08}N_{0.65}$
S300	310	1.55E-06	1.05E-04	1.77		
S304	327	2.90E-06	8.90E-05	1.66	1.66	$SiO_{1.40}N_{0.42}$
S305	329	2.90E-06	8.85E-05	1.66		
S306	327	5.90E-06	1.20E-04	1.55	1.55	$SiO_{1.77}N_{0.21}$
S307	300	6.00E-06	1.20E-04	1.54		
S308	310	5.85E-06	1.20E-04	1.54	1.54	-
S309	324	5.95E-06	1.20E-04	1.54		
S310	291	1.85E-06	1.05E-04	1.72	1.72	$SiO_{1.24}N_{0.57}$
S311	292	1.85E-06	1.05E-04	1.72		
S312	296	1.55E-06	1.00E-04	1.75	1.75	$SiO_{1.14}N_{0.62}$
S313	295	1.55E-06	1.00E-04	1.76		
S314	276	1.45E-06	1.05E-04	1.75	1.75	$SiO_{1.14}N_{0.62}$
S315	269	1.45E-06	1.05E-04	1.75		

XPS measurements were carried out for samples S296, S300, S304, S306, S310 and S314. The dependence of the refractive index on the nitrogen content in the SiO_xN_y film is given in Figure 94. Absolutely linear dependence of the refractive index on the nitrogen content in SiO_xN_y film is achieved.

Equation	y = a + b*x	
Weight	No Weighting	
Residual Sum of Squares	3.86269E-5	
Pearson's r	0.99942	
Adj. R-Square	0.99856	
	Value	Standard Error
Intercept	1.45121	0.00426
n Slope	0.01338	2.27614E-4
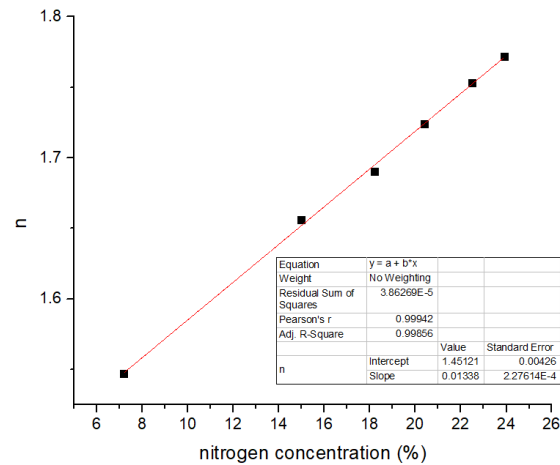
Figure 94.: Refractive index of the SiO_xN_y film depending on the nitrogen content.

Modelling using Optilayer software were done, predicting that n=1.75 would give lowest reflectance, see Figure 95.
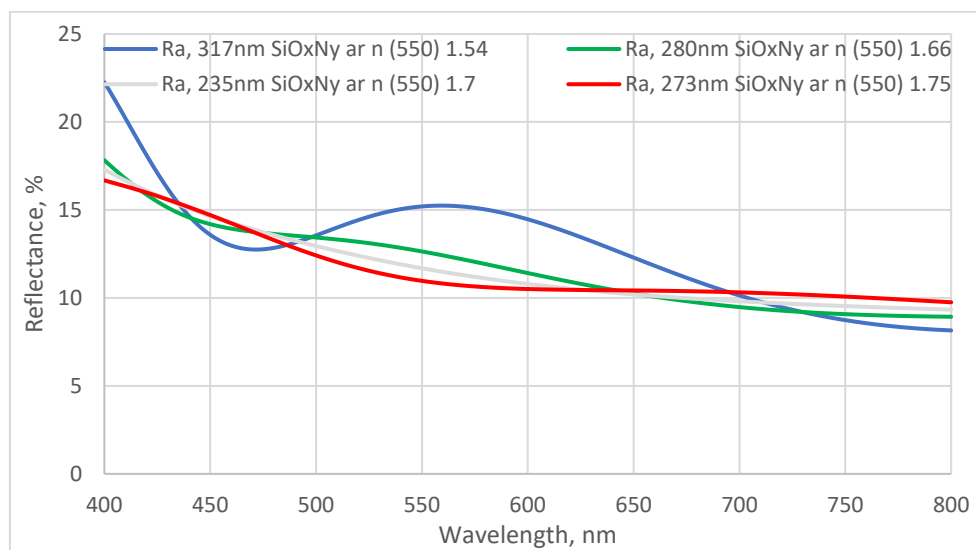
Figure 95.: Optilayer modelling of diffuser reflectance dependence from various SiO_xN_y layers.

Coated samples were assembled into diffusers using specially made glass alignment sheets with openings for the 50mm x 50mm size samples, see Figure 96. 8µm spacers in density 95 pcs/mm^2 were used. All coated samples were cleaned before use with isopropanol.
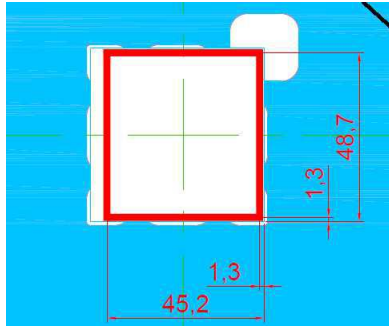
Figure 96.: Glass carrier sheet with sample alignment opening.

During assembly process the BOT alignment sheet was handled as regular 1,1mm glass. In case of the TOP glass sheet the main nuance was that the glass sample was held into the alignment sheets opening using glass attachment fluid so that it would not fall out when it is turned upside down. A small amount of attachment fluid was filled into the alignment sheets opening and then the TOP sample was placed into it. After that TOP and BOT alignment sheets were processed as regular 1.1mm glass sheets.

During assembly process two different attachment fluids were tested – LC material (LC3D2) and vacuum pump oil (Leybonol LVO 100). From these two attachment fluids liquid crystal turned out to be the preferred option because it was easier to clean from surfaces after removing the assembled unit.

During the assembly process there were no major problems that would fail the process. Few minor problems were as follows:

- The alignment sheet did not lay perfectly flat on the assembly table. Due to this some manual alignment was needed and alignment glass had to be held down with palm in order to get it aligned properly which may introduce some contamination that could cause dielectric breakdown;

- There should be a dot on the TOP alignment sheet that indicates where to drip the attachment fluid so that it spreads out evenly otherwise the fluid can get over the sample glass edge and spread to unwanted areas;

For SiO_xN_y reference 196nm SiO_x coated samples were used. Note that because SiO_x coated samples were not deactivated by high temperateture treatment, so after assembly of samples into cells, they have developed active unfilled area defect, see Figure 97.
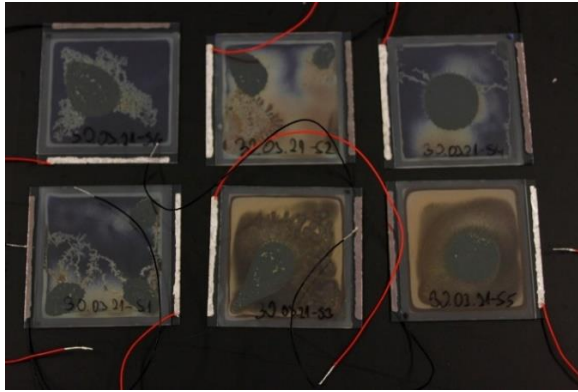
Figure 97.: Empty void defects for SiO$_x$ coated samples.

This defect is identical to large size diffusers where temperature untreated SiO$_x$ coatings are used. There to avoid this defect, most likely due to very active SiO$_x$ surface, coating should be treated 2h at 300 °C. On the contrary, SiO$_x$N$_y$ samples did not had this defect, see Figure 98., so temperature treatment step is not necessary. Some spots with different LC aligment can be observed but none of the void defects.
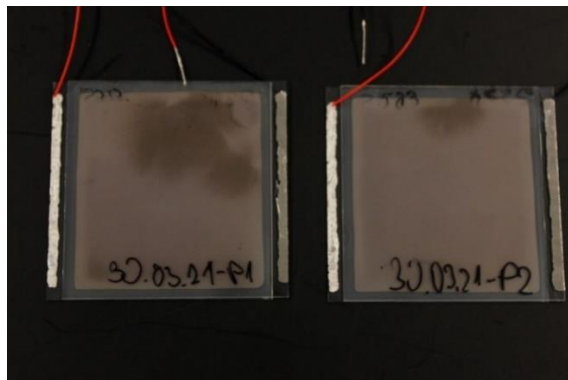
Figure 98.: LCD using SiO$_x$N$_y$ coatings without empty void area defects.

Two assembly batches were done, the first to validate the method with only two samples and SiO$_x$ standard cells for reference benchmarking, followed by the rest coated samples. The time difference between them was 1 week, and this may explain increased breakdown voltage for second batch due to possible particle contamination.

The overview is given in Table 28. From the electro - optical test results, one can see that best open state transmittance is obtained for n=1.66. Note that the raise time is faster due to changed dielectric properties and thinner coating.

Table 28.: E-O results for diffusers with SiO_xN_y coatings.

Coating	n (550 nm)	Film thickness, nm	Normalized open transmission, %	E-O test, %		E-O test (speed), µs	
				Open	Close	Fall	Rise
	1st batch, switching voltage up to 150V						
$SiO_{1.84}$	1.51	196+196	87.8	88.8	12.3	695	1030
$SiO_{1.14}N_{0.62}$	1.75	276+269	88.9	88.8	8.3	735	463
$SiO_{1.40}N_{0.42}$	1.66	287+273	89.4	90.8	8.6	735	463
	2nd batch, switching voltage up to 130V, breakdowns at higher voltages						
$SiO_{1.08}N_{0.65}$	1.77	306+310	-	87.2	8.1	727	1693
$SiO_{1.77}N_{0.21}$	1.55	327+300	-	89.6	8.4	727	1692
$SiO_{1.24}N_{0.57}$	1.72	291+292	-	89.2	8.7	737	1485
$SiO_{1.14}N_{0.62}$	1.75	295+295	-	89.9	8.6	718	1397

Optilayer software predicted n=1.75 to give higher transmittance in open state but in practice we see than n=1.66 is better, see Figure 99.
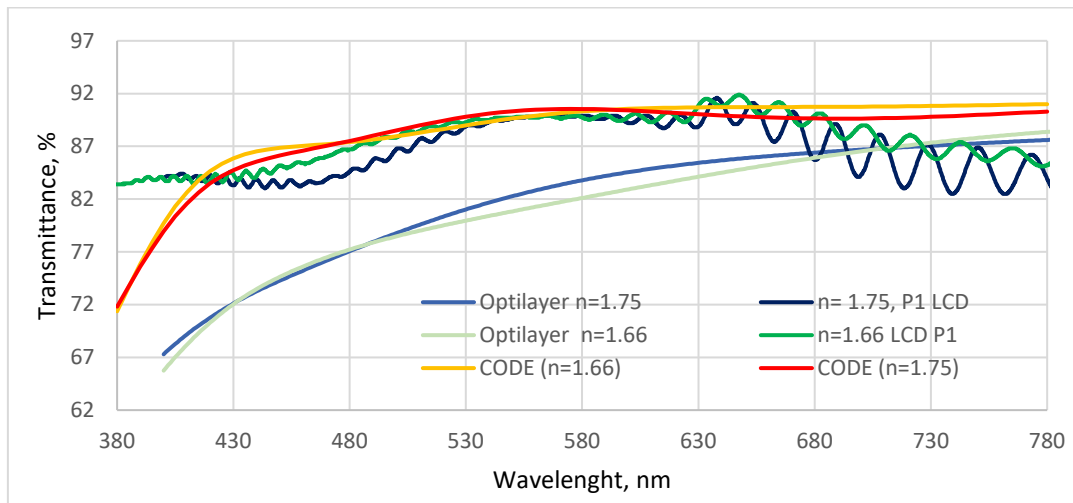
Figure 99.: Transmittance Optilayer and CODE V simulations for SiO$_x$N$_y$ layer combinations vs real results (LCD).

Alternative modelling using CODE V software was also done and its result suggests that n= 1.66 is better that agrees with practical results, so most likely its model is more appropriate as it takes into account k values, that are nonzero for coatings with n above 1.7 at 550 nm, see Figure 100.
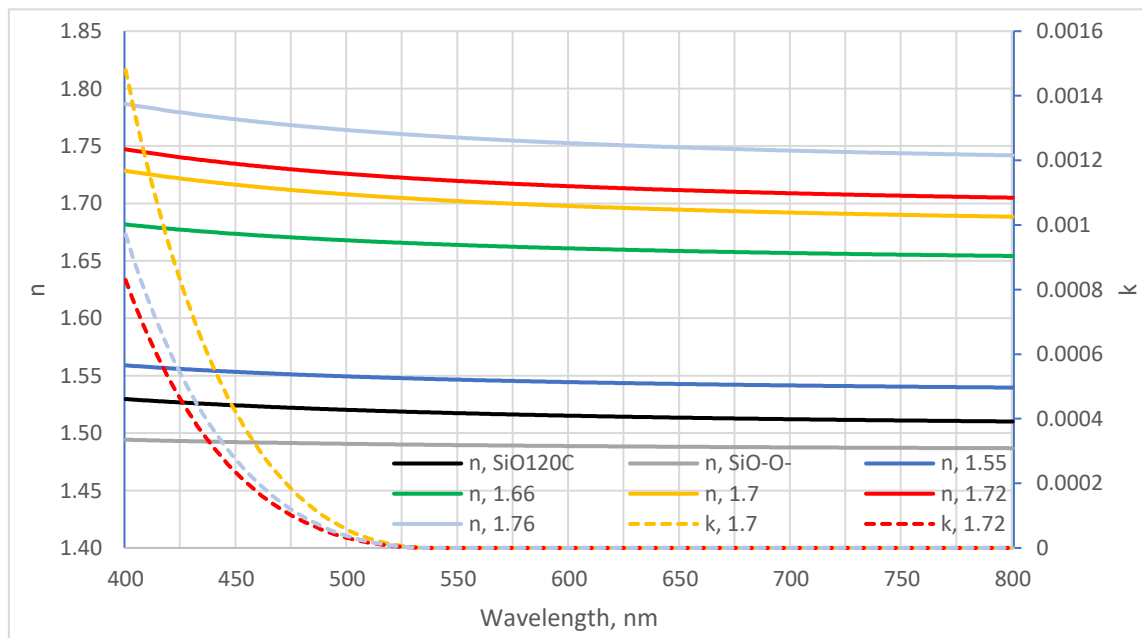
Figure 100.: n, k values of dielectric coatings.

Finding optimum mode by CODE V software predicts n=1.55 and 200nm thickness. Samples were made and while results are better than reference but do not improve previously reached results,

see Table 29. Observed breakdowns at 100-120 V most likely is due to thinner coating thickness and coating quality.

Sample Nr.	Approximate thickness, nm	E-O test Open-close	E-O test, speed Fall-raise	n at 550 nm
P12:S327+S328	187+195	89.1-9.1%	671-735	1.54
P13:S329+S330	193+197	89.4-9.2%	663-862	1.54

Obviously, for stack transmission optimization, coatings up to n = 1.7 at 550 nm should be used as they have k value of zero. 280-290 nm thick SiO$_x$N$_y$ coating with n = 1.66 will give best results for diffuser transmission. Thinner coating will increase risk of dielectric breakdown but in principle, when coating quality is improved, may be used for diffusers.

Coating process was set on larger scale FHR Line2500.H sputtering machine based on SiO$_x$ process settings but adding O$_2$ to N$_2$ process gas. By varying process gas ratio, coatings with different refractive index were achieved with almost liner dependence, see Figure 101.
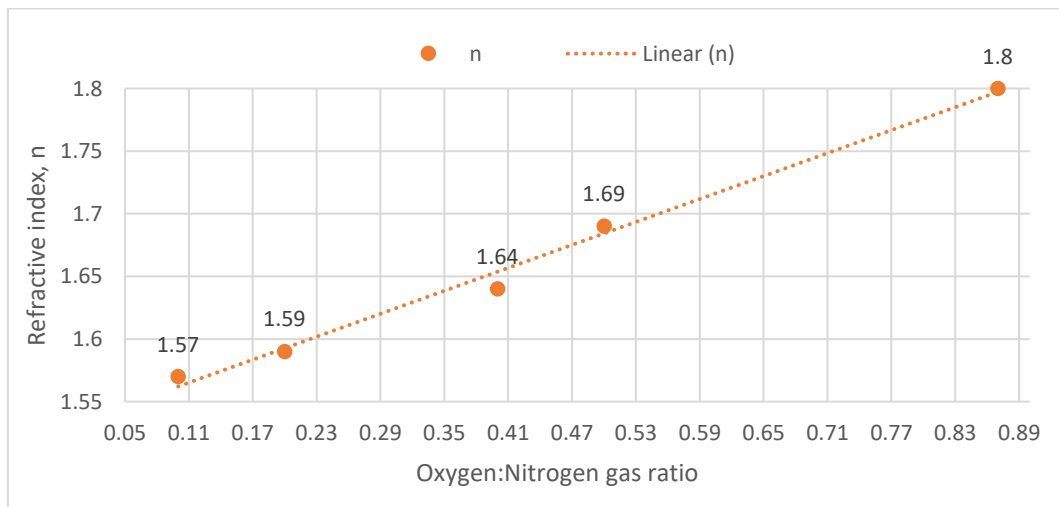
Figure 101.: Refractive index (at 550nm) dependence on process gas oxygen: nitrogen ratio in FHR machine. Higher ratio corresponds to more nitrogen.

Oxygen:nitrogen ratio of 0.87 yielded sample with noticeable less transmittance in visual spectra due to incomplete reactive sputtering process. Other samples had good transparency and only for coating at 0.4 ratio, k values were larger than 0. For diffusers, coating properties can be tuned with oxygen:nitrogen ratio in reactive sputtering, the preference given for 0.5 oxygen:nitrogen ratio (if ITO layer have refractive index closer to 2) or 0.2 (if high temperature deposited ITO with refractive index

1.8 is used). The overview of n-k dispersion is given in Figure 102., showing that refractive index dispersion is larger for industrial machine.
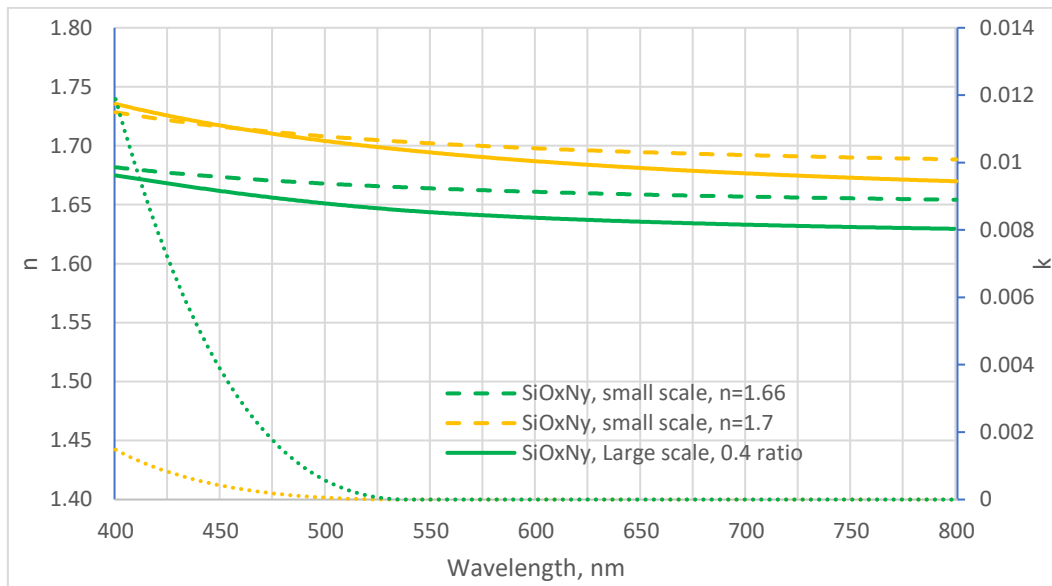
Figure 102.: Comparison between n-k dispersion of films coated industrial machine (solid) and pilot scale (dashed) machine.

As coating with various n is available now, Sci-Soft Film Wizard, Optilayer and COMSOL software models of diffuser were used for more precise estimation of the BBAR layer effect under conductive ITO layer. Figure 103. shows that the lowest reflections can be obtained by using 75 nm SiO_xN_y layer with n= 1.71 (S283) for 30nm ITO layer.
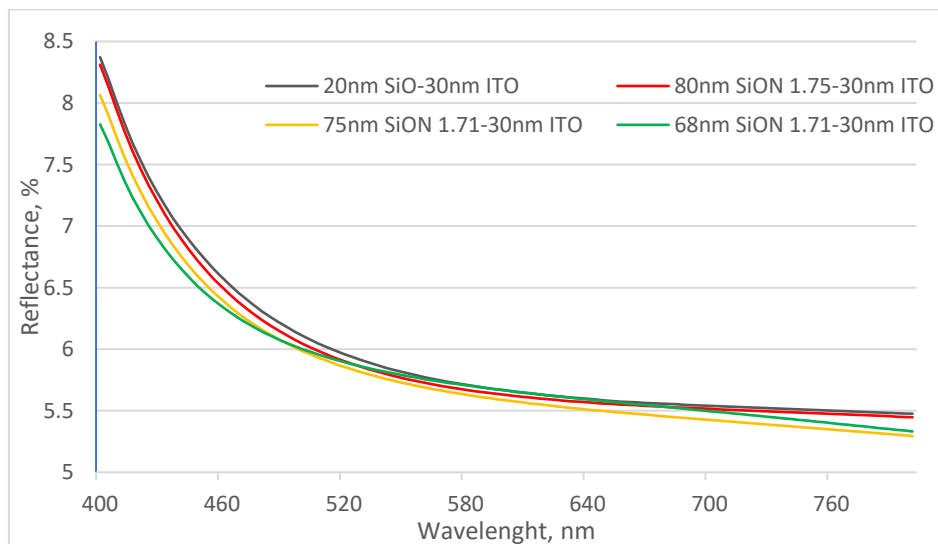
Figure 103.: COMSOL model results for various layers between 30nm ITO and glass.

Models suggest that the best layer thickness for this material is 68 nm, see Figure 103. However, the reduction of reflection is not very large – 0.2-0.4 % for high temperature process ITO layer which is only 30 nm thin.

The situation could be different when low temperature ITO is used in thickness of 120 nm and then, the BBAR layer of 68- 80 nm of n= 1.75 SiO_xN_y would be mandatory, see Figure 104.
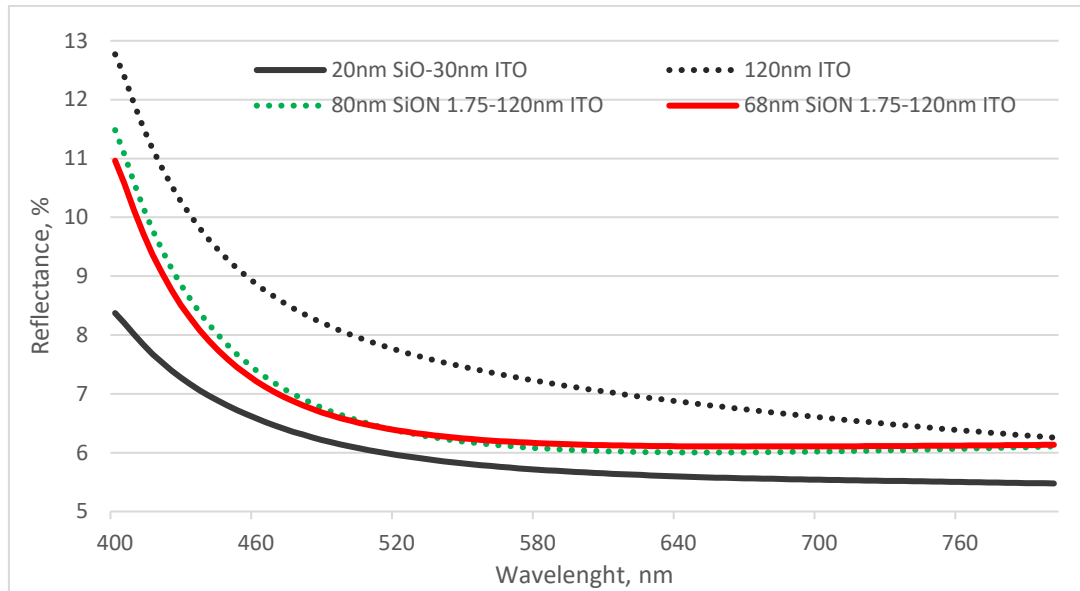
Figure 104.: COMSOL model results for antireflective layer under 120nm ITO glass. Reflectance of 30nm ITO is lower.

4.4 Conclusions

1. Normalized transmittance of single diffuser was improved from 87.0 % to 89.4 %, that is higher than planned 88.0 % by using refractive index matching.

2. SiO_xN_y coating was used for index matching dielectric layers due to following advantages:

- It is single coating not like traditionally used SiO_2 and PI combination in LCD industry, easier to make;

- It's refractive index is closer to ITO refractive index;

- Refractive index can be easily adjusted by varying oxygen: nitrogen ratio during sputter process;

- Less defects are observed as its surface is less active to than sputtered SiO_x. Most likely due to less dangling Si-O bonds;

- Can be used as barrier and BBAR layer under low temperature process ITO layer.

3. Several software tools were evaluated for modeling and simulation of diffuser and coating stack transmission and reflectance. CODE V and Optilayer gave most precise results. Alternatively, COMSOL Multiphysics model can also be used, for example in antireflective coating design.

5. Single diffuser and multifocal diffuser (optical chip) build up

5.1 Literature review

One can find many generalized information regarding production technology of flat panel displays. The key aspects related to micro-diffuser production are briefly reviewed below. Figure 105. provides schematic overview of the processes.
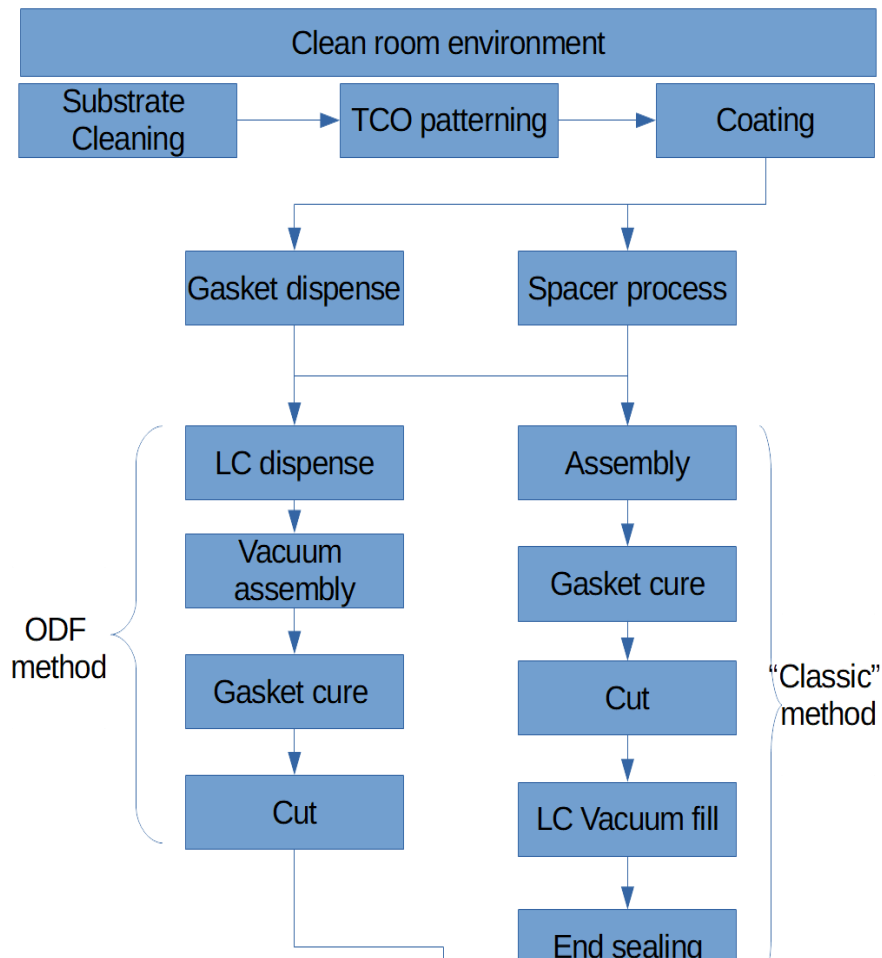
Figure 105.: Schematic presentation of production processes.

All operations depend on environment and the requirements are set from cell gap and resolution (feature size). Any particle that is visible or conductive must be avoided. Typical passive matrix production needs at least ISO class 7 for general environment as one class higher local work place can be achieved with HEPA equipped fans in each equipment [72]]. The required cleanroom environment can be lower for back-end processes, like cutting, testing etc., where LCD cell is already sealed. Micro-displays have more strict requirements since they are used under magnification. A 200x

magnification will require class 2 as particles below 5 microns will be visible [73]. This is almost like high-end active-matrix LCD production environment.

Besides the environment, all materials should be clean, in particular attention is given to substrate cleaning as it is main base material. Glass or ITO coated glass is typically washed with highly pure deionized water with the help of appropriate detergent. During this process, not only particles but surface contaminants are removed, ensuring that they are not interfering with next processes. In the late 1990's, in an emerging field of coatings that made glass harder to stain and easier to clean, a few competitors started using Contact Angle measured in degrees to compare the water repellence of these coatings. This was because one of the main characteristics of these coatings is that they are all water-repellent or hydrophobic. Since then, this technique has become one of the most used surface cleanliness characteristics techniques. It takes advantage of the fact that most contaminants cause water to bead up due to their hydrophobic nature. The main disadvantages for this application are that it is a direct "one point" measurement technique, to inspect large surface areas a measurement series must be made[74]. Contact angle measurement is a simple, useful and sensitive tool for quantifying the wettability and the surface energy of different materials in contact with pure water and/or aqueous surfactant solutions [75]. Modern equipment allows not only to measure water and aqueous surfactant solutions (for example, diiodomethane), but also calculate surface free energy easily [76].

Every display, large or micro begins with base material, glass or, in specific cases, inorganic or organic film. It serves as containment boundaries for display and as basis for functional coatings. The best review on glass as material can be found in 3rd edition of Fundamentals of Inorganic Glasses book [77]. We will look on properties that have direct influence on our work – chemical, mechanical and optical.

Chemical properties are important as the liquid crystal performance is very sensitive to ion contamination [78] even if there are no thin film transistor structures. Moreover, glass performance is affected as well by chemical composition, for example in glass corrosion process [79].

Small size displays, called micro-displays, are produced either on quartz (transflexive type) or silicon wafer (reflective type). Quartz substrates are chosen for those displays that are placed close to high power light sources, like projectors. Silicon wafers were used for micro displays as it is convenient to produce small thin film transistor structures with standard semiconductor equipment. None of materials have any issues with metal ion leaks or chemical properties, as the chemical composition is nearly 100% SiO_2 with traces of other metals or oxides [73], [79]. While fused silica has better properties, it is not used for larger display production. The material is not cheap and price increases with size exponentially. One of best, largest fused silica products is industrially available from Corning

in 300mm diameter [80]. The minimum size for available display production line, called Gen 1, is 300x400mm [72], effectively narrowing our choice to soda lime or borosilicate glass.

Soda lime glass has been used for quite long period, as the first displays were made from readily available materials at that time. First glass sheets suffered from spot inclusions and increased sodium leak during processing, notably photolithographic process. As a rule, SiO_2 barrier layer was sputtered first before coating conductive materials. Now with very mature display glass production technology, it becomes less and less common. Soda lime glass is the choice for passive matrix displays, as most convenient and economic material, and typically includes barrier layer [81].

Alkaline earth boro-aluminosilicate glass usage started with advent of thin film transistor (TFT) displays partly due to lack of any sodium leak into liquid crystal layer, see Table 30. As technology progressed to larger TFT display panels in size and with smaller transistor structures, requirements for precision increased. Typical soda lime glass has 8.40×10^{-6}/°C (0 to 300 °C) thermal expansion coefficient but for alkaline earth boro-aluminosilicate 3.17×10^{-6}/°C [31]. Therefore, borosilicate glass is now the common material for TFT [81]. It is 10-20% more expensive than soda lime.

Table 30.: Chemical composition of soda lime and borosilicate glass.

	Sodalime	Borosilicate
Silicon oxide	70 % - 73 %	65 % - 78 %
Aluminum oxide	0.5 % - 1.9 %	13 %- 18 %
Strontium oxide	0 %	0.2%—8 %
Barium oxide	0 %	0.2%—10 %
Calcium oxide	0 %	3 %—12 %
Zinc oxide	0 %	0—2 %
Magnesium oxide	1.0 % - 4.5 %	0 % - 2 %
Sodium and potassium oxides	13 % - 15 %	0 %
Sulfur oxide	0 % - 0.3 %	0 %
Iron oxide	0.08 % - 0.14 %	0 %
Boron oxide	0 %	7 % - 12 %

Glass surface is not inert. It reacts with water (humidity) at temperatures from 600 °C to room temperature. Hydroxyl (OH-) groups formed on surface and in the body, are very reactive and important to note for coating processes, see Figure 106. Chemisorbed water cannot be removed with simple heating, temperatures over 400 °C are required. It is also affected by glass roughness, i.g.

surface mechanical properties. Deionized water used in glass cleaning steps can attack the glass surface and increase its roughness [81].
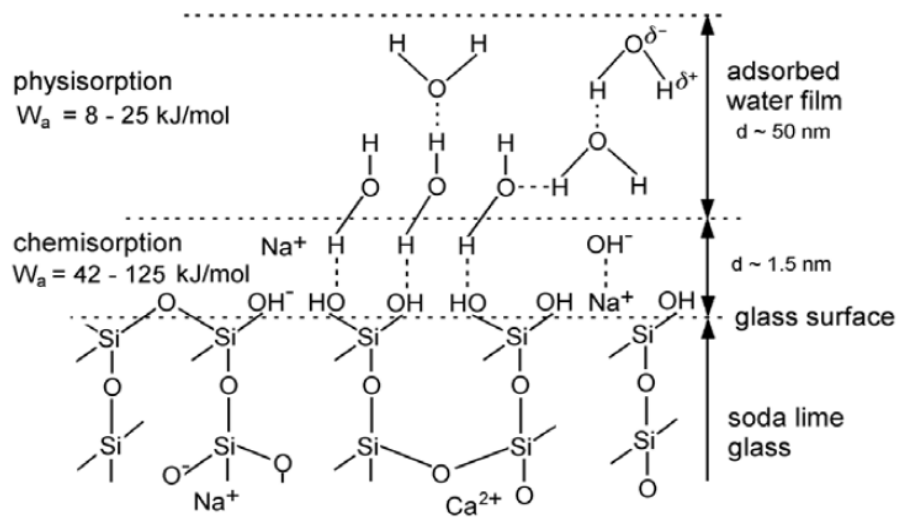
Figure 106.: Diagram of flat surface with terminal hydroxyl groups and absorbed water [81].

Mechanical properties are important as there is handling and process requirements [72], as well as surface geometry which, in turn influences optical properties, see Table 31.

Table 31.: Comparison of glass and fused silica mechanical properties.

	Glass	Fused silica
Young's Modulus:	70 GPa	73 GPa
Poisson Ration	0.2	0.16
Density	2.5 g/cm3	2.2 g/cm3
Shear Modulus	29 GPa	31 GPa
Surface roughness	4-10 nm	<2 nm

Glass is elastic material and under gravity sheet of glass will sag in the middle. The thinner the glass is, the bigger the sag. For example, 400x300 mm glass supported at 300 mm sides, will sag: 1.1 mm thick only 1 mm but 0.55 mm thick 4 mm. This limits the handling and processability in form of glass sheets [82]. As we are looking for thinner substrates, 0.4 mm glass is the thinnest that can be handled in Gen 1 line by conveyors and robot arms. 0.33 mm can be handled manually by sliding and moving on carrier between process steps. Any thinner material is processed like film with roll-to-roll technique or temporally bonded to thicker glass carrier [83]. However, there bonding materials

impose process temperature restriction [84]. Another principal approach is to use slimming of assembled displays.

Glass has curvature, waviness and toughness that impact any display construction, see Figure 107.
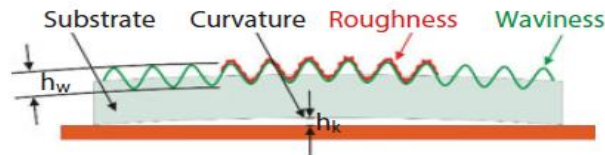
Figure 107.: Glass surface properties.

Warp is a large surface irregularity, any deviation from a true plane. This is any twisting or raising of any portion of the glass sheet from a flat inspection surface. Supplier quality control ensures that supplied substrates pass the criteria but any later coating of thin films can change its value. Warped glass will lead to uncontrollable cell gap even there are counter methods [85]. Micro-corrugation is measured on the tin face in a direction perpendicular to the pull of the glass production line. Glass for simple passive matrix displays do not require low micro-corrugation values, see Table 32. Their size is small so any light interference from micro-corrugation cannot be observed. This, however becomes evident as sizes are becoming larger. If needed, one can polish the tin face of glass to improve the micro-corrugation [17].

Table 32.: Micro-corrugation values for different glass class [86]

Substrate thickness	TN glass substrate (µm/20 mm)	STN glass substrate (µm/20 mm)	Fused silica substrate (µm/20 mm)
1.1 mm	wfpd≦0.15	wfpd≦0.05	
0.55 mm	wfpd≦0.25	wfpd≦0.10	
0.4 mm	wfpd≦0.30	wfpd≦0.15	
0.3 mm	Not produced		wfpd≦0.002

For high end displays, fusion drawn technology for thin glass forming is preferably used. Contrary to classical tin bath process, this creates glass sheets that do not need polishing to reduce micro-corrugation. Besides this, both sides of glass sheet have identical surfaces form chemical point of view [77].

The primary aspect for selecting glass is its transparency. Quartz due to higher refraction index, reflects 6.7 % from two surfaces exposed to air. Glass, in general, reflects about 8 %. If we look at glass extinction coefficient values and glass thickness, their influence is small. The main transmission

loss occurs due to reflections on surfaces [77]. Thus, specification for higher transparency is achieved by antireflective layers on air surfaces, with most common being 4-layer combination [64], [79].

Last but not least, there are also surface defects [81]. Their number is dependent on inspection magnification. For example, typical passive matrix display (TN) quality specification will allow 40 µm spot on glass, as it is barely visible with naked eye. 15x-50x magnification used in micro-display projection systems will be make it detectable and can led to defective display gradation [87]. As the fused silica sizes are smaller, it is possible to achieve strict requirements to surface quality. Most common defects are [86]:

Bubbles. A bulk bubble is a gaseous inclusion more or less circular depending on the thickness of the glass. It deforms the image in transmission or reflection.

Stones. Solid inclusion (unmolten material).

Seeds. A term used to denote a gaseous inclusion having an extremely small diameter in the glass.

Cords. Fine lines with different transmission in the glass. It is glass of different glass composition due to non-homogeneity.

Adhering surface chips. Glass particles sticked on the glass surface. Notably their number is higher if glass is cut, grinded and not immediately cleaned. Glass chips after time becomes very troublesome to remove.

Scratches. Damage on the glass surface appearing in lines.

Tin speck. A tin inclusion. It deforms the image in transmission or reflection.

The next process after initial cleaning, is conductive layer patterning. Traditionally it is done by series of process steps, masking necessary ITO areas by photolithography method and etching away the rest. Alternative, which is also used in this work, is to use high power laser to ablate away unnecessary ITO [88]. It is quite convenient and fast if division into conductive regions is needed but not suitable for removing large areas due to long processing time.

After patterning of conductive layer, dielectric and alignment coatings are typically deposited by wet coating methods. For example, polyimide precursor is flexo-printed on substrate. High temperature imidization reaction is done in oven and if particular LC planar orientation direction is needed, then the surface is rubbed by velvet cloth. Rubbing process not only provide microgrooves but in addition surface polymerization reactions occur [89].

Wet coating has its drawbacks. First, it is limited to available coating formulations with certain refractive index and dielectric properties, limiting overall stack design. Second, wet coating layer is dried in the process and isolated pinholes are formed that leads to dielectric breakdown of LC at high electric fields. Multiple layers help to reduce this possibility but yet another alternative is to use

physical vapor deposition for coatings. This method provides good results but is limited to inorganic materials [54].

Then the process flow is divided for top and bottom substrates. On top substrate spacers are deposited by wet or dry process [72]. Wet process involves suspending spacer particles into evaporable solvent and spraying into hot chamber over substrate. Dry spacer technique uses electrostatic field to separate spacers during spray and attracting them on to substrate. Dry method is avoided for static electricity sensitive substrates but preferred for adhesive spacers. Adhesive spacers have adhesive coating that might start to melt during wet process spray leading to spacer clusters that is considered as defect. In case if support structures (photo spacers) are used, it is done by typical photolithography process .

On bottom substrate gasket can be screen-printed or dispensed depending on gasket material viscosity or gasket total length on substrate. If there are multiple cells with long total length of the gasket, dispensing becomes too long for practical means so screen print is preferred. Dispensing is more convenient process, however gasket line start, stop and turns must be carefully optimized to ensure uniform quality [90]. In the case of micro-displays, thinner gasket is preferred to keep overall size small.

Historically first method for LCD cell assembly was to assemble top and bottom substrates in atmosphere, cure gasket and then fill LC inside the cells. The fill process starts by vacuuming the cells through hole in the gasket and adding LC to it afterwards, thus called vacuum capillary fill (VCF) method. Due to narrow cell gap, LC first enters the cell under capillary forces and then under force of atmospheric pressure. Cell gap is not perfect, it is typically overfilled. Cell is then pressed to squeeze out excess of LC and sealed. Method works well for certain sizes, as for large sizes it takes too long time to fill while LC mixture evaporates. To overcome this limitation, "one drop method" (ODF) was invented, so one or many drops of LC were placed inside closed gasket and both substrates were assembled in vacuum. The cell gap accuracy in this case depends on dispensing accuracy but method allowed display production above 21-inch sizes [91]. This is also convenient method for smaller displays as handling operations are reduced.

After assembly cell is cut out from "mother" panel by either mechanical scribing or by laser. Majority of displays is still cut, breached out from mother glass and edge polished. With advances in laser field, laser scribing gives better quality (fewer lateral cracks from cutting wheel pressure" and becomes more common and available [92] for advanced forms.

Contact attachment to ITO surface can be done by means of conductive particles mixed in UV or thermo curable adhesive or chemically soldered to the surface using ultrasonic solder equipment [93].

Gap between two dielectric layers with electric field must be precisely controlled as its thickness determines electro - optical properties, typically in the range of 2 to 50 micron. As it will be filled with liquid crystal layer, which as liquid is not compressible and can provide cell gap control by itself, anyway, for cell construction certain means of cell gap control are needed [72]. This is achieved by depositing spacers or making support structures by photolithographic means. Spacers can be placed outside active area (mixed in gasket material and then dispensed) and on active area by spray, see Figure 108.
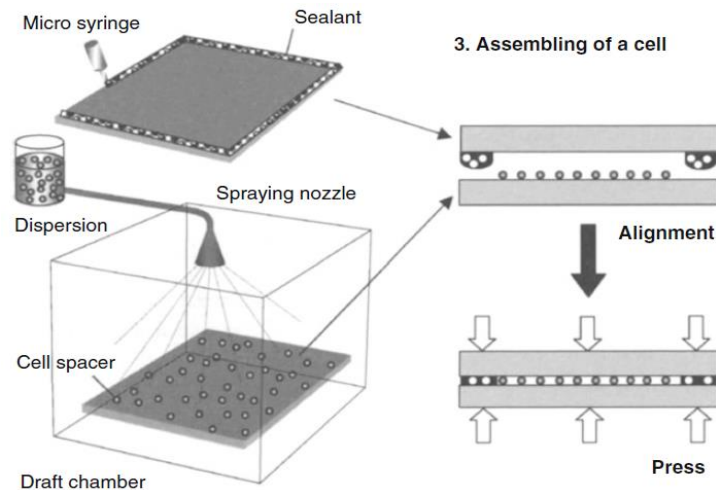
Figure 108.: Schematic illustration of spacer process for display assembly in vacuum capillary method [94]

Spacers can be made from glass or polymer (radical polymerization of styrene and divinylbenzene). Both are inert to LC but polymer is preferred because their thermal expansion is similar to that of liquid crystal, and is compressible. Cylindrical shapes are best for gap control but are rarely used as they can scratch the layer surface. Depending on LCD application one can have black or white spacers with certain diameter distribution. Spacers can be supplied in form of adhesive spacers, when adhesive layer after spray deposition is melt and thereby fixes the spacer on one substrate. This helps to avoid spacer loss during substrate handling, and having unevenly spaced cell gaps during LCD use [95]. Note that, spacers are not birefringent and typically have refractive index of 1.46. Depending on pixel size, spacer takes away affective active area, resulting in light loss or visible artifact (depending on magnification). This becomes very important for micro displays where spacer can block half of pixel. Thus, to improve efficiency spacers should be absent or kept at minimum only to ensure mechanical support during manufacturing or use [72]. During ODF process, top and bottom glasses are joined in vacuum by 78 N force, see Figure 109. This is enough to press the gasket with mixed spacers to designed cell gap. The substrate above display active area at this moment rests on spacers. Small unfilled gap is present as 95±2 % of LC fill ratio is used as gap limiting factor.

<div align="center">a)   b)   c)</div>
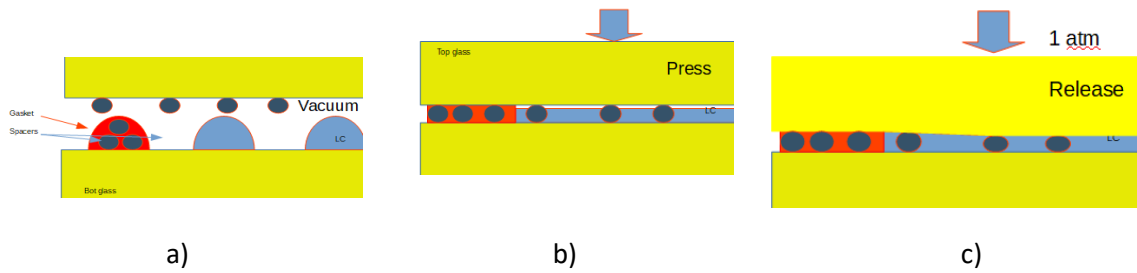
Figure 109.: ODF process, a) -before assembly, b)- during press, c)- after restoring atmospheric pressure.

LC fill ratio typically is selected below 100% to avoid gravity defects caused by excessive amount of LC and manifest during using higher temperatures and long driving of the display. Cold bubble effects in the corners are much easier to detect during production, so fill is stepwise increased till this defect is not observed any more, see Figure 110.
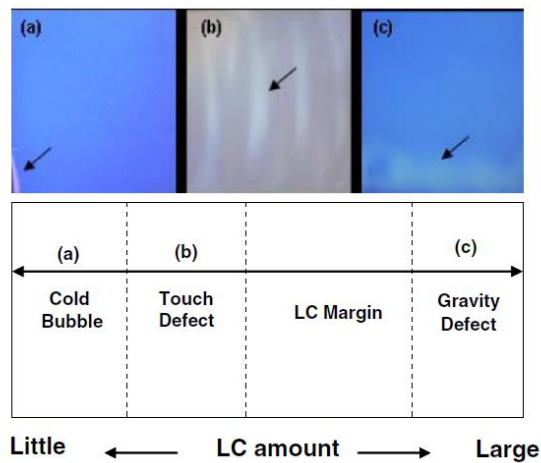
Figure 110.: LC fill defects a) bubble, b) touch, c) gravity and connection with LC filled volume [96]

Alternatively, if classic liquid crystal vacuum filling is used, spacers must be present, that during end seal process, exact cell gap can be adjusted by pressing LCD sides, see Figure 111. Spacers elastically deform to precalculated size and ensure constant gap within display series [97].
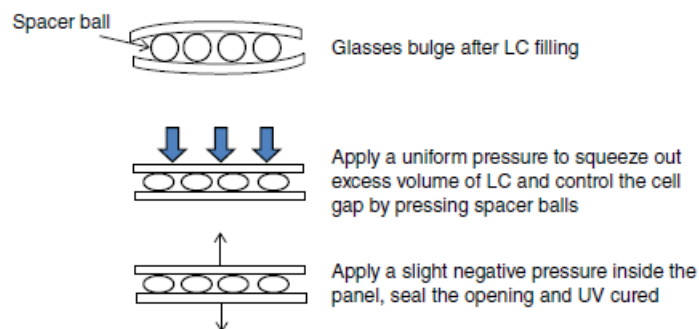
Figure 111.: Schematic illustration of the end seal process [97]

Spacer density depends on required cell gap, accuracy and LCD type. The most common density values are 10 to 200 spacers per mm². One method [98] is to calculate the spacer density based on their compressibility. For one spacer sphere deformation force is given by:

$$F = \frac{\sqrt{2}}{3} X^{\frac{2}{3}} K \sqrt{r}$$

(12.)

where X is the effective diameter reduction, K is compressibility modulus, r- radius of the sphere. Given the manufacturers K value, one can calculate F and from compression load calculate necessary amount of spacer spheres. In general, it is recommended to compress at least 5% that when liquid crystal volume expands at elevated temperatures, spacers stay fixed.

If the display is intended to be flexible and/or subjected to touch force, the necessary distance between placed spacers (spacer/support density) can be calculated [99] due to deformation forces, see Figure 112. Two main conditions are:
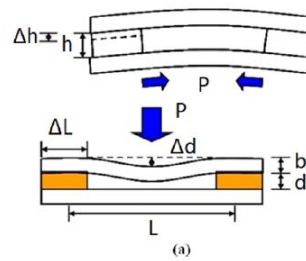
Figure 112.: Schematic illustration of deformation forces during bow and press [99]

a) the relative compression of the spacers caused by external pressure on the first plate must not exceed a given value:

$$\frac{\Delta h}{h} = \left(\frac{P}{\pi s E_s}\right)^{\frac{1}{2}} \leq \frac{\Delta h}{h} max$$

(13.)

where h is the height of the spacers, Δh is the change in the spacer height, P is the external pressure on the first plate of the cell, E_s is the modulus of elasticity of the spacers, and s is the degree of surface coverage of the spacers on the first plate.

b) the maximum deflection of the afore mentioned first plate between the spacers must lie within the same limit.

$$\frac{\Delta d}{d} = \frac{PL^3}{4E_p b^3 d} \leq \frac{\Delta h}{h} max$$

(14.)

where d is the thickness of the LC layer, Δd is the maximum deflection of a plate, L is the mutual spacing of the spacers, E_p is the modulus of elasticity of the plate, and b is the thickness of the plate. For micro-displays due to their small size there is possibility for "spacerless" approach, so the gap uniformity is ensured by either gasket or precise amount of liquid crystal inside the cell. The

disadvantage of this "spacerless" method is that the uniformity of the cell gap depends on the flatness of the substrates [100], [101] and LC dispensing accuracy.

Spacers in the gasket must ensure the full load on display will be ensured. This can be calculated from data and formula provided by supplier [95]:

$$P = 38.4D^{1.75}, \tag{15.}$$

where P is the maximum load in kg for single spacer and D is spacer diameter in mm.

Spacer distribution uniformity requirement is dependent on LCD type, for example STN type will require 4.2±0.1 of gap accuracy. The requirement for diffuser type LCD is less, a 10% accuracy will be sufficient.

There is one constant force – atmospheric pressure on LCD and one dynamic force-electrostatic force between opposite charged sides. For typical LCD types, the last force is negligibly small, explaining that there is little or no research on this subject [102].

In order to reach higher resolutions in TFT LCD, randomly sprayed spacers are replaced by support pillars above the transistor part that is not transparent. Photopatterned spacer pillars have advantage – their size and density as well as shape can be precisely controlled. Yet another advantage is that spacers are not movable during ODF process. The only issues are placement as human eye can notice regular patterns and alignment disruption in vicinity of pillar structure [84]. Support structures in form of pillars, pixel walls most commonly are made from photoresists [31]. As we previously reported, SU-8 can be screen printed and photo-lithographically processed to form such structures [103].

After single diffusers are made and tested, they must be assembled together by means of optical bonding. Optical bonding is bonding of two or more optical components, typically glass, together using a clear optical index matched adhesive. Most often, optical bonding eliminates the air gap between the cover glass and display, thus eliminating two reflective surfaces. This process and adhesive materials applicable are very well studied [104]. In this work, optical bonding is used to eliminate air gaps between individual displays in the stack, in order to increase total set transmission. It is engineering task, to select appropriate material and technology. Two main technologies used for adhesive optical bonding are liquid bonding and dry bonding. In liquid bonding many types of chemicals such as silicones, epoxies, polyurethanes and thermoplastics are used. The liquid lamination method typically involves assembly of the components before cure as well as dispensing and curing of the adhesive. In the case of dry bonding the material typically exists in fully cross-linked state for assembly such as pressure sensitive optically clear adhesives (OCAs). Dry bonding offers several advantages: it is clean, fast and relatively defect free process. However, it requires precisely pre-cut film and vacuum machine for its affixing to display, as well as autoclave to remove any air bubbles [105]. Moreover, the layer introduces 0.5 % haze at least, as well as 0.6 % is lost in transmittance [106].

Liquid optical bonding technology despite of its many weaknesses, it is still the most widely used optical bonding technology because it offers lower cost of ownership. Several technologies exist for adhesive application: damm-and-fill, patterned dispensing, slit-coating, screen-printing, damm-and-injecting. Depending on application, one of the methods can be selected [107].

Materials are a two-part thermal cured chemistry or one-part radiation cured. In the case of a two-part system the materials must be mixed thoroughly and de-aired. In addition, care must be taken such that all air and gas, generated due to mixing or chemical interactions, are removed. Furthermore, proper dispensing is a must such that air entrapment does not take place. In general lamination processes using liquid adhesives is labour intensive with long cycle times. Radiation curing can also be limited due to light blocking masks and uniformity of cure affecting display performance over temperature. A considerable shrinkage may take place during the curing of 2-part chemicals which could lead to warp and separation. In addition, many liquid adhesives, especially silicones require a primer application to achieve adequate adhesion to many low surface energy substrates. Furthermore, clean-up of display and tooling are essential after lamination. This can significantly increase the cycle time, equipment cost, material and solvent cost, and can also lead to further yield loss [108].

There are various sources that induce stresses in an optical assembly. Mechanical loads acting on the optical assembly during operation can generate stress or uniform temperature changes can induce mechanical stress in an optical assembly due to mismatch in CTE between the bonded elements and mounting materials. It is also seen that pressure, inertia, and vibratory loads, internal distortion of the adhesive during cure, and residual stresses due to manufacturing and fabrication processes can develop stress in an optical system. General recommendation is to avoid stress birefringence is by reducing the CTE mismatch between the substrates and the mounting material [109].

Many adhesives are formulated with solvents that evaporate during cure and produce high levels of contaminants. These volatile ingredients are emitted during curing or when the bonded assembly is exposed to vacuum or elevated temperatures. These emitted ingredients in turn may condense as contaminating films on nearby surfaces, such as optics or opto-mechanical assemblies. This causes dimensional instability and changes in material properties, such as micro roughness. This subsequently changes the absorption and scattering characteristics. It is seen that the problem is further aggravated by other factors such as UV exposure, thermal cycling. Also, the deposited contaminants, when illuminated with high power optical beams, give rise to local heating due to optical absorption. The heating can deform the optical figure or induce a thermal-lensing effect from

the coupling of thermal dependence of the refractive index to temperature gradients in the affected optics. Total mass loss (TML) and collected volatile condensable material (CVCM) are two measures of outgassing [110].

Shrinkage during cure and uneven bond layer contributes to movement of the assembly and, in turn, influences assembly alignment accuracies. When high temperature is used for curing, complex process takes place. First, adhesive expands and excess material is squeezed out in x, y axis, or substrates move apart if they are not constrained. As curing starts, volume shrinks, and material is backfilled till gelation takes place. Gelation happens at 30-40 % of cure process and then material flow is prevented. All further stress happens now in z-axis direction. Final cooling step adds up stress in z-direction [111]. Low shrinkage adhesives are more suitable for precision application and are shown to maintain excellent alignment during and post cure without complicated fixturing. UV curable adhesives can bond within seconds at room temperature and are suitable for applications where alignment is critical. Also, an adhesive must be in fluid form with low viscosity so that it wets the substrates completely, leaving no voids in case of rough surfaces. Rigid-to-rigid lamination is known to have problem of entrapped air due surface variations. Pennington from 3M company suggested to use primarily deposited contact patch, so that wetting starts from contact point and propagates to the rest of display. This is confirmed method to reduce air entrapment [110]. Lowering the modulus of elasticity of adhesive materials is also option for process improvement [111].

Optical bonding methods that offer strain relief can reduce detrimental effects. Optical gels can be used in this case because their compliance can respond to stress preventing build-up of stresses in adjacent optical parts. They cannot assure high dimensional stability but they are becoming more and more popular [109].

5.2 Material specification and modelling

Recall specifications related for this chapter, see Table 33. Micro-diffusers due to small physical dimension size, see Figure 113., can be more difficult to make.
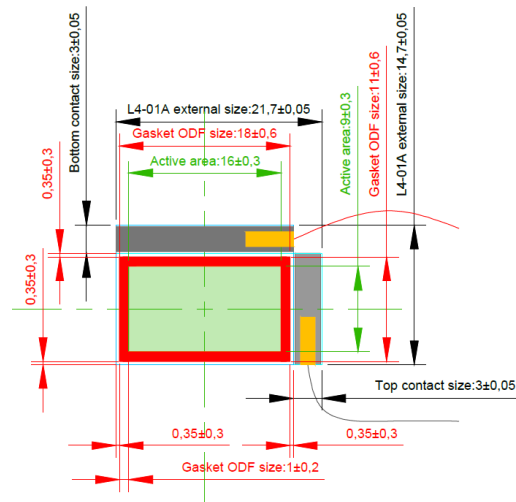
Figure 113.: Diffuser dimensions.

The smaller the size, the higher requirements for process and equipment and it must be proved that quality is stable for serial production. It is known that VCF method is used for small size display making but is time consuming, so ODF method is preferred. ODF line dispense machine Asymtek Axiom Jet head (DJ-9500) can dispense minimum 1 nL (~1 μg of LC) so theoretically it can be used to fill the micro-display volume 0.0015 ml (1.5 mg) if dispensed LC volume deviation from designed volume does not exceed 1.5 %. If cell gap should stay in 8±0.5 micron range, the LC weight should be 1.52±0.14 mg.

Table 33.: Specifications related to diffuser assembly and stacking.

Specification	Current	Goal	Chapter
Size, active area	62x49 mm	26x15 mm 16x9 mm	5
Distance between active LC layers	1.1 mm	0.66 mm	5, 6
Number of layers	47	39	4, 6
Inactive elements in size of 8μm	136 pcs/mm^2	0-100 pcs/mm^2	5
Total set transmission in open state	78%	82%	4, 5, 6

The same applies also to glass thickness. For optical chip used in AR-HMDs, certain distance (0.3 – 1.1 mm depending of the projection system) is needed between active LC layers, requiring use

of thin glass. The aim is to find minimum thickness, which still allows to use current LCD production line and still provide acceptable quality level. It must be noted, that production line is designed for minimum 0.4 mm thick glass, and glass bowing most likely require modifications of handling, processing and diffuser design.

The next aim is to make micro-diffuser with minimum spacer density or, preferably, without spacers at all. From substrate deflection Equation 14., one can calculate that 0.11 spacers/mm^2 are needed to avoid potential substrate bow more by 10% between 8µm spacers. This is very low number. Using Equation 12. we get that if we put 0.26 g per one spacer, it will decrease its height by 10 % (recommended compression at room temperature for displays), and by Equation 15. - 8.22 g maximum permissible load at which fracture will occur. This limits dynamic range for process load. For VCF process, after the LC capillary fill process, the excess of LC is squeezed out to get 10 % compression, typical pressure is 0.04 N/mm^2. From this load, diffuser would need 15 pcs per square mm^2. Yet, during LC capillary filling process itself, 0.1 N/mm^2 pressure is applied, so Equation 15. suggests that there should be at least two spacers for square mm to prevent cell total collapse and Equation 12. that spacer will be compressed by 46 %. However, both existing formulas cannot give value at which elastic deformation ends, so it is not clear that the shape will not be regained if we compress by 46 %. Also, influence of gasket as relatively incompressible support not far away, is not taken into account.

For ODF process, the pressure during assembly is lower – only 0.0005 N/mm^2 and when atmospheric pressure is renewed, the pressure is taken up by LC, so the bow is actually limited by LC volume in diffuser cell. 0.5 spacers/mm^2 could be realistic goal based on static calculations.

However, dynamic calculations would be more precise taking into account gasket region with spacers mixed in and area outside the cells without LC and spacers. Full 3D model of 33x22 mm cell was too complicated to build in COMSOL as computation requirements are very high due to multiple micron sized object meshing. However, it is possible to simplify model by calculation of glass displacement in 2D model, taking into account glass and spacer properties.

From spacer supplier datasheets [95] we find that Jung modulus of divinylbenzene spacer is very close to soda lime glass, so linear elastic modeling was applied to whole model. Let's define that 0.33mm glass edges are fully fixed (constrained) in place by the gasket, see Figure 114.
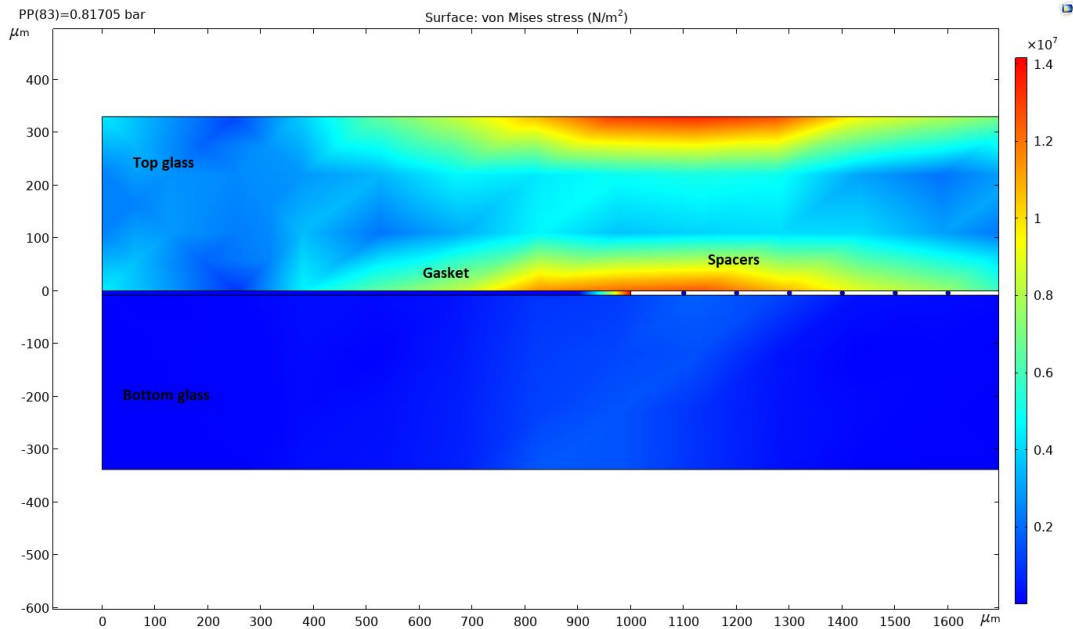
Figure 114.: COMSOL model for spacer compression.

For example, 8 μm thick spacerless cell, if no pressure is applied, the empty cell will retain its cell gap with only minimal sag (3%) in middle, see Figure 115., due to glass weight.
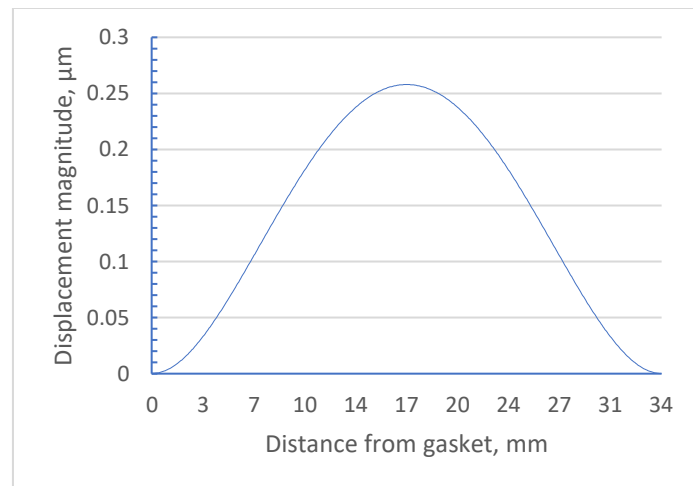
Figure 115.: Spacerless cell top glass sag under its own weigh.

However, during capillary vacuum fill of the empty cell, atmospheric pressure is applied to outside boundaries. At this condition, spacerless cell will collapse, see Figure 116. Most likely some gap near the gasket will remain but whether it allows cell LC filling, is highly unlikely.
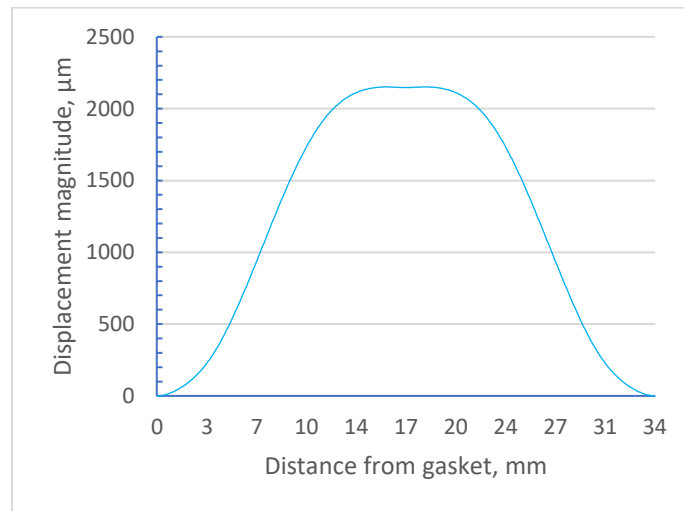
Figure 116.: Spacer less cell top glass deflection under atmospheric pressure. Note that 2000µm deflection value is larger than cell gap of 8µm, meaning collapse of the cell.

Cell gasket can provide cell gap control but due to thin, 0.33 mm glass, it can be applied for cells with active are less than 6 mm, see Figure 117.
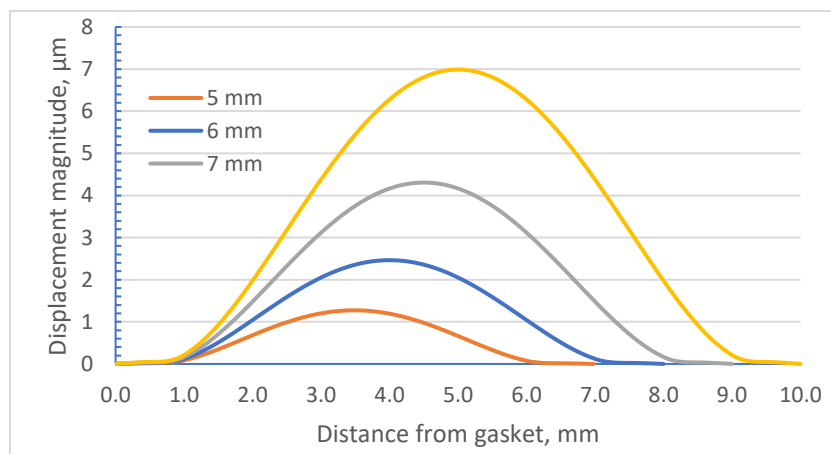
Figure 117.: Spacerless cell top glass deflection under 1 bar for various distances between gaskets.

We can conclude that spacers are necessary. By adding 8 µm spacers to our model we find cell gap change depending on spacer density during end seal process, see Table 34.

To avoid gap deviation more than our specified limit (±10%) we need at least 1 spacers per mm^2. In the same time, we must acknowledge that spacer spray is random process and areas of lower density will occur, so cell even with 4 spacers per mm^2 may not be achievable.

Table 34.: Gap change depending on spacer density from spacers in COMSOL model.

Spacers per mm^2	4	2	1	0.5	0.25	0.2	0.17	0.14
Gap change, μm	0.03	0.05	0.08	0.14	0.65	1.27	2.4	4.2

During production, cell must undergo several steps with different applied pressure. For 33x22 mm cell with 8 μm spacer density of 1 spacer/mm^2, cell gap change can be calculated for each step, see Table 35.

Table 35.: Cell gap change during process steps for 8um spacers.

Process step	Pressure N/mm^2	Gap change, μm
Without load	Glass own weight	0.001
Assembly in air	0.0004	0.06
Curing in multipress	0.005	0.35
Capillary vacuum fill	0.010	0.06
End seal press	0.014	0.08

Low spacer density, like 1 spacer/mm^2, could be achievable with photo spacer process, when each spacer is formed in prescribed place. If we use random spacer spray, we must take into account that some spacers might be missing due to clustering effect, see Figure 118.
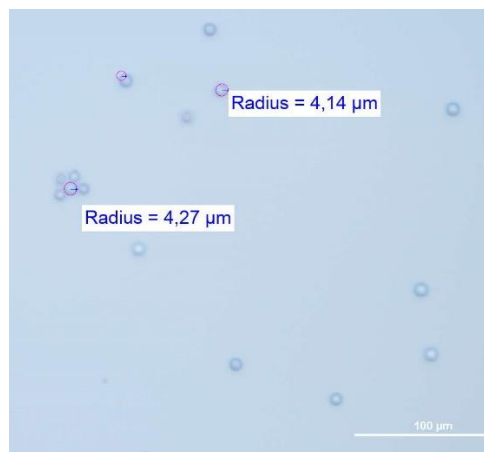
Figure 118.: Spacer distribution pattern showing cluster of five spacers and unpopulated areas nearby.

The influence of three missing spacer in the middle of the cell is larger than nearer to cell side, where it is stabilized by gasket, see Figure 119 and Figure 120.
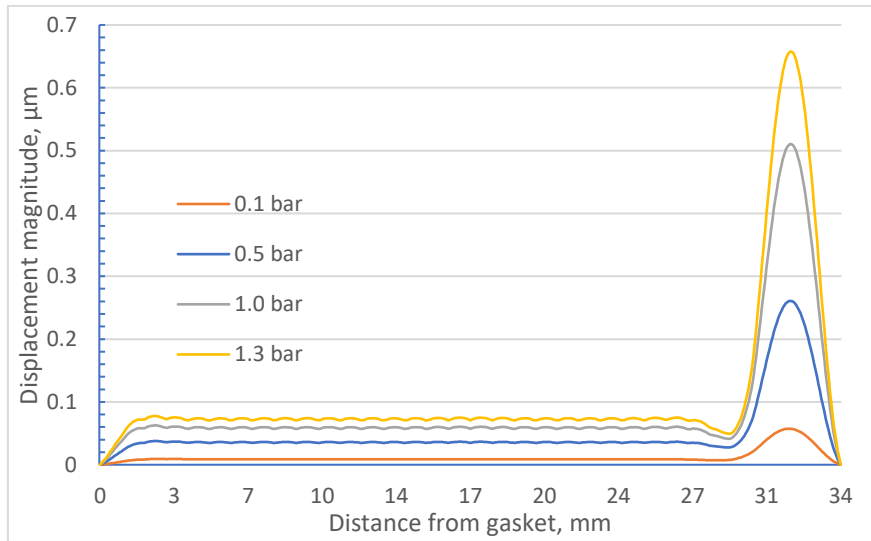
Figure 119.: Cell gap change of 1 spacer/mm² density cell during process steps. Three spacers near the gasket are removed.
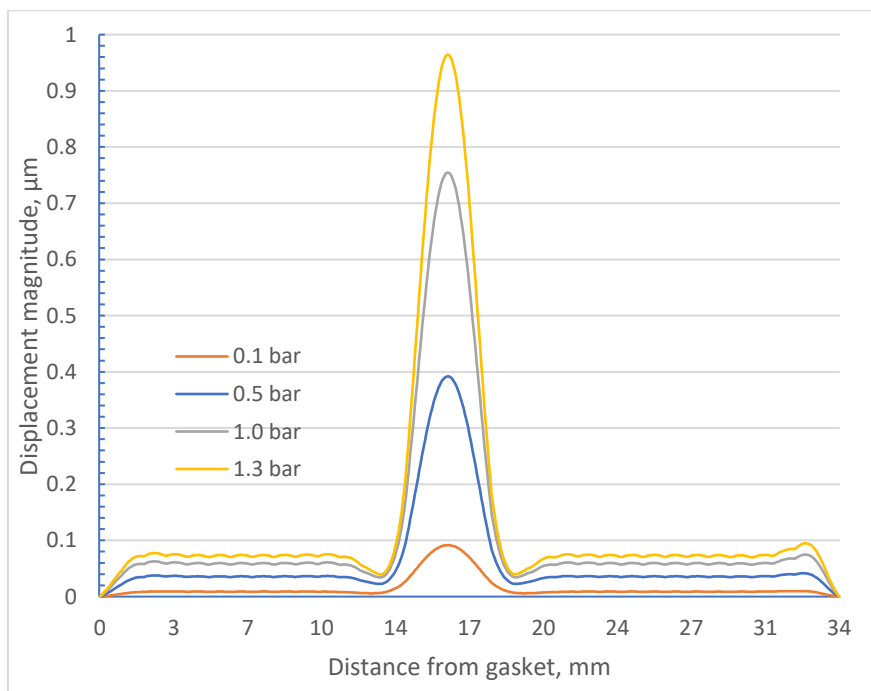
Figure 120.: Cell gap change of 1 spacer/mm² density cell during process steps. Three spacers in center are removed and 1 spacer near right side.

However, we find that absence of 6 spacers will result in cell gap collapse, see Figure 121.
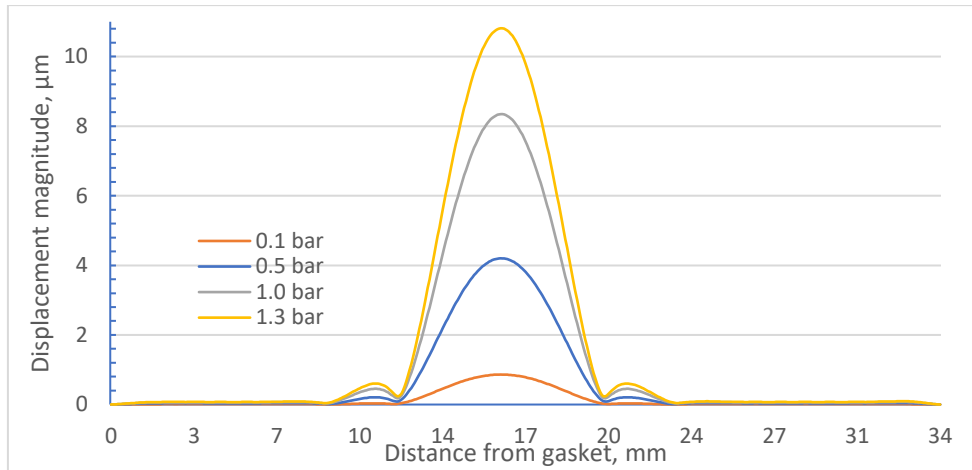
Figure 121.: Cell gap change of 1 spacer/mm² spacer density cell during process steps with 6 spacers missing in the center.

We can conclude that theoretically, spacer density below 1 spacer/mm^2 can be achievable for photo spacers but for conventional sprayed spacers, spacer densities must be higher to ensure that there are no unsupported areas. It is more a safety factor, and how close we can get to theoretical modelled density, must be determined experimentally. We can assume that at least safety factor of 5-10 is needed.

Cell gap due is larger near to gasket as gasket constrains movement in x direction, see Figure 122 for 10 spacers/mm^2. This could explain observed different switching regions near the gasket, however it must be noted that gasket could yield to the stress and in practice effect will be different.
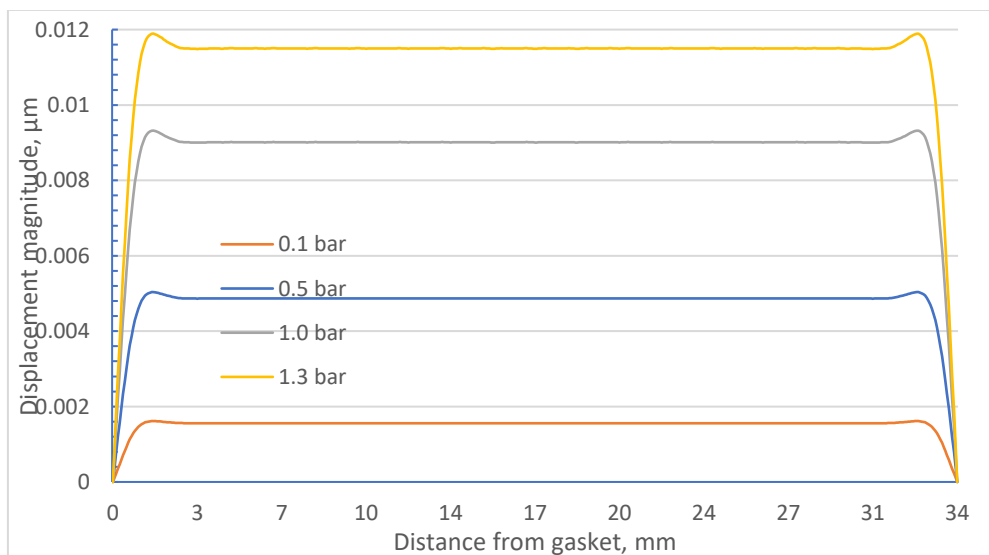
Figure 122.: Cell gap change for 10 spacers/mm² cell.

For diffuser lamination process into optical chip, lamination process is unconstrained, so there is no stress between bonding frame and individual diffusers and some z-axis dimension changes

can be tolerated. No specific optical alignment between individual elements is required but individual unit rotation must be avoided to ensure further defect free mechanical assembly. Serious drawback of the current case is the presence of wires, that must be soldered to contact pads before lamination otherwise it becomes very difficult to do it later due to restricted space. The key characteristics of adhesive must include the following attributes:

- Low birefringence and haze less, optically clear (high transmission) and particle/defect free
- Refractive Index as close as possible to glass
- Low moisture absorption and nonreactive with glass
- Low cost, readily available, non-hazardous ingredients
- Resistant to temperature effects; thermal soak and cycling
- Good UV, IR and life stability
- No out-gassing, bubble formation, or latent formations after bonding
- Possibility for repair-ability/ removal from partial assembly
- Short process time

Dry bonding is not preferred as it increases number of layers, three versus one in case of wet bonding. Besides, assembly in dry bonding requires specific machinery and adds haze. However, manual assembly is possible for skilled operator only for sizes comparable to human hands. Micro-diffusers in this case, are on the border of manual assembly capability. Anyway, we include tape for comparison purposes, 175um thick tape made by TESA.

Patterned adhesive dispensing is method of choice for small size. For liquid adhesives there is number of choices. Two component epoxy from Epo-Tek, satisfies the conditions above. The material can be cured in room temperature and curing time can be accelerated by temperature. The downside of longer curing time, is the requirement to fix materials to avoid misalignment and necessity to clean tooling and product after the process. UV hardening adhesive from Kyoritsu Chemicals WR-5500 is state-of-the-art material for optical part assembly, and solves long curing time, as UV exposure fixes the product. The disadvantage is relatively high cure shrinkage, 7.9 %. As representative of the silicone gel materials, that offer stress free assembly stack production, is Egel-3000 gel. It is very difficult to select materials according to their datasheet data, as nearly all of them have general data, like "transmission value >99 %", so to obtain real values of optical constants experimental measurements must be made.

5.3 Experimental part

LC volume and dispense pattern influence on cell vacuum assembly process

Before we attempt to decrease spacer density, we must achieve stable results and see that both possible methods (ODF and VCF) can r. ODF method qualification work started with preparation of 22x15 mm units from 0.5 mm borosilicate glass coated with 30 nm ITO and 260 nm SiO_x. The spacer density initially was planned 100 pcs/mm^2 like used for larger displays and 100 % fill ratio of LC. LC was dispensed in 3 drops, see Figure 123.
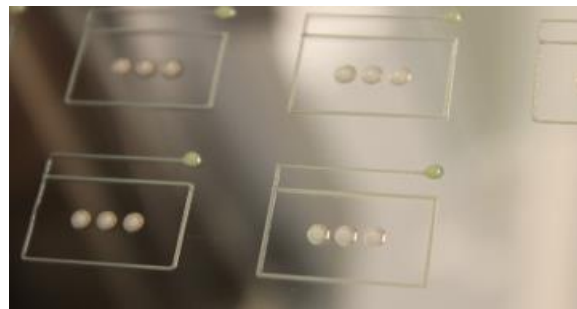
Figure 123.: Dispense pattern of 3 LC dots in middle of active area.

Spacer average density counted was 110 pcs/mm^2, enough to provide stable cell gap for the process, and less than 5 % compression is expected by atmospheric force in ODF process.

LC dispensing was stable with small deviations, see Table 36. but gasket dispense encountered problems. Due to small unit size and thin gasket, small gasket height is difficult to control. Partly in the first experiment the problems were mitigated by choosing less viscous ODF gasket material and reduction of active area (AA) as well as increase of assembly pressure but anyway overall yield was low.

Table 36.: Dispensing parameters for ODF process.

Number of dots	Dot weight (mg)	Target overfill	Designed LC weight (mg)	Measured LC weight (mg)	Deviation from target (%)	Assembly pressure, N
3	0,3841	0%	1,150	1,152	0,20	39,24
3	0,3600	0%	1,070	1,080	0,93	39,24
3	0,3605	0%	1,070	1,082	1,07	117,72
3	0,3585	0%	1,070	1,076	0,51	156,96
3	0,3538	0%	1,070	1,061	-0,80	156,96

In order to improve quality and yield, either different ODF equipment should be used with higher accuracy or VCF method should be used.

During E-O tests, 10 V above switching threshold in open state, haze zone was observed near gasket, see Figure 124. At first, it was attributed to thicker cell gap as predicted by model (Figure 122.), gap is thicker near the gasket. However, under microscope, it can be observed that in this region, LC are orienting differently than in middle of the cell, that led to hypothesis that SiO_x surface near gasket are somehow influenced by gasket. Similar observation was reported in literature[112], only for inorganic coatings. It is supposed that active SiO_x surface absorbs hydrocarbons from gasket material during manufacture that leads to change of surface alignment for LC. In our case, this haze zone can be countered by higher driving voltage.

a)   b)
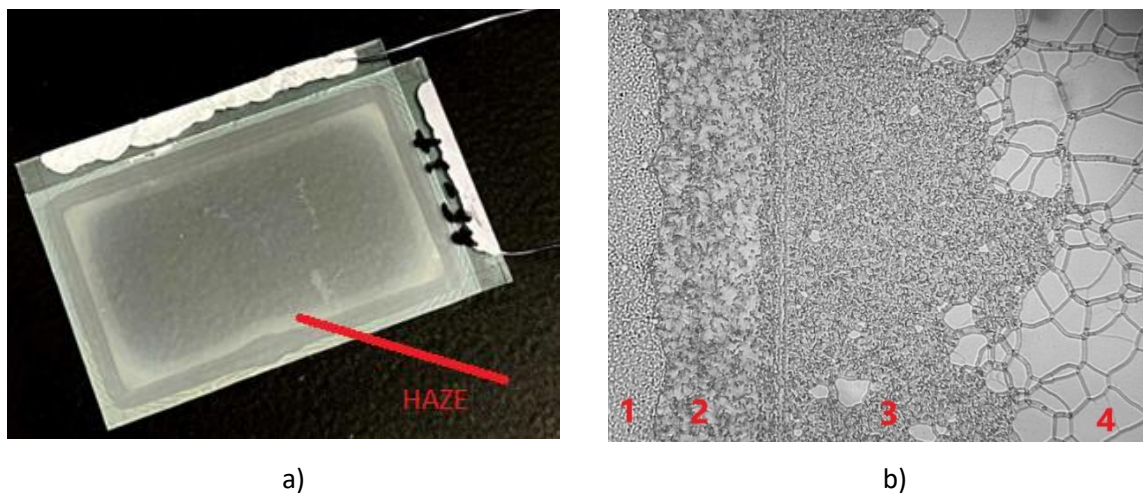
Figure 124.: ODF cell (33x22mm) in diffuse state during E-O test. a) "frame" like haze zone near gasket b) magnified haze zone, 1 – gasket, 2 – undriven area outside LC, 3- scattering FC zone, 4- transparent ULH zone.

VCF method qualification units were also made. The gasket quality was better due to less viscous gasket material as well as end press process used for gap homogenization. Due to small sizes, cutout rectangle with several units was used for VCF process. Two cells were filled simultaneously, fill ports sealed and rotated till all good cell are filled, see Figure 125.

Table 37.: E-O result comparison for cells made by ODF and VCF methods.

	Open, %	Close, %	Fall, µs	Rise, µs
ODF cells	88.6	16.1	677	1610
VCF cells	88.5	16.5	618	1341

E-O results, see Table 37, indicate that VCF version has fewer scattering properties, so the cell gap is thinner. This could also explain unit small color difference, as capillary fill version had blue tint and ODF version yellow tint.
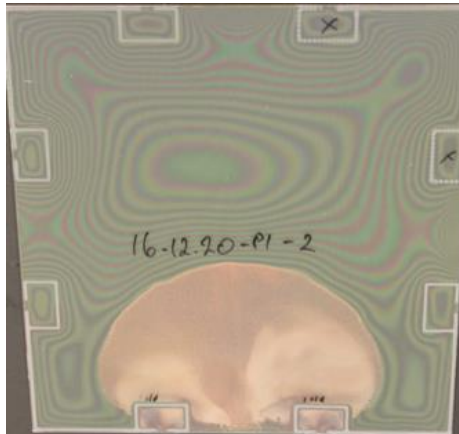
Figure 125.: Due to handling requirements, rectangle cutout is used for filling 2 cells at a time (bottom part). Note fringes due to cell gap differences. LC filled not only cells but also the gap between.

Thin glass use

After initial qualification, next step is to proceed with thinner 0.33 mm, soda lime glass. Devices were successfully prepared and only two notable issues for process were:

1) Thin glass sheet sag under their weight, see Figure 126. This precludes processing by robot hands as robot arm will collide with bent part;

2) Incompatibility with ultrasonic dry cleaner equipment. Suction force from ultrasonic/vacuum head causes thin and lightweight sheet debonding from table. Increasing table suction vacuum level did not provided any remedies.
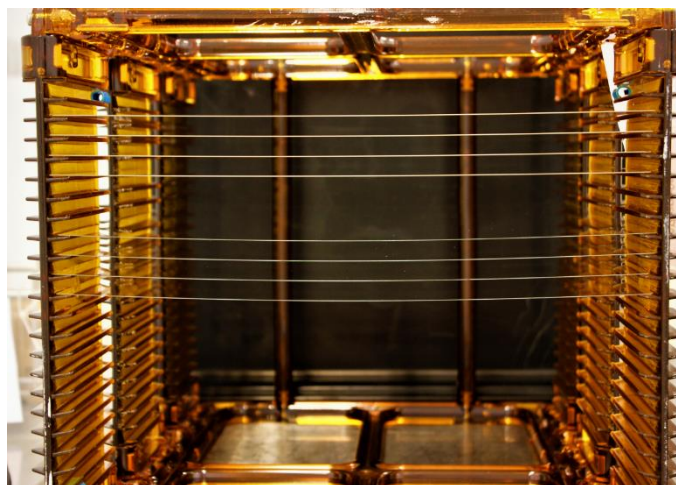
Figure 126.: 0.5 mm glass sheets (upper part) and 0.33 mm (lower part, bow observable) in robot loading cassettes.

Spacer density

Reduction of spacers density has been tried for 300x400 mm 12 μm diffuser panels (as there the effects would be more pronounced) where experimentally found spacer density is 20-22 pcs/mm^2. Reduction of spacer density below this value resulted in increased dielectric breakdown rate and visual inhomogeneity, see Figure 127. All diffusers with spacer density below 1 pcs/mm^2 had breakdown.

Figure 127.: Diffusers with various spacer density, left -22 pcs/mm2, middle - 2 pcs/mm2, left 0.2 pcs/mm2. Note rings from process pins and marks from finger touch. Small square areas inside display are intentionally made for cell gap measurement.

The next experiment was planned to optimize (decrease) spacer density in active area for micro-displays. Compared to previously mentioned 300x400 mm displays, for 22x15 mm case gasket support is more significant and might enable reduction of support spacers in active area.

In order to find optimum spacer density and test modeling validity, several 22x15 mm series with different 8 μm spacer density were manufactured. The results show close state transmittance decrease for lower spacer density due to thinner cell gap that leads to undesired loss of contrast, see Table 38. So, for vacuum capillary method (VCF) method, minimum spacer density most likely is above 100 pcs/mm^2.

Table 38.: Spacer density impact on VCF diffuser E-O properties .

Panel	Spacer density, pcs/mm^2	Open, %	**Close, %**	Fall time, μs	Rise time, μs
P3-2	130 ±20	89.1	**18.8**	658	1216
P3-4-1	37 ±10	89.6	**22.4**	674	874
P2-2-1	24 ±5	89.5	**25.1**	678	759
P2-4-1	8 ±2	88.7	**38.4**	710	335
	0.5 ±1	Half of AA is not filled with LC			
	Spacerless, 0	Half of AA is not filled with LC			

Very low density 0.5 spacers/mm^2 and spacerless approach resulted in inhomogeneous cell gap and incomplete filling, see Figure 128. Too little or no spacers inside the cell results in cell gap collapse in vacuum filling chamber, as predicted by model. We can also note that cell gap for spacerless display is even sensitive to applied driving voltage. Profilometer measurements show cell gap change of 0.5 μm (6.3 %) for this 22x15 mm display whereas for other types it is below 5 nm.
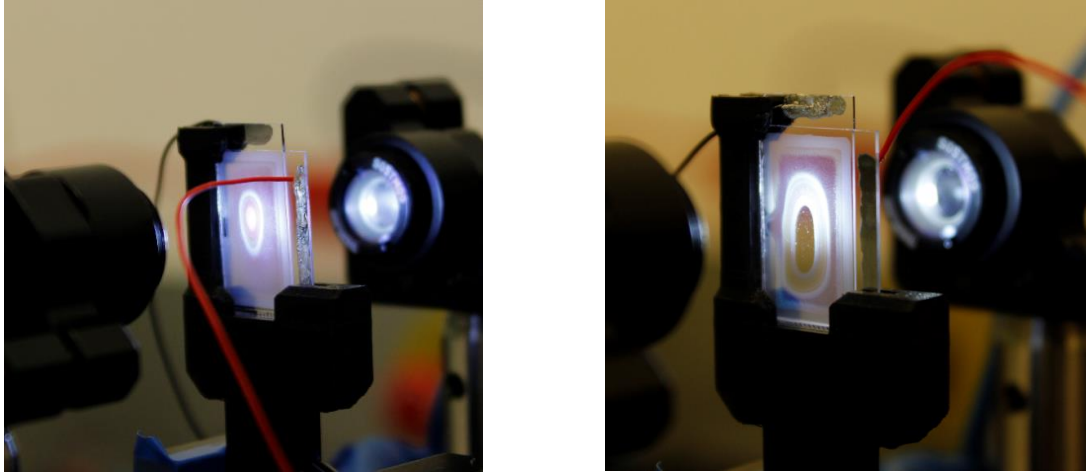
Figure 128.: Low density and spacer-less microdiffusers after incomplete capillary fill.

Since VCF method is not suitable for spacer number decrease, the only way left is to modify one-drop-fill (ODF) method. Gasket for this method is typically dispensed but dispensing too many small size elements decrease overall quality due to very long process time. Alternative is screenprinting, with advantage of consistency and speed but with much higher material consumption. For the experiment, 0.5 mm glass was selected, ITO was patterned and on top of it, 204-205 nm SiO$_x$ layer was sputtered and temperature treated for 3h at 300 °C. Gasket was screenprinted using 120-34 sieve with 29 μm emulsion and LC was dispensed within it with various underfill values. Spacers (8 μm, adhesive type) were deposited on opposite glass in 113 pcs/mm^2 average density. All panels were assembled in 0.06 mbar vacuum using 39 N pressing force and gasket was UV cured by 20.6 mW/cm^2 power followed by 2 h at 80 °C in curing oven. The results were satisfactory, showing dependence on underfill value (more LC corresponds to better scattering), see Figure 129. The most stable results are obtained for 3.8 % underfill ratio.
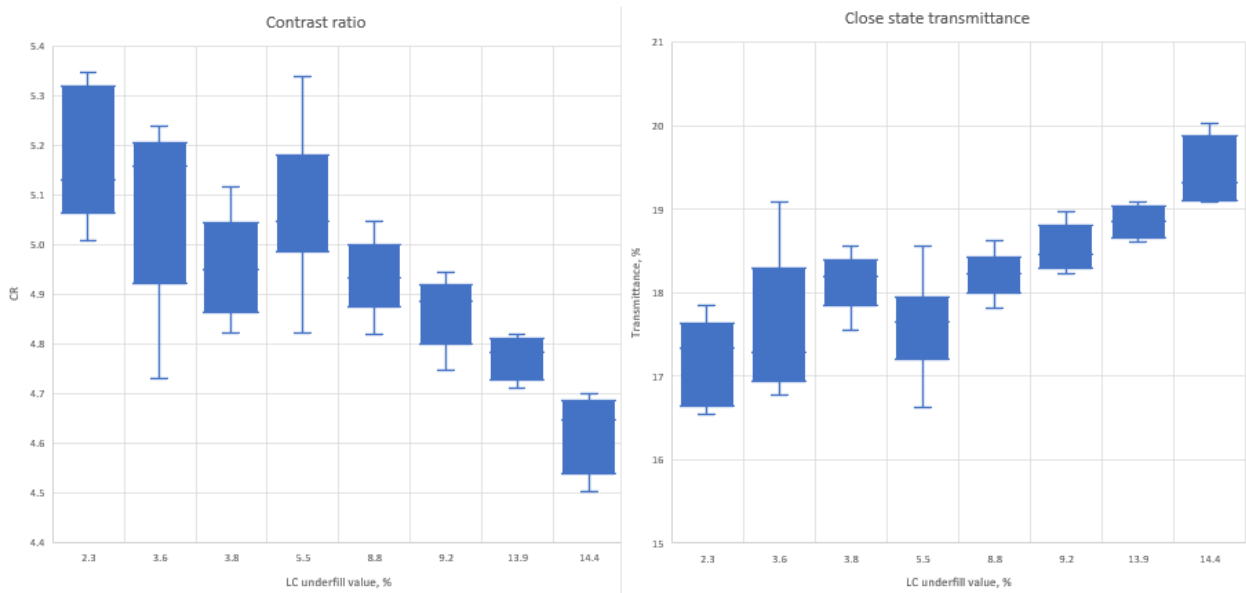
Figure 129.: Optical evaluation of ODF units. Left - contrast ratio, right - close state transmittance dependence on LC underfill value.

Further reduction of spacer density was done for cells made by ODF method with selected underfill ratio. This time, SiO_x coating was substituted by index matched SiO_xN_y coating. The cells were examined under polarizer to observe gap homogeneity, see Figure 130. Densities above 5 spacer per mm^2 have good uniformity.

| a) | b) | c) |
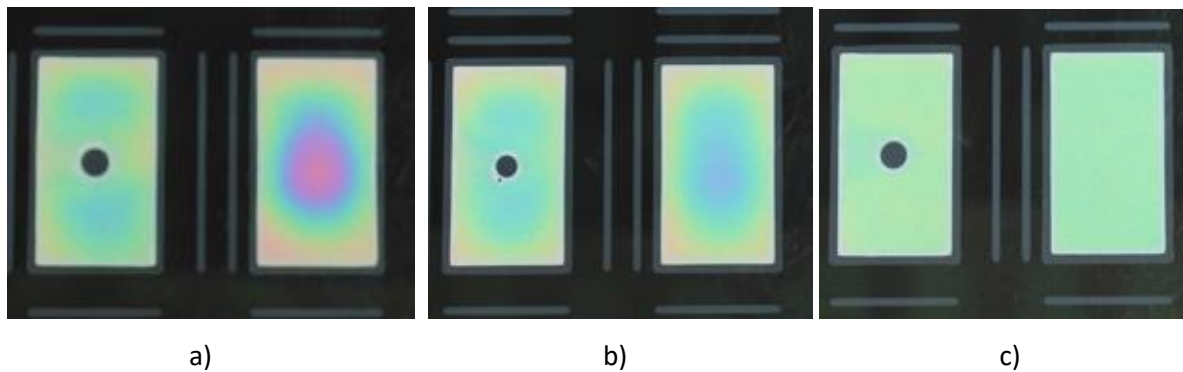
Figure 130.: Cell gap homogeneity of ODF cells with spacer density: a) spacerless, b) 2 spacer/mm², c) 5 spacer/mm². Cells on the left have support dot from the gasket material in the middle.

From the electro-optical test results, see Table 39, we can see that most stable results are obtained for 28 spacer/mm² density and while 5 spacer/mm² had good uniformity of cell gap, it is thinner.

Table 39.: E-O test results for ODF cells with various spacer density.

Spacer density, pcs/mm2	Open, %	Close, %	Close, STDEV%	Fall time, μs	Rise time, μs
99 ±16	91.0	21.5	0.6	720	1076
50 ±4	91.2	20.4	0.5	737	998
28 ±1	91.4	19.7	0.4	727	1059
5 ±1	91.5	23.5	0.5	741	797
2 ±1	91.3	26.0	1.1	750	647
none	91.5	35.0	5.1	785	385

Haze zone near gasket was minimal, confirming that less active SiO_xN_y is better, see Figure 131.

a)   b)
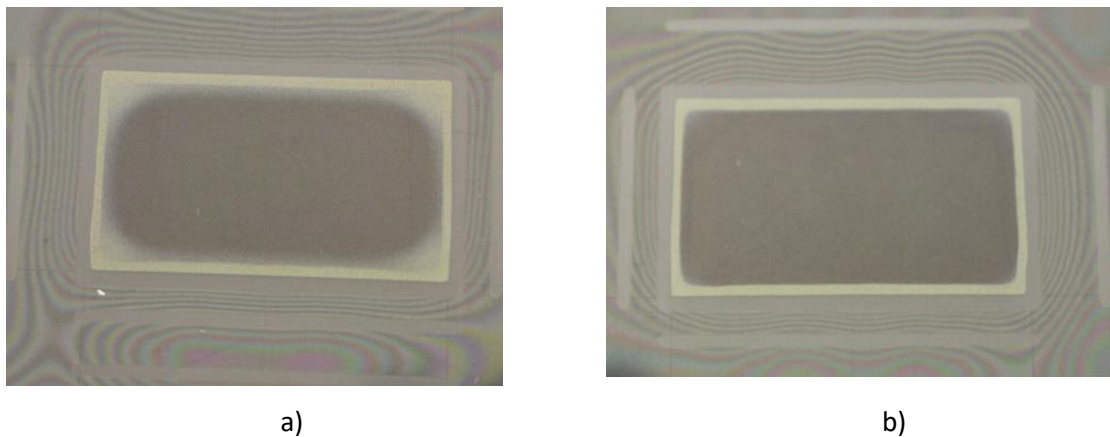
Figure 131.: Haze zone intensity for cells with different coatings a) SiO_x b) SiO_xN_y.

Selected materials for optical chip lamination were tested using micro-diffuser size glass with that were laminated with help of chosen materials.

Table 40.: Lamination material influence on BBAR coated glass stack transmittance.

Used material	Method	Transmittance at 550 nm, %	Reflectance at 550 nm, %	Absorption at 550 nm, %
Alpha-gel OPT K95E	Gel Dry bonding	84.6	6.7	8.7
WR5000	UV wet bonding	88.4	5.5	6.1
Tesa tape 69407	Tape dry bonding	80.0	2.8	17.2
EPOTEK-301-2FL	Epoxy wet bonding in RT	88.8	8.0	3.2

As it can be seen in Table 40., UV-curable adhesive and thermo-curable adhesive show the best transparency (88.4 % and 88.8 % respectively). WR5500, is preferred due to lower reflectance as its refractive index is closer to glass and fast curing by UV prevents glass sliding. The next best result is with OPT Alpha Gel (84.6 %). Tape has lower measured transparency, most likely due to defects in the laminated layers.

As suggested by literature and industry data, tape dry bonding requires special machinery to provide defect free layers, and they are not commercially available for this size at the moment. Lower transmission values are explained by LCD geometries, as they are not perfectly flat. Slightly rounded or concave surfaces, depending on LC temperature expansion, causes delamination and air gaps. Thicker tapes (TESA) can take more of the z-axis changes. Due to long curing time in RT, epoxy gel is not the material of choice for mass production, and WR5500 from Kyoritsu Chemicals is selected. Epotek-301-2FL can be used for small scale prototyping purposes.

Multifocal liquid crystal diffuser from 4 laminated units (33x22x0.7 mm) using WR5500 glue was made, see Figure 132.
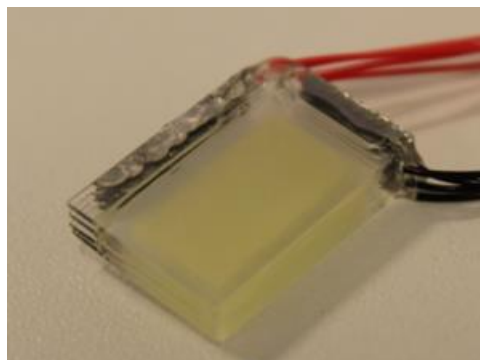
Figure 132.: Multifocal liquid crystal diffuser.

Multifocal liquid crystal diffusers were inserted in projection system AR-HMDs, see Figure 133.
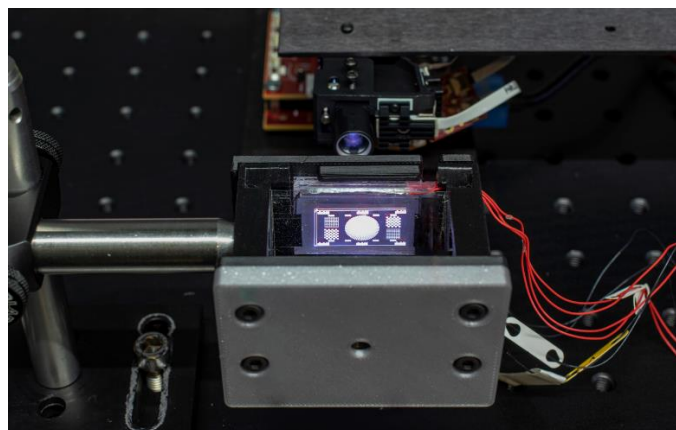
Figure 133.: AR-HMDs projection system in combination with multifocal liquid crystal diffuser.

Multifocal liquid crystal diffusers, see Figure 134., are successfully manufactured and used in Lightspace Technologies AR-HMDs models IG1050, see Figure 135.
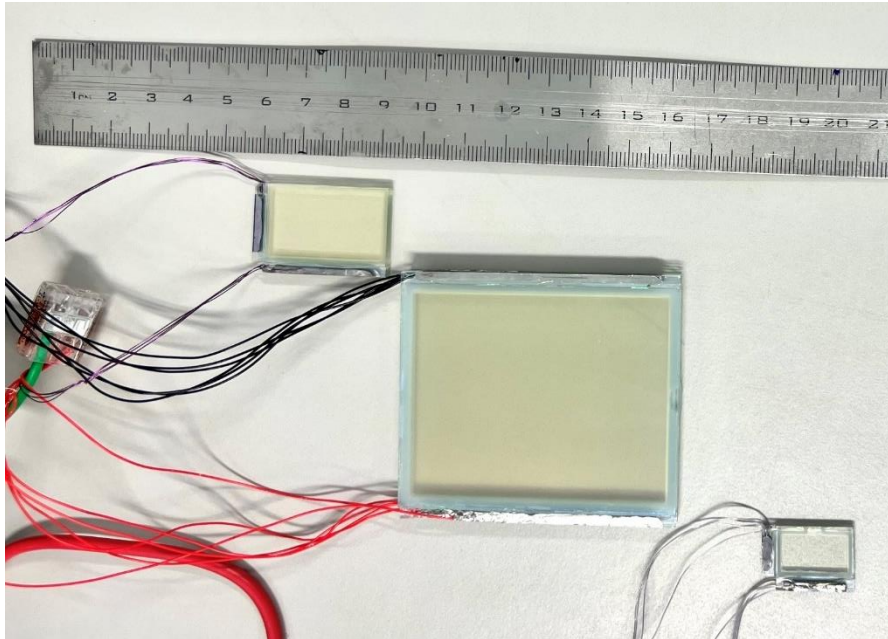
Figure 134.: Different form factor multifocal diffusers. Larger prototype from beginning of this work, shown in the middle.

Figure 135.: Lightspace AR-HMD with multifocal liquid crystal diffusers.

5.4 Conclusions

With less spacer density the distances between spacers are becoming larger and substrate deflection play more significant role. Theoretical assumptions and formula suppose that surfaces are perfectly flat and spacer distribution is ideal. In reality, assembly machine surfaces have 50μm flatness and we cannot control precise location of spacers with spray method, especially when lower densities are used. So, in fact there are regions where cell gap is locally decreased during assembly, and this explains increased electrical breakdowns for 400x300 mm diffusers.

Minimum spacer density for VCF method is 100 pcs/mm^2 and for ODF method – between 5-28 pcs/mm^2. Modelling suggests that for ODF method theoretical minimum is 0.5-1 pcs/mm^2 but probability of spacer clustering or few missing spacers requires safety factor larger than 5. Spacerless design is possible for cells smaller than 5x5 mm, then 0.33 mm glass can be sufficiently supported from gasket.

It is possible to decrease glass thickness down to 0.33 mm for cell construction, allowing more narrow distance between LC layer.

6. Summary and conclusions

Optimum material combination and structural design for diffusers have been found by using numerical modelling methods that decreased amount of experimental work and saving resources. COMSOL Multiphysics were used to build appropriate models that were validated by experimental results and, where applicable, by optical design software.

Key characteristics of a cholesteric liquid crystal diffuser, which is a part of multifocal liquid crystal diffuser, were evaluated:

- The dynamics of the relaxation process from homeotropic to focal conic transition was addressed, stressing on the influence of the different factors such as dopant concentration, electronic driving, and surface anchoring conditions;

- The dependence of the scattered light effectiveness of the diffuser on factors such as pointed above was also analyzed;

- The appearance of a transient state during the relaxation process from homeotropic to focal conic state, revealing its possible origin.

For instance, increasing the concentration of a chiral dopant used in the PFLC diffuser shortens cholesteric pitch and decrease switching time from homeotropic to focal conic state at the expense of increased driving voltage. However, the dependency of fall time *vs* concentration has a pronounced minimum after which increasing concentration of chiral additive increases the switching time, while decreasing the effectiveness of the diffuser element's light scattering power. For one of the highest HTP dopants, the optimum concentration is found to be about 2.5 %.

The surface anchoring condition also has an effect on characteristics of diffusers. The light-scattering characteristics can be facilitated by antiparallel surface alignment, which was shown to improve close state transmission by 82 % in comparison to homeotropic alignment while increasing switching time from homeotropic to focal conic by 30 %. The influence of the anchoring conditions is most prominent in the cells with thinner cell gap. Also, the close state transmittance value can be improved by yellow dye addition.

Transient increase of transmittance during change from transparent (homeotropic) state to diffuse (focal conic), cannot be explained by transient planar state, characteristic to PDLC, as there are no evidences in reflective and capacitive properties. Instead, uniform lying helix state formation is proposed. One possible way to remove it is to apply electric field with form of continuous decrease of

the applied voltage (ramp) to the diffuser rather than a sudden switch-off the voltage. Contrast for longer wavelengths can be improved by addition of yellow dye.

Diffuser type liquid crystal layer thickness measurement method based on capacitance measurements was developed and validated. COMSOL Multiphysics model have been used to compute capacitance values. Capacitance method has been validated by spectroscopic thickness measurement method for LC with known refractive index. Proposed LC layer thickness control method has been approbed for use in inline LCD production. Moreover, obtained value of layer thickness by this method was used to determine refractive index of novel liquid crystal mixture for diffuser (light scattering) LC. Knowledge of refractive index allows further optimization of LCD cells in future by index matching.

Transmittance values for multifocal diffuser have been improved by optical stack optimization. Thickness and properties of internal coating facing active LC were optimized for better optical performance. SiO_xN_y coating was developed for index matching dielectric layers as its refractive index can be easily adjusted by varying oxygen: nitrogen ratio during sputter process. Most notably less diffuser cell defects are observed as SiO_xN_y surface is less active in comparison to sputtered SiO_x.

Designated goal for spacerless diffuser design cannot be implemented and there is minimum necessary spacer density. With less spacer density the distances between spacers are becoming too large and substrate deflection start to play more significant role. In models based on theoretical assumptions and formulas we suppose that surfaces are perfectly flat and spacer distribution is ideal. In reality, assembly machine surfaces have 50µm flatness and for spacer wet spray method precise location of spacers cannot be controlled, especially when lower densities are used. It is not possible to decrease spacer density for capillary fill method. To achieve stable results, at least 25 pcs/mm^2 are required for ODF method. If lower density is required, it can be done by selecting larger diameter spacers thus compensating their ~20 % compression or other method (photo spacers) should be chosen.

Within in this thesis presented investigation, substantial improvement of multifocal liquid crystal diffusers properties (see Table 41.) have been reached and developed diffuser used in AR-HMDs.

Table 41.: Achieved specification results of the work.

Specification	At the start of work	Goal	Achieved results
Size, active area	62x49 mm	26x15 mm 16x9 mm	26x15 mm 16x9 mm
Distance between active LC layers	1.1mm	0.66 mm	0.66mm
Number of layers	47	39	39
Inactive elements in size of 8μm	136 pcs/mm^2	0-100 pcs/mm^2	25 pcs/mm^2
Total set transmission in open state	78 %	82 %	85 %
Individual unit transmision in diffuse state*	20.4 %	19 %	18.3 %
Individual unit transmision in open state*	89.3 %	90.5 %	92.3 %

*- without BBAR coatings on air/glass boundary.

Normalized transmittance of single diffuser was improved from 89.3 % to 92.3 %, that is higher than planned 90.5 % by using refractive index matching.

7. Thesis

- After fast removal of electric field in short pitch polymer free cholesteric liquid crystal systems transition from homeotropic to focal conic state occurs via transient uniform lying helix formation.

- Sputter coated SiO_xN_y film could be used to simultaneously fulfill four functions –passivation of conductive layer, refractive index matching, dielectric insulation and serve as alignment layer, besides, it effectively replaces two layers typically used in LC technology a silica based inorganic protective (hardcoat) layer and organic dielectric/alignment layer.

- Developed technology is used to produce miniature multi-layer liquid crystal diffuser with advanced electro-optical properties that meet the requirements of augmented reality displays.

8. Author's publication lists

Granted and *submitted* patents:

1. Osmanis, I. Ozols, A., Osmanis, K., Zabels R., Optical display arrangement and method of operation, US 2019 / 0146232 A1, May 16, 2019

2. Osmanis, I., Osmanis, K., Narels, M., Gertners, U., Zabels, R., Smaukstelis, A., Ozols, A.,Table - top volumetric display apparatus and method of displaying three - dimensional image, US 10,726,751 B2, Jul 28, 2020

3. Osmanis, I., Narels, M., Osmanis, K., Ozols, A., Gertners, U., Zabels. R., Display system for generating three-dimensional image and method therefor, US 17081183 (Application Number), Published: 28.04.2022.

4. Osmanis, I., Osmanis, K., Zabels, R., Narels, M., Gertners, U., Valters, G., Ozols, A., Near-eye display apparatus and method of displaying three-dimensional images, US 17109441 (Application Number), Published: 01.04.2021.

5. *Ozols, A., Osmanis, I., Osmanis, K., Narels, M., Mozolevskis, G., Zabels, R., Improved liquid crystal cell, US17/404,392 (submitted August 17, 2021)*

6. *Gertners, U., Osmanis, I. Narels, M., Ozols. A., Balode, S., Zabels R., Optical element for expanding and uniforming beam of light, US17/514,679 (submitted October 29, 2021)*

7. *Osmanis, I., Gertners, U., Osmanis, K., Narels, M., Greitans, M., Ozols, A., Balode, S., Zabels, R., Optical arrangement for expanding and uniformizing light beams, US17/581,169 (submitted January 21, 2022)*

Publications:

1. Zabels, R., Osmanis, K., Narels, Ozols, A., Osmanis, I., AR displays: Next-generation technologies to solve the vergence-accommodation conflict, Applied Sciences (Switzerland), 2019, 9(15), 3147, DOI:10.3390/app9153147.

2. Osmanis, K., Zabels, R., Ozols, A., Narels, M., Osmanis, I., Stereoscopic ar displays – towards solid-state multi-focal architecture, Digest of Technical Papers - SID International Symposium, 2020, 51(1), pp. 1638–1641, DOI:10.1002/sdtp.14208

3. Zabels, R.; Osmanis, K., Ozols, A.; Narels, M.; Gertners, U.; Smukulis, R.; Osmanis, I.; "Volumetric technology: enabling near-work compatible AR displays," Proc. SPIE 11304, Advances in Display Technologies X, 113040E (26 February 2020), DOI: 10.1117/12.2544891.

4. Ozols A.; Zutis E.; Zabels R.; Linina E.; Osmanis K.; Osmanis I.; "Fast-switching liquid crystal diffusers: outlook on optical properties and applicability in volumetric display architecture," Proc. SPIE 11788, Digital Optical Technologies 2021, 117880U (20 June 2021), DOI: 10.1117/12.2594147.

5. Ozols, A.; Mozolevskis, G.; Letko, E., Rutkis, M.; Zabels, R.; Linina, E.; Osmanis, I.; "Sputtered SiOxNy thin films: improving optical efficiency of liquid crystal diffuser elements in multi-focal near-to-eye display architecture," Proc. SPIE 11872, Advances in Optical Thin Films VII, 118720I (12 September 2021), DOI: 10.1117/12.2596885.

6. Ozols, A.; Mozolevskis, G.; Zalubovskis, R.; Rutkis, M.; "Development of liquid crystal layer thickness and refractive index measurement methods for scattering type liquid crystal displays", Latvian Journal of Physics and Technical Sciences, vol.59, no.4, 2022, pp.25-35. https://doi.org/10.2478/lpts-2022-0031.

7. Ozols, A.; Linina, E.; Zabels, R.; Komitov, L. Evaluation of the Characteristics of Cholesteric Liquid Crystal Diffuser Element Applied in Multi-Focal Display Architectures. Crystals 2022, 12, 733. DOI: 10.3390/cryst12050733.

Conferences:

- A. Ozols, G. Mozolevskis, E. Letko, M. Rutkis, R. Zabels, E. Linina, I. Osmanis, "Sputtered SiOxNy thin films: improving optical efficiency of liquid crystal diffuser elements in multi-focal near-to-eye display architecture," SPIE Optical Systems Design, 2021, Online Only.

- A. Ozols, E. Zutis, R. Zabels, E. Linina, K.Osmanis, I. Osmanis, "Fast-switching liquid crystal diffusers: outlook on optical properties and applicability in volumetric display architecture," SPIE Digital Optical Technologies, 2021, Online Only.

- A.Ozols, "What silica-based thin films could do for augmented reality displays?", FM&NT – NIBS 2022.

- A.Ozols, E.Linina, R.Zabels, "Optimization of Total Light Transmittance for AR/VR Displays by Use of Silica Based Thin Films", Eurodisplay 2022.

9. References

[1] G. Shiers, "Ferdinand Braun and the Cathode Ray Tube," *Sci Am*, vol. 230, no. 3, pp. 92–101, Mar. 1974, doi: 10.1038/scientificamerican0374-92.

[2] ITU Publications, "Measuring digital development: facts and figures," Geneva, 2019.

[3] B. Blundell and A. Schwarz, "Volumetric Three-Dimensional Display Systems," *Volumetric Three-Dimensional Display Systems, by Barry G. Blundell, Adam J. Schwarz, pp. 330. ISBN 0-471-23928-3. Wiley-VCH , March 2000.*, Mar. 2000.

[4] J. Geng, "Three-dimensional display technologies," *Advances in Optics and Photonics*, vol. 5, no. 4, p. 456, Dec. 2013, doi: 10.1364/AOP.5.000456.

[5] D. Smalley, T.-C. Poon, H. Gao, J. Kvavle, and K. Qaderi, "Volumetric Displays: Turning 3-D Inside-Out," *Optics and Photonics News*, vol. 29, no. 6, p. 26, Jun. 2018, doi: 10.1364/OPN.29.6.000026.

[6] D. E. Smalley *et al.*, "A photophoretic-trap volumetric display," *Nature*, vol. 553, no. 7689, pp. 486–490, Jan. 2018, doi: 10.1038/nature25176.

[7] S. F. Keane, A. . Jackson, G. F. Smith, W. J. Tamblyn, and K. Silverman, "Volumetric 3D display," 10,401,636 B2, 2019

[8] J. Koo and D. Kim, "Volumetric three-dimensional (3D) display system using transparent flexible display panels," 7.587,120 B2, 2009

[9] A. Sullivan, "DepthCube solid-state 3D volumetric display," *Stereoscopic Displays and Virtual Reality Systems XI*, vol. 5291, pp. 279–284, May 2004, doi: 10.1117/12.527543.

[10] M. S. Banks, J. Kim, and T. Shibata, "Insight into Vergence-Accommodation Mismatch," *Proc SPIE Int Soc Opt Eng*, vol. 8735, p. 873509, May 2013, doi: 10.1117/12.2019866.

[11] T. Shibata, J. Kim, D. M. Hoffman, and M. S. Banks, "Visual discomfort with stereo displays: Effects of viewing distance and direction of vergence-accommodation conflict," *Proc SPIE Int Soc Opt Eng*, vol. 7863, p. 78630P, Feb. 2011, doi: 10.1117/12.872347.

[12] T. Zhan, J. Xiong, J. Zou, and S.-T. Wu, "Multifocal displays: review and prospect," *PhotoniX 2020 1:1*, vol. 1, no. 1, pp. 1–31, Mar. 2020, doi: 10.1186/S43074-020-00010-0.

[13] K. Aksit, W. Lopes, J. Kim, P. Shirley, and D. Luebke, "Near-eye varifocal augmented reality display using see-through screens," *ACM Transactions on Graphics*, vol. 36, no. 6, Nov. 2017, doi: 10.1145/3130800.3130892.

[14] X. Hu and H. Hua, "High-resolution optical see-through multi-focal-plane head-mounted display using freeform optics," *Opt Express*, vol. 22, no. 11, p. 13896, Jun. 2014, doi: 10.1364/OE.22.013896.

[15] G. Gu *et al.*, "Transparent stacked organic light emitting devices. I. Design principles and transparent compound electrodes," *Journal of Applied Physics*, vol. 86, no. 8, pp. 4067–4075, Oct. 1999, doi: 10.1063/1.371331.

[16] G. Gu, G. Parthasarathy, P. Tian, P. E. Burrows, and S. R. Forrest, "Transparent stacked organic light emitting devices. II. Device performance and applications to displays," *Journal of Applied Physics*, vol. 86, no. 8, p. 4076, Sep. 1999, doi: 10.1063/1.371428.

[17] D. K. Yang and S. T. Wu, "Fundamentals of Liquid Crystal Devices," *Fundamentals of Liquid Crystal Devices*, vol. 9781118752005, pp. 1–570, Dec. 2014, doi: 10.1002/9781118751992.

[18] A. Ozols, E. Zutis, R. Zabels, E. Linina, K. Osmanis, and I. Osmanis, "Fast-switching liquid crystal diffusers: outlook on optical properties and applicability in volumetric display architecture," in *Digital Optical Technologies 2021*, Jun. 2021, p. 26. doi: 10.1117/12.2594147.

[19] N. Broy, F. Alt, S. Schneegass, N. Henze, and A. Schmidt, "Perceiving layered information on 3D displays using binocular disparity," *PerDis 2013 - Proceedings: 2nd ACM International Symposium on Pervasive Displays 2013*, pp. 61–66, 2013, doi: 10.1145/2491568.2491582.

[20] J. E. Cutting and P. M. Vishton, "Perceiving Layout and Knowing Distances: The Integration, Relative Potency, and Contextual Use of Different Information about Depth," *Perception of Space and Motion*, pp. 69–117, Jan. 1995, doi: 10.1016/B978-012240530-3/50005-5.

[21] M. S. Banks, J. C. A. Read, R. S. Allison, and S. J. Watt, "Stereoscopy and the human visual system," *SMPTE Motion Imaging Journal*, vol. 121, no. 4, pp. 24–43, 2012, doi: 10.5594/J18173.

[22] T. Shibata, J. Kim, D. M. Hoffman, and M. S. Banks, "Visual discomfort with stereo displays: Effects of viewing distance and direction of vergence-accommodation conflict," *Proc SPIE Int Soc Opt Eng*, vol. 7863, p. 78630P, Feb. 2011, doi: 10.1117/12.872347.

[23] D. M. Hoffman, A. R. Girshick, K. Akeley, and M. S. Banks, "Vergence-accommodation conflicts hinder visual performance and cause visual fatigue," *Journal of Vision*, vol. 8, no. 3, Mar. 2008, doi: 10.1167/8.3.33.

[24] M. S. Banks, J. Kim, and T. Shibata, "Insight into Vergence-Accommodation Mismatch," *Proc SPIE Int Soc Opt Eng*, vol. 8735, p. 873509, May 2013, doi: 10.1117/12.2019866.

[25] "Magic Leap Review Part 1 - The Terrible View Through Diffraction Gratings - KGOnTech." https://kguttag.com/2018/09/26/magic-leap-review-part-1-the-terrible-view-through-diffraction-gratings/ (accessed May 08, 2022).

[26] "US7587120B2 - Volumetric three-dimensional (3D) display system using transparent flexible display panels - Google Patents." https://patents.google.com/patent/US7587120B2/en (accessed May 08, 2022).

[27] J. Rick Chang, B. v K Vijaya Kumar, A. C. Sankaranarayanan, and J.-H. Rick Chang, "Towards Multifocal Displays with Dense Focal Stacks," *ACM Transactions on Graphics*, vol. 37, no. 6, p. 13, 2018, doi: 10.1145/3272127.

[28] R. Zabels *et al.*, "AR Displays: Next-Generation Technologies to Solve the Vergence–Accommodation Conflict," *Applied Sciences 2019, Vol. 9, Page 3147*, vol. 9, no. 15, p. 3147, Aug. 2019, doi: 10.3390/APP9153147.

[29] K. Osmanis, R. Zabels, A. Ozols, M. Narels, and I. Osmanis, "Stereoscopic ar displays – towards solid-state multi-focal architecture," *Digest of Technical Papers - SID International Symposium*, vol. 51, no. 1, pp. 1638–1641, 2020, doi: 10.1002/SDTP.14208.

[30] S. C. Shin *et al.*, "Removal of hot spot speckle on rear projection screen using the rotating screen system," *IEEE/OSA Journal of Display Technology*, vol. 2, no. 1, pp. 79–84, Mar. 2006, doi: 10.1109/JDT.2005.863779.

[31] R. H. Chen, *Liquid crystal displays : fundamental physics and technology*. Wiley, 2011.

[32] D. Coates, W. A. Crossland, J. H. Morrisy, and B. Needham, "Electrically induced scattering textures in smectic A phases and their electrical reversal," *Journal of Physics D: Applied Physics*, vol. 11, no. 14, p. 2025, Oct. 1978, doi: 10.1088/0022-3727/11/14/012.

[33] S. v. Pasechnik, V. G. (Vladimir G.) Chigrinov, and D. v. Shmeliova, *Liquid crystals : viscous and elastic properties*. Wiley-VCH, 2009.

[34] A. K. Jain and R. R. Deshmukh, "An Overview of Polymer-Dispersed Liquid Crystals Composite Films and Their Applications," *Liquid Crystals and Display Technology*, Oct. 2020, doi: 10.5772/INTECHOPEN.91889.

[35] J. Chen, W. Cranton, and M. Fihn, "Handbook of visual display technology," *Handbook of Visual Display Technology*, pp. 1–3564, Jan. 2016, doi: 10.1007/978-3-319-14346-0.

[36] P. E. Watson, "The homeotropic to planar transition in cholesteric liquid crystals /," Kent State University, 2000. Accessed: May 08, 2022. [Online]. Available: https://www.researchgate.net/publication/35743508_The_homeotropic_to_planar_transitio n_in_cholesteric_liquid_crystals?msclkid=e4c4c694cecd11ecb20532f0dec3ecf1

[37] J. E. Anderson, P. Watson, T. Ernst, and P. J. Bos, "Computer simulation evidence of the transient planar state during the homeotropic to focal conic transition in cholesteric liquid crystals," *Phys Rev E Stat Phys Plasmas Fluids Relat Interdiscip Topics*, vol. 61, no. 4 Pt A, pp. 3951–3960, 2000, doi: 10.1103/PHYSREVE.61.3951.

[38] J. E. Anderson, "Transitions from the homeotropic state in cholesteric liquid crystals," Kent State University, 2000.

[39] L. M. Blinov, "Structure and Properties of Liquid Crystals," *Structure and Properties of Liquid Crystals*, 2011, doi: 10.1007/978-90-481-8829-1.

[40] A. Sullivan and JOHNSON SARA L, "3D display devices with transient light scattering shutters," 20020113753, 2002

[41] S. Palmer and B. Backlund, "Polymer-free Cholesteric Textured (PFCT) Liquid Crystal Optical-shutters," Borlange, 2005.

[42] F. Bruyneel, "Method for measuring the cell gap in liquid-crystal displays," *Optical Engineering*, vol. 40, no. 2, p. 259, Feb. 2001, doi: 10.1117/1.1337036.

[43] J. Li, C. H. Wen, S. Gauza, R. Lu, and S. T. Wu, "Refractive indices of liquid crystals for display applications," *IEEE/OSA Journal of Display Technology*, vol. 1, no. 1, pp. 51–61, Sep. 2005, doi: 10.1109/JDT.2005.853357.

[44] E. Nitiss, R. Usans, and M. Rutkis, "Simple method for measuring bilayer system optical parameters," *https://doi.org/10.1117/12.922317*, vol. 8430, pp. 380–390, May 2012, doi: 10.1117/12.922317.

[45] "A model for the formation of mura during the One-Drop-Filling process — University of Strathclyde." https://pureportal.strath.ac.uk/en/publications/a-model-for-the-formation-of-mura-during-the-one-drop-filling-pro?msclkid=e3d40af2cecf11ec9f258bd2ea1392ae (accessed May 08, 2022).

[46] S. Valyukh, S. Sorokin, and V. G. Chigrinov, "Inline Quality Control of Liquid Crystal Cells," *Journal of Display Technology*, vol. 11, no. 12, pp. 1042–1047, Dec. 2015, doi: 10.1109/JDT.2015.2434939.

[47] C. F. Kao, S. K. Tsai, and S. H. Lu, "Measuring cell gap of liquid crystal displays by scanning white-light tandem interferometry," *Japanese Journal of Applied Physics*, vol. 48, no. 10 Part 1, pp. 1065081–1065084, 2009, doi: 10.1143/JJAP.48.106508.

[48] L.-Y. Ding, W.-P. Shih, M.-H. Lin, Y.-C. Hu, and P.-Z. Chang, "An analytical model for instant design of an LCD cell with photospacers under gravity and local loading," *J Soc Inf Disp*, vol. 20, no. 3, pp. 148–155, Mar. 2012, doi: 10.1889/JSID20.3.148.

[49] R. Gotlaufs, "Research on electrically controllable optical diffusers and development of an improved electrical drive circuit," Master Thesis, Riga Technical University, 2018.

[50] Y. B. Kim and I. K. Hur, "High speed response time of nematic liquid crystal mixtures for LCD monitor and TV applications," *https://doi.org/10.1080/15980316.2001.9651863*, vol. 2, no. 3, pp. 32–38, 2010, doi: 10.1080/15980316.2001.9651863.

[51] H. Wang, X. Nie, T. X. Wu, and S. T. Wu, "Cell gap effect on the dynamics of liquid crystal phase modulators," *Molecular Crystals and Liquid Crystals*, vol. 454, no. 1, pp. 285/[687]-295/[697], Sep. 2006, doi: 10.1080/15421400600655824.

[52] A. G. Kozachenko and L. Komitov, "Influence of the surfaces on the nucleation process during the cholesteric-nematic transition," *Molecular Crystals and Liquid Crystals*, vol. 412, 2004, doi: 10.1080/15421400490439833.

[53] G. Hegde, A. Kozachenko, and L. Komitov, "Generation of hidden bistable images in a cholesteric liquid crystal device," *Liquid Crystals*, vol. 48, no. 15, pp. 2076–2085, 2021, doi: 10.1080/02678292.2021.1921865.

[54] G. Mozolevskis, I. Sekacis, E. Nitiss, A. Medvids, and M. Rutkis, "Dielectric breakdown of fast switching LCD shutters," *Advances in Display Technologies VII*, vol. 10126, p. 1012607, Feb. 2017, doi: 10.1117/12.2252492.

[55] K. Osmanis *et al.*, "Advanced multiplanar volumetric 3d display," p. 36, Feb. 2018, doi: 10.1117/12.2297629.

[56] A. Eisen-Enosh, N. Farah, Z. Burgansky-Eliash, U. Polat, and Y. Mandel, "Evaluation of Critical Flicker-Fusion Frequency Measurement Methods for the Investigation of Visual Temporal Resolution," *Scientific Reports*, vol. 7, no. 1, Dec. 2017, doi: 10.1038/S41598-017-15034-Z.

[57] C. LANDIS, "Determinants of the Critical Flicker-Fusion Threshold," *https://doi.org/10.1152/physrev.1954.34.2.259*, vol. 34, no. 2, pp. 259–286, Apr. 1954, doi: 10.1152/PHYSREV.1954.34.2.259.

[58] C. Tani, "Phase Transition Temperature Dependence of Field-Induced Nematic-Cholesteric Relaxation Time," *Japanese Journal of Applied Physics*, vol. 18, no. 7, pp. 1387–1388, Jul. 1979, doi: 10.1143/JJAP.18.1387.

[59] G. W. Gray, "Dyes and liquid crystals," *Dyes and Pigments*, vol. 3, no. 2–3, pp. 203–209, Apr. 1982, doi: 10.1016/0143-7208(82)80023-5.

[60] K. Beev, P. Bos, and X. Feng, "Polarization-independent fast optical shutter with high transmission," *Applied Optics, Vol. 58, Issue 17, pp. 4622-4629*, vol. 58, no. 17, pp. 4622–4629, Jun. 2019, doi: 10.1364/AO.58.004622.

[61] A. M. Mandong and A. Uzum, "Fresnel calculations of double/multi-layer antireflection coatings on silicon substrates," *Research on Engineering Structures and Materials*, vol. 7, no. 4, pp. 539–550, 2021, doi: 10.17515/RESM2020.241EN1217.

[62] A. Stadler, "Transparent Conducting Oxides-An Up-To-Date Overview," *Materials (Basel)*, vol. 5, no. 4, pp. 661–683, Apr. 2012, doi: 10.3390/MA5040661.

[63] EuroLCDs, "INdustrial Scale Production of Innovative nanomateRials for printEd Devices," Ventspils, 2019.

[64] B. S. Chiou and J. H. Tsai, "Antireflective coating for ITO films deposited on glass substrate," *Journal of Materials Science: Materials in Electronics 1999 10:7*, vol. 10, no. 7, pp. 491–495, 1999, doi: 10.1023/A:1008924018328.

[65] G. H. Guai, Q. L. Song, Z. S. Lu, and C. M. Li, "Effects of multiple heat treatment cycles on structure, optical and electrical properties of indium-tin-oxide thin films," *Surface and Coatings Technology*, vol. 205, no. 8–9, pp. 2852–2856, Jan. 2011, doi: 10.1016/J.SURFCOAT.2010.10.062.

[66] "US20050206820A1 - Fast optical shutter - Google Patents." https://patents.google.com/patent/US20050206820A1/en (accessed May 08, 2022).

[67] H. Takanashi, J. E. Maclennan, and N. A. Clark, "Sub 100 nanosecond pretilted planar-to-homeotropic reorientation of nematic liquid crystals under high electric field," *Japanese Journal of Applied Physics, Part 1: Regular Papers and Short Notes and Review Papers*, vol. 37, no. 5 A, pp. 2587–2589, May 1998, doi: 10.1143/JJAP.37.2587/XML.

[68] M. W. Geis, T. M. Lyszczarz, R. M. Osgood, and B. R. Kimball, "30 to 50 ns liquid-crystal optical switches," *Optics Express*, vol. 18, no. 18, p. 18886, Aug. 2010, doi: 10.1364/OE.18.018886.

[69] W. C. Elmore, "The Transient Response of Damped Linear Networks with Particular Regard to Wideband Amplifiers," *Journal of Applied Physics*, vol. 19, no. 1, p. 55, Apr. 2004, doi: 10.1063/1.1697872.

[70] Nissan Chemical, "LCD coating material data sheet." 2012.

[71] H. S. Vanegas, M. Pinzón, J. E. Alfonso, J. J. Olaya, and C. Pineda-Vargas, "Chemical characterization and optical properties of SiOxNy films deposited on common glass substrate," *Materials Express*, vol. 6, no. 3, pp. 295–299, Jun. 2016, doi: 10.1166/MEX.2016.1306.

[72] J. Souk, S. Morozumi, F.-C. Luo, and I. Bita, "Flat panel display manufacturing".

[73] D. Armitage, I. Underwood, and S. T. Wu, "Introduction to Microdisplays," *Introduction to Microdisplays*, pp. 1–377, May 2007, doi: 10.1002/9780470057056.

[74] "How Clean Is Clean? Measuring Surface Cleanliness and Defining Acceptable Levels of Cleanliness," pp. 179–194, Apr. 2011, doi: 10.1201/B10858-17.

[75] M. A. Rodríguez-Valverde, M. A. Cabrerizo-Vílchez, P. Rosales-López, A. Páez-Dueas, and R. Hidalgo-Álvarez, "Contact angle measurements on two (wood and stone) non-ideal surfaces," *Colloids and Surfaces A: Physicochemical and Engineering Aspects*, vol. 206, no. 1–3, pp. 485–495, Jul. 2002, doi: 10.1016/S0927-7757(02)00054-7.

[76] "Mobile Surface Analyzer-MSA One-Click SFE | KRÜSS Scientific." https://www.kruss-scientific.com/en/products-services/products/msa-one-click-sfe (accessed May 08, 2022).

[77] A. K. Varshneya and J. C. Mauro, "Fundamentals of inorganic glasses," *Fundamentals of Inorganic Glasses*, pp. 1–735, Jan. 2019, doi: 10.1016/C2017-0-04281-7.

[78] S. H. Perlmutter, D. Doroski, and G. Moddel, "Degradation of liquid crystal device performance due to selective adsorption of ions," *Applied Physics Letters*, vol. 69, no. 9, pp. 1182–1184, Aug. 1996, doi: 10.1063/1.117404.

[79] H. J. Glaser, *Large area glass coating*. Von Ardenne Anlagentechnik Gmb, 2005.

[80] "Augmented Reality Solutions." https://www.corning.com/worldwide/en/products/advanced-optics/product-materials/PrecisionGlassSolutions/augmented-reality-solutions.html?msclkid=880256b5cedf11ec8c23d5548da382a8 (accessed May 08, 2022).

[81] H. Bach and D. Krause, Eds., "Thin Films on Glass," 2003, doi: 10.1007/978-3-662-03475-0.

[82] G. Meda, "13.2: Support Design for Reducing the Sag of Horizontally Supported Sheets," *SID Symposium Digest of Technical Papers*, vol. 31, no. 1, pp. 161–163, May 2000, doi: 10.1889/1.1832907.

[83] J. Haq, S. Ageno, G. B. Raupp, B. D. Vogt, and D. Loy, "Temporary bond-debond process for manufacture of flexible electronics: Impact of adhesive and carrier properties on performance," *Journal of Applied Physics*, vol. 108, no. 11, p. 114917, Dec. 2010, doi: 10.1063/1.3517145.

[84] G. P. Crawford, "Flexible Flat Panel Displays," *Flexible Flat Panel Displays*, pp. 1–528, Jun. 2005, doi: 10.1002/0470870508.

[85] J. H. Kim, J. Y. Hwang, B. Y. Kim, J. Y. Kim, D. H. Kang, and D. S. Seo, "Solution for warpage in the liquid crystal display module process," *Japanese Journal of Applied Physics, Part 2: Letters*, vol. 45, no. 46–50, Dec. 2006, doi: 10.1143/JJAP.45.L1277.

[86] Glass manufacturer Wuhu Token Sciences, "Specification of ITO transparent conductive glass for LCD display application." 2013.

[87] C. E. Derrington, P. A. Smith, and H. C. Stauss, "25.1: Invited Paper : High Volume Microdisplay Manufacturing," *Sid Symposium Digest of Technical Papers*, vol. 31, no. 1, p. 371, May 2000, doi: 10.1889/1.1832959.

[88] N. Farid, H. Chan, D. Milne, A. Brunton, and G. M. O'Connor, "Stress assisted selective ablation of ITO thin film by picosecond laser," *Applied Surface Science*, vol. 427, pp. 499–504, Jan. 2018, doi: 10.1016/J.APSUSC.2017.08.232.

[89]   J. Hoogboom, T. Rasing, A. E. Rowan, and R. J. M. Nolte, "LCD alignment layers. Controlling nematic domain properties," *Journal of Materials Chemistry*, vol. 16, no. 14, pp. 1305–1314, Mar. 2006, doi: 10.1039/B510579J.

[90]   "Jetting small of high viscosity fluids for dots packaging applications." https://www.researchgate.net/publication/293714778_Jetting_small_of_high_viscosity_fluids_for_dots_packaging_applications?msclkid=94ead868cee011ec8219806ee6b96263 (accessed May 08, 2022).

[91]   H. Kamiya *et al.*, "56.3: Development of One Drop Fill Technology for AM-LCDs," *SID Symposium Digest of Technical Papers*, vol. 32, no. 1, pp. 1354–1357, Jun. 2001, doi: 10.1889/1.1831814.

[92]   "MDI Advanced Processing GmbH." https://www.mdi-ap.de/en/home/ (accessed May 08, 2022).

[93]   "Ultrasonic Soldering Technology by MBR ELECTRONICS Switzerland." http://www.sonicsolder.com/ (accessed May 08, 2022).

[94]   T. Adachi, "Silica Spherical Microparticles Applied as Spacers," *Handbook of Sol-Gel Science and Technology*, pp. 1–11, 2016, doi: 10.1007/978-3-319-19454-7_59-1.

[95]   F. C. D. Sekisui Shemical Co Ltd, "Micropearl Presentation." 2012.

[96]   H. S. Cho, D. Kwon, M. H. Lee, D. W. Kang, B. C. Kim, and S. J. Yu, "Influence of ball spacer size and density on liquid crystal margin of in-plane switching panel fabricated by the inkjet process," *Japanese Journal of Applied Physics*, vol. 49, no. 5 PART 2, May 2010, doi: 10.1143/JJAP.49.05EC05.

[97]   K. Hemanth Vepakomma, M. Pandey, T. Ishikawa, and R. Koona, "Paper No P41: Predicting Change in Cell Gap in LCD Panels Subjected to Touch Force," *SID Symposium Digest of Technical Papers*, vol. 44, pp. 144–147, 2013, doi: 10.1002/SDTP.23.

[98]   Cuypers Dieter, "Vertically aligned nematic liquid crystal microdisplays for projection applications," Gent University, 2005. Accessed: May 08, 2022. [Online]. Available: https://biblio.ugent.be/publication/470265?msclkid=261ab0f6cee111ecb7a1f51f2fb70ef2

[99]   Y. Zhang *et al.*, "A flexible optically re-writable color liquid crystal display," *Applied Physics Letters*, vol. 112, no. 13, p. 131902, Mar. 2018, doi: 10.1063/1.5021619.

[100]   van de J. Steen, "Design of LCOS microdisplay backplanes for projection applications," Gent University, 2006. Accessed: May 08, 2022. [Online]. Available: https://www.researchgate.net/publication/292348523_Design_of_LCOS_microdisplay_backplanes_for_projection_applications?msclkid=6795e168cee111ecbeaaf5a7d943d1d3

[101]   G. Bodammer, D. W. Calton, and I. Underwood, "26.3: Investigation of the Bow of Silicon Backplanes for Microdisplay Applications," *SID Symposium Digest of Technical Papers*, vol. 32, no. 1, p. 439, 2001, doi: 10.1889/1.1831890.

[102]   K. Kočevar and I. Muševič, "Observation of an electrostatic force between charged surfaces in liquid crystals," *Physical Review E - Statistical Physics, Plasmas, Fluids, and Related Interdisciplinary Topics*, vol. 65, no. 3, 2002, doi: 10.1103/PHYSREVE.65.030703.

[103] J. Klavins, G. Mozolevskis, A. Ozols, E. Nitiss, and M. Rutkis, "Screen Printing of SU-8 Layers for Microstructure Fabrication," *Latvian Journal of Physics and Technical Sciences*, vol. 52, no. 5, pp. 58–67, Oct. 2015, doi: 10.1515/LPTS-2015-0029.

[104] B. Bahadur, J. D. Sampica, J. L. Tchon, and A. Butterfield, "Direct dry film optical bonding - A low-cost, robust, and scalable display lamination technology," *J Soc Inf Disp*, vol. 19, no. 11, pp. 732–740, Nov. 2011, doi: 10.1889/JSID19.11.732.

[105] "NISSHO CORPORATION | LUCIACS® CS9621T/LUCIACS® CS9622T." https://www.nissho-group.com/english/products/luciacs/052/index.html (accessed May 08, 2022).

[106] B. Bahadur, J. D. Sampica, J. L. Tchon, and V. P. Marzen, "Direct-Dry-Film Optical Bonding: Finding New Applications," *Information Display*, vol. 29, no. 4, pp. 34–39, Jul. 2013, doi: 10.1002/J.2637-496X.2013.TB00631.X.

[107] "Materials for Electronic Display Screens | Dow Inc." https://www.dow.com/en-us/market/mkt-electronics/sub-elec-displays.html (accessed May 08, 2022).

[108] K. S. Prabhu, T. L. Schmitz, P. G. Ifju, and J. G. Daly, "A survey of technical literature on adhesive applications for optics," *New Developments in Optomechanics*, vol. 6665, p. 666507, Sep. 2007, doi: 10.1117/12.735948.

[109] D. W. Dahringer, *Adhesives for Micro- and Opto-Electronics Application: Chemistry, Reliability and Mechanics*. Springer, Boston, MA, 2007. doi: 10.1007/0-387-32989-7_35.

[110] B. Pennington *et al.*, "Vacuumless lamination of printable LOCA," *Digest of Technical Papers - SID International Symposium*, vol. 45, no. 1, pp. 28–31, 2014, doi: 10.1002/J.2168-0159.2014.TB00008.X.

[111] G. Yeh, M. L. Rudolph, and J. Y. C. Chen, "68.4: Minimizing the Impact of Bonding Induced LCD Defects," *SID Symposium Digest of Technical Papers*, vol. 44, no. 1, pp. 951–954, Jun. 2013, doi: 10.1002/J.2168-0159.2013.TB06380.X.

[112] "[PDF] Assembly of an XGA 0.9" LCOS display using inorganic alignment layers for VAN LC | Semantic Scholar." https://www.semanticscholar.org/paper/Assembly-of-an-XGA-0.9%22-LCOS-display-using-layers-Cuypers-Doorselaer/d194c87a5b02c433d72314d6bd5108490355a5c7 (accessed May 09, 2022).

Acknowledgements

Appendix A. E-O measurement systems

Definitions

- **Open** – defined as transparency during driving, expressed in relative values (or percent). Analysis reports this number as average from smoothed 250 data points during open state.

- **Closed** – defined as off state transparency, when no voltage is applied (transient scattering mode). Electrically, closed state is defined between time points A and D (Figure 136). Analysis returns this number as lowest transparency value for averaged and smoothed transparency.
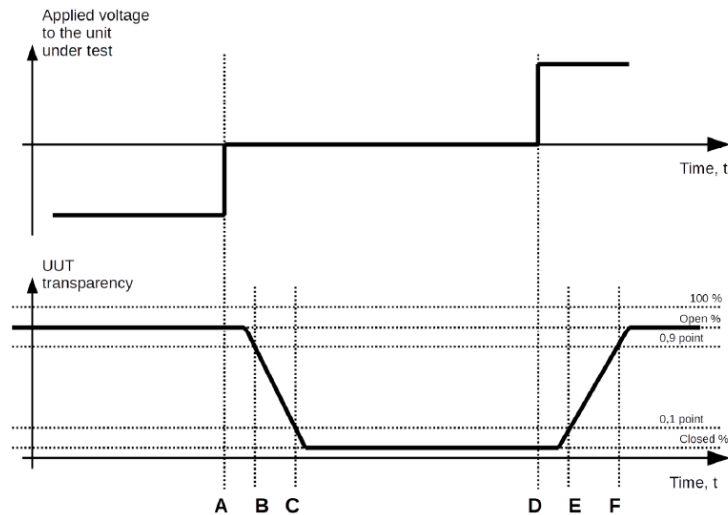

Figure 136.: VST-1 open and close state definitions.

- **Contrast** – Ratio between open state transparency and closed state transparency.

$$C=Open/Closed$$

Note the transparency value calculation:

100 % - open air transparency, measured before putting in unit under test.

0.9 point – calculated by: $\mathbf{0.9\ Open}\ \%\mathbf{=(en-Closed)*0.9+Closed}$

0.1 point – calculated by: $\mathbf{0.1\ Open}\ \%\mathbf{=(en-Closed)*0.1+Closed}$

- **Fall Delay** – time period when voltage is set to zero and transmittance falls below 90% threshold.

- **Fall** – time period between 90% and 10% thresholds (Open → Closed).

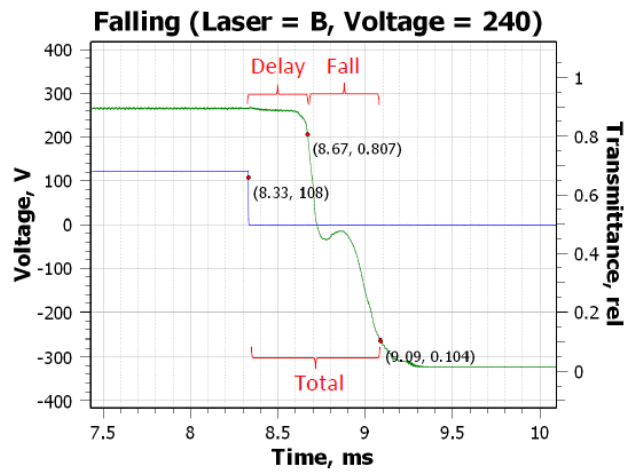- **Fall total** – sum of Fall Delay and Fall, see Figure 137.

Figure 137.: Fall time definition.

- **Rise Delay** – time period when voltage is applied and transmittance exceeds 10% threshold.

- **Rise** – time period between 10% and 90% thresholds (Closed → Open) .

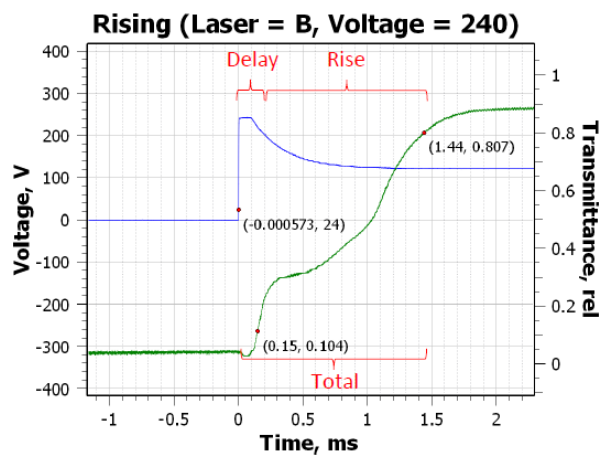- **Rise total** – sum of Rise Delay and Rise, see Figure 138.

Figure 138.: Rise time definition.

VST-1 system

VOL-SHUTTER-TEST-1 is a liquid crystal diffuser test device that measures optical transparency and transient parameters and was historically first to be made and use. Unit is capable of driving liquid crystal diffusers (unit under test – UUT) with bipolar pulse train voltage with variable voltage level (up to 200V) and period. Tester consists of signal generator (controlled via USB), amplifier, measurement circuit with oscilloscope (controlled via USB).

Tester is controlled by software application – it controls the calibration of light sources, waveform generation, measurement of liquid crystal shutters and analysis, as well as result reporting to files and Magic database.

Vol-shutter-test-1 consists of the following devices:

- HVAMP-1 – high voltage amplifier (K=200)

- White LED light source – C535A-WKM-CS0V0151 from CREE, see Figure 139.

- Photodiode-BPW24R from Vishay S.

- PicoScope 3404B – oscilloscope with 4 channels and generator output
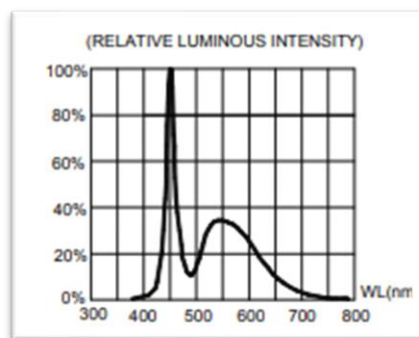
- Laptop PC

Figure 139.: VST-1 LED relative luminous intensity over wavelength.

Vol-shutter-test-1 is accompanied with a software run on the laptop. The software is a Windows .NET 4.0 application, developed to manage the testing of the liquid crystal shutters. The software features include:

- Integration with oscilloscope

- HVAMP-1 control (on/off, temperature measurements)

- Automatic sweep measurement mode – predefined testing method (voltage sweep, …) for different products

- Custom measurement mode – user adjustable measurement setup, waveform setup and rule set for custom testing

- Quick results window for result analysis

- Calibration to ensure precise transparency values

Software has a built-in calibration that maps measured transparency values against precisely known attenuation glass (such as optical dimming glass sheets with precisely known transparency, see Table 42) to ensure linearity of the receiver.

Table 42.: VST-1 calibration shades.

Thorlabs shade	Optical Density	Relative Shade
-	0	1
NE201B	0,1	0,79
NE202B	0,2	0,63
NE203B	0,3	0,5
NE204B	0,4	0,4
NE205B	0,5	0,32
NE206B	0,6	0,25
NE210B	1	0,10
NE210B + NE203B	1 + 0,3	0,05
-	-	0

Analysis algorithm: First all CSV columns from PicoScope 3404B are parsed in software, then histograms are created. Data are smoothed, adjusted by calibration data, calculated open light transmittance and closed light transmittance and timing parameters are calculated.

VST-2 system

The VST-2 developed by LightSpace Technologies is made for measuring various electrical and optical properties of the diffusers resembling closer RGB projection system of AR-HMD. These properties are measured using three lasers (developed by ThorLabs Inc.) with wavelengths:

• 635 nm – CPS635R (PR218013_2005);

• 532 nm – CPS532 (PR218013_2007);

• 450 nm – CPS450 (PR218013_2006);

and the photodiode FDS100 (PR218013_2001; ThorLabs Inc.) as a light sensor, which measures laser radiation which passes through the diffuser while it is being electrically driven.

It is possible to change the driving parameters and also a position of the light sensor relative to the diffuser in the VST-2. In the Figure 140 VST-2 is shown with main components indicated.
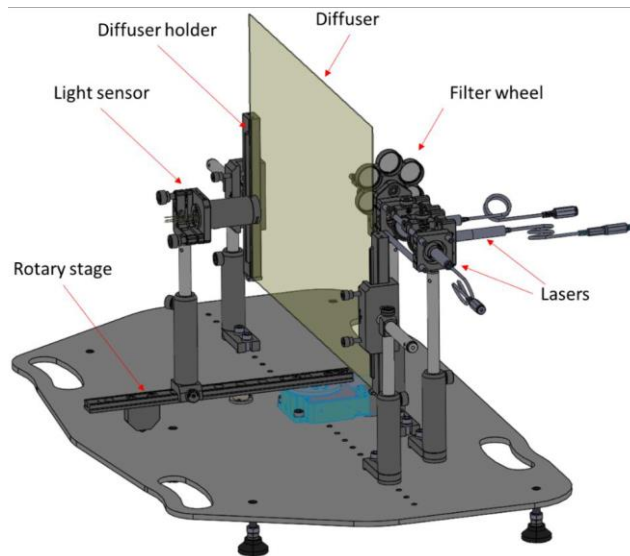
Figure 140.: VST-2 system.

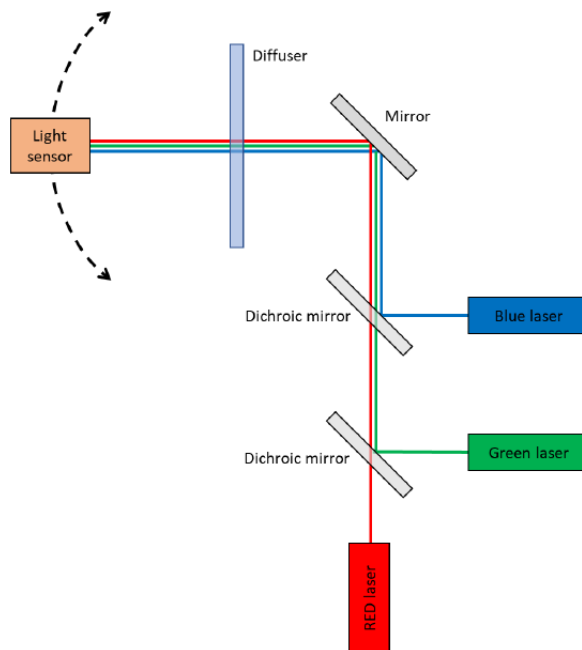The graphic representation of the VST-2 operating principle is shown in Figure 141 (view from the top).

Figure 141.: VST-2 operation principle.

With the help of mirrors, laser beams are positioned so that they travel perpendicularly to the diffuser plane in a straight line (parallel to the base plate's (PR218013_1003) surface) to the center of the light sensor's condenser lens. The diffuser is driven with user defined parameters in the application vst2app (developed by LightSpace Technologies). In this application, user also defines an angle range in which the measurements are performed.

Software has a built-in calibration that maps measured transparency values against precisely known attenuation glass set in filter wheel (such as optical dimming glass sheets with precisely known transparency, see Table 43) to ensure linearity of the receiver.

Table 43.: VST-2 calibration filters.

Number on the wheel	OD of the mounted ND filter	Product number
1	0,1	NE01B; PR218013_2028
2	0,2	NE02B; PR218013_2029
3	0,3	NE03B; PR218013_2030
4	0,4	NE04B; PR218013_2031
5	0,6	NE06B; PR218013_2032
6	no	no

Additional ND filters can be mounted on the light sensor's condenser lens (LE1131-A-ML; PR218013_2013) to obtain other combinations of the optical densities: NE06A (OD: 0,6; ThorLabs Inc.); NE10A (OD: 1,0 ThorLabs Inc.); 46-26 (OD: 2,5; Edmund Optics Inc.), see Table 44.

Table 44.: VST-2 additional filters.

		Mounted on the light sensor's condenser lens				
		none	0,6	1,0	1,0 and 0,6	2,5
On the ND filter wheel	none	none		1,0		2,5
	0,1	0,1	0,7	1,1	1,7	2,6
	0,2	0,2	0,8	1,2	1,8	2,7
	0,3	0,3	0,9	1,3	1,9	2,8
	0,4	0,4		1,4	2,0	2,9
	0,6	0,6		1,6	2,2	3,1

VST-3 system

The latest addition to the testing setup is the integration of spectrometer Ocean Optics Flame T UV-VIS system with driver for studying spectral dispersion, see Figure 142.
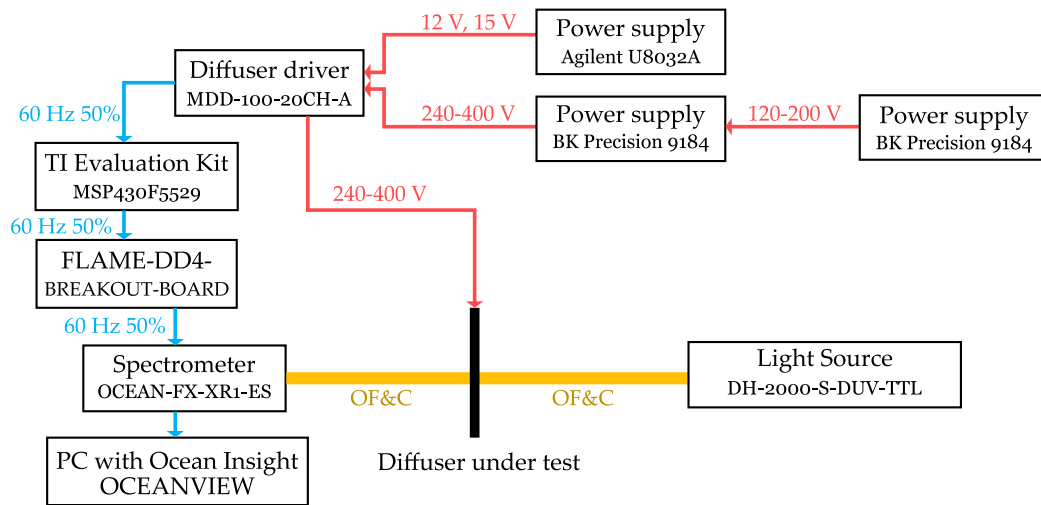

Figure 142.: Setup for spectra dynamics characterization.